SMART OFFSHORE HEAVY LIFT OPERATIONS

SMART OFFSHORE HEAVY LIFT OPERATIONS

Proefschrift

ter verkrijging van de graad van doctor
aan de Technische Universiteit Delft,
op gezag van de Rector Magnificus Prof. dr. ir. T.H.J.J. van den Hagen,
voorzitter van het College voor Promoties,
in het openbaar te verdedigen op dinsdag 27 oktober 2020 om 12:30 uur.

door

Jun YE

Master of Science in Marine Technology,
Technische Universiteit Delft, Delft, Nederland,
geboren te Henan, China.

Dit proefschrift is goedgekeurd door de

promotor: prof. dr. R.R. Negenborn
copromotor: dr. V. Reppa

Samenstelling promotiecommissie:

Rector Magnificus,	voorzitter
Prof. dr. R.R. Negenborn,	Technische Universiteit Delft
Dr. V. Reppa,	Technische Universiteit Delft
Onafhankelijke leden:	
Prof. dr. C. Stoica Maniu	CentraleSupelec, France
Prof. dr. ir. J.W. van Wingerden	Technische Universiteit Delft
Prof. dr. A. Metrikine	Technische Universiteit Delft
Prof. dr. ir. C. van Rhee	Technische Universiteit Delft
Overige leden:	
Prof. dr. ir. S. Baldi	Southeast University, China

The research described in this thesis was supported by the China Scholarship Council under grant 201607720003.

Keywords: Smart Systems, Offshore Constructions, Heavy Lift Vessels, Position Control, Mode Detection.

ISBN 978-94-6384-170-2

So we beat on, boats against the current, borne back ceaselessly into the past.

F. Scott Fitzgerald

CONTENTS

PREFACE

Time flies and before I could even notice, four years' PhD life has already come to an end. As a person seldom has any ambitions in my life, I never thought I would do a PhD until that winter in 2015. Luckily, I accepted this opportunity and succeeded at last, with support from my promotors, my family, my friends, and my colleagues.

First of all, I would like to thank the financial support from China Scholarship Council, and from the Department of MTT for all the research relevance expenses.

I would like to thank my promotor Prof. Rudy Negenborn and co-promotor Dr. Vasso Reppa for providing me a position in TEL when I was in the hardest days during my 3rd year of PhD and for all the supervisions during my last two years' PhD life. Prof. Negenborn is a diligent and encouraging promotor who has been very helpful with his knowledge and vision. I've gained a lot of inspiration and knowledge during our monthly progress meeting. Dr. Reppa is a patient and smart supervisor who has given me so many valuable suggestions in both research and everyday life. I've learned a lot of control knowledge from her, which helped me a lot with my PhD research.

I would also like to express my gratitude towards Prof. Hans Hopman and Dr. Milinko Godjevac for providing me an opportunity to start this PhD, and for all the supervisions during the first two years of my PhD. In addition, I would like to thank Prof. Simone Baldi and Dr. Spandan Roy for their support during my PhD.

Finally and most importantly, I would like to thank my friends, my colleagues, and my family, especially my parents, my parents-in-law, my husband, and my sweet cat Einstein for their emotional and financial support throughout my PhD life. I still remember those depressing days when I was doubtful and lost with all the negative thoughts in my mind. It was Einstein who jumped into my arms in the cold rainy days to cheer me up. It was Zelan, my dear husband, who always stood by my side and encouraged me to continue. It was my parents, who put their jobs aside and flied to the Netherlands to talk with me. It was my parents-in-law, who kindly supported me for all my decisions.

Jun Ye
Delft, September 2020

NOMENCLATURE

$\boldsymbol{\eta}_{\text{v}}(t)$	6 DoFs position (in [m]) and rotation (in [rad]) of the vessel in NED frame
$\mathbf{J}_b^n(\text{t})$	6×6 rotation matrix from BODY frame to NED frame
$\mathbf{J}_n^b(\text{t})$	6×6 rotation matrix from NED frame to BODY frame
$\boldsymbol{\nu}_{\text{v}}(t)$	6 DoFs velocity (in [m/s]) and angular velocity (in [rad/s]) of the vessel
$\mathbf{M}_{\text{RB}}$	6×6 rigid body mass matrix of the vessel (with mass in [kg], and moment of inertia in [kg/m^2])
$\mathbf{M}_{\text{A}}$	6×6 added mass matrix of the vessel (with mass in [kg], and moment of inertia in [kg$\cdot$ m^2])
$\mathbf{D}_{\text{v}}$	6×6 damping matrix of the vessel (in [kg/s] and [kg$\cdot$ m/s])
$\mathbf{C}_{\text{v}}$	6×6 Coriolis matrix of the vessel (in [kg/s] and [kg$\cdot$ m/s])
$\mathbf{G}_{\text{v}}$	6 DoFs hydrostatic force on the vessel (in [N] and [N$\cdot$ m])
$\mathbf{g}_{\text{v}}$	Mass gravity of the vessel (in [N] and [N$\cdot$ m])
$\boldsymbol{\tau}_{\text{thr}}(t)$	Thrust force and moment of the vessel (in [N] and [N$\cdot$ m])
$\boldsymbol{\tau}_e(t)$	Environmental load on the vessel (in [N] and [N$\cdot$ m])
$\boldsymbol{\tau}_{\text{wires}}(t)$	Force and moment from the crane wires caused by the heavy structure (in [N] and [N$\cdot$ m])
$\boldsymbol{\nu}_{\text{current}}(t)$	Current linear velocity and angular velocity in 6 DoFs (in [m/s] and [rad/s])
$\boldsymbol{\nu}_{\text{r}}(t)$	Relative velocity vector of the vessel campared to the current velocity in 6 DoFs (in [m/s] and [rad/s])
$\boldsymbol{\tau}_{\text{wind}}(t)$	Wind induced force and moment in 6 DoFs (in [N] and [N$\cdot$ m])
$\boldsymbol{\tau}_{\text{wave}}(t)$	Wave induced force and moment in 6 DoFs (in [N] and [N$\cdot$ m])
$\mathbf{M}_{\text{l}}$	3×3 mass matrix of the load (in [kg])
$\boldsymbol{\eta}_{\text{l}}(t)$	Position of the load in NED frame in 3 DoFs (in [m])
$\mathbf{D}_{\text{l}}$	3×3 damping matrix of the load (in [kg/s])
$\mathbf{g}_{\text{l}}$	Mass gravity of the load in 3 DoFs (in [N])
$\mathbf{F}_{\text{env}}(t)$	Environmental force on the load in 3 DoFs (in [N])
$\mathbf{R}_3$	3×3 rotation matrix from BODY frame to NED frame
$\mathbf{F}_{\text{l}}(t)$	Load force on the vessel in 3 DoFs (in [N])
$\mathbf{p}_{\text{l}}(t)$	3 DoFs position of the load in BODY frame (in [m])
$\mathbf{p}_{\text{ct}}$	3 DoFs positon of the crane tip in BODY frame (in [m])
$F_{\text{hoist}}(t)$	Scalar represents hoist force (in [N])
$\boldsymbol{\eta}(t)$	Position and yaw angle of the vessel in 3 DoFs (in [m] and [rad])
$\hat{\boldsymbol{\eta}}(t)$	Observation of $\boldsymbol{\eta}$ (in [m] and [rad])
$\tilde{\boldsymbol{\eta}}(t)$	Observation error of $\boldsymbol{\eta}$ (in [m] and [rad])
$\mathbf{R}_3(\psi)(t)$	Rotation matrix from vessel's body fixed coordinate system to NED frame in 3 DoFs (Assuming $\phi = \theta = 0$)

$\boldsymbol{\nu}(t)$	The linear velocity and angular velocity of the vessel in 3 DoFs (in [m/s] and [rad/s])
m	Mass of the load
$\hat{\boldsymbol{\nu}}(t)$	Estimation of $\boldsymbol{\nu}$ in 3 DoFs (in [m/s] and [rad/s])
$\tilde{\boldsymbol{\nu}}(t)$	Estimation error of $\boldsymbol{\nu}$ (in [m/s] and [rad/s])
$\boldsymbol{\tau}_c(t)$	Controlled force from the crane winch during mooring mode in 3 DoFs (in [N])
$\boldsymbol{\tau}_1(t)$	Bounded force from the hanging of the load during free-hanging mode in 3 DoFs (in [N] and [N·m])
$\boldsymbol{\tau}(t)$	Vessel control input in 3 DoFs (in [N] and [N·m])
$\bar{\mathbf{d}}(t)$	Bounded environmental disturbances (in [N] and [N·m])
σ	Construction phase
$\mathbf{F}_\sigma(t)$	Mooring stiffness in mode σ (in [N/m] and [N·m])
$\boldsymbol{\tau}_{1\sigma}(t)$	Force from hanging of the load in mode σ (in [N] and [N·m])
$\mathbf{M}$	Mass matrix of the vessel in 3 DoFs (in [kg] and [kg/m^2])
$\mathbf{D}$	Damping matrix of the vessel in 3 DoFs (in [kg/s] and [kg· m/s])
$\mathbf{M}_\sigma$	Mass matrix of the vessel in mode σ (in [kg] and [kg/m^2])
$\mathbf{I}$	Identity matrix with appropriate dimension
$\mathbf{0}$	Zero matrix with appropriate dimension
$\tilde{\delta}$	The elastic elongation of the crane wires
t_s	Mode switching time
t_D	Detected mode switching time
t	time

Notations

$\lvert\cdot\rvert$	Element-wise absolute value
$\lvert\lvert\cdot\rvert\rvert$	Euclidean norm
$diag\{\cdot,\cdots,\cdot\}$	A diagonal matrix with diagonal elements $\{\cdot,\cdots,\cdot\}$
$c.$, $s.$, and $t.$	The cosine, sine and tangent function of $\cdot$ respectively

1

INTRODUCTION

SMART vessel has been a popular topic in the field of offshore and coastal engineering to increase safety and time efficiency during transportation and offshore constructions. One way to classify how 'smart' a vessel is, is by using levels of autonomy. According to Lloyd's Register, there are six levels of autonomy in vessels [60]:

- *Level 1 (On-board Decision Support): Human operators are responsible for all actions. Digital systems give support to human operators.*
- *Level 2 (On & Off-board Decision Support): Human operators are responsible for all actions. Digital systems can present options for human operators, and can influence the choices of human operators.*
- *Level 3 ('Active' Human in the loop): Digital systems make decisions and actions. Human operators provide supervisions.*
- *Level 4 (Human on the loop, Operator/ Supervisory): Decisions and actions are carried out by digital systems. Human operators have the opportunity to over-ride high impace decisions.*
- *Level 5 (Fully autonomous): Most decisions and actions are carried out by the digital systems, with rare human supervisions.*
- *Level 6 (Fully autonomous): Decisions are made and actions are carried out fully by the system, no human actions are needed.*

Existing studies on smart vessels mainly focus on waterborne transportation with one or more vessels. Projects such as i-CAVE (Integrated Cooperative Automated Vehicles), SCoop (Safe Cooperation of Autonomous Vehicles in Mixed Traffic), AVATAR (Sustainable urban freight transport with autonomous zero-emission vessels), and many more, have been carried out since 2016. For construction vessels, however, the research on autonomy is limited. In this chapter, we will introduce the research background of offshore heavy lift operations and propose research questions. The outline of the thesis is provided in the end of this chapter.

1

1.1. HEAVY LIFT VESSELS AND OFFSHORE HEAVY LIFT CONSTRUCTION

The economic growth worldwide has witnessed significant increase in the demand for energy to fulfill the needs of every life and to assist the growing of industries. During the last decades, the exploration and exploitation of energy resources, such as wind energy, oil and gas, has been extended from onshore to offshore, where huge platforms have been installed to extract, store, and process crude oil and natural gas, and windmills to produce electricity [89]. After several years of service, these platforms reach the end of their lifetime and should be removed.

Offshore structures (e.g., oil platforms, offshore windmills) are mostly installed and removed by vessels offshore [56]. There are mainly two methods to install and remove such facilities using a vessel. The traditional way is to use offshore cranes to lift these facilities, while a more recent innovative way is to do a so-called 'float over' installation [75, 92], using float over vessels to transport and to install the facilities in one piece. However, such installation method needs specially designed float over vessels that can fit over the substructure, and can sail out after construction work. In the second case, there is a limitation on the size of the facility to be installed or removed, and the motion of the vessel has to be carefully taken care of during the construction. Furthermore, float over installation is hardly used in the removal of offshore facilities due to its high request for the topside size. Due to such limitations, most offshore operations are currently done by crane vessels and this research will focus on offshore operations by crane vessels.

In the case of crane vessels, in order to perform the lifting of very heavy loads, huge cranes are placed on the vessel. The installations of offshore structures by crane vessels can be divided into two types. One is to install by parts and integrate the parts offshore, the other is to integrate different parts onshore and install the structure as a whole [101]. For the first way of installation, the requirement of a vessel's crane capacity is relatively smaller. However, it takes more time for offshore operation to be done. For the latter method, the construction time is improved but the crane capacity must be high enough for the integrated offshore structures.

In addition to the installation of offshore structures, the removal of such facility is also done by heavy lift vessels. According to the regulations set by International Maritime Organization (IMO), companies should remove offshore installations when such facilities are abandoned or no longer used in order to protect the environment [44]. For the stakeholders of such facilities, it is also preferable to remove such offshore structures when the production ends to save the maintenance costs. With the increasing maintenance fees due to the aging of the platforms and the low oil price, removal of such structures is becoming even more common than installation. An estimation of over 7500 offshore oil and gas platforms in over 53 countries will become obsolete in the next few decade [96]. These platforms should eventually be removed. Such removal assignments can also be done once, or in multiple times by smaller sections [83].

As the offshore environment can change quickly and can be harsh [7, 93], there are IMO rules that describe what kinds of environment heavy lift operations can take place [6]. If a platform is constructed or removed in several pieces, normally the work needs to be carried out with one or more crane vessels and with multiple removal assignments.

This sometimes means more waiting time for the proper weather conditions, and more construction time which increases the period that the operators stay in a hazardous environment. Thus most offshore contractors nowadays prefer to use high capacity offshore cranes to install or remove integrated structures to save their budget, and to ensure safety.

Crane vessels are widely used for transporting and construction of offshore or onshore facilities and cargoes in coastal regions and in deep/ shallow sea [98]. These crane vessels may be of two types: vessels with a relatively small crane capacity for coastal areas [48,49]; and vessels with a large capacity for offshore constructions [24,27]. The first type of crane vessels are normally designed with mobile cranes which can move in three dimensions to transfer the containers or other small scale objects in a flexible and quick way, which normally have a capacity of up to 120 tonnes. The latter type of crane vessels, which are known as heavy lift vessels, are designed for heavier structures. Figure 1.1 shows an example of a vessel with a crane installed at the aft. For such vessels, the cranes installed on board are less flexible and operable due to the size and large capacity. The lifting capacity of such vessels can be much higher than coastal crane vessels reaching 14,000 tonnes. It is worth to note that this type of vessels can be built on top of existing vessels. An example of heavy lift vessels with load is shown in Figure 1.2.

Figure 1.1: Crane Vessel Wei Li in Rotterdam Port [8]

Both installation and removal assignments require the vessel to stay in position during the lifting/offloading period. Earlier position keeping methods before adapting dynamic positioning systems include mooring and jacket [101]. For the mooring method, the vessel first sails to the desired position and moors to the seabed. This method can provide relatively stable position keeping for the vessel. However, the result can be worse during bad weather, and the mooring procedure takes time as the bunch needs to be released slowly. When a jacket is used, the vessel is fixed on a platform next to the construction point thus the heavy lift work can be performed with no wave or current impact on the heavy lift vessel. Both methods are time consuming as several more construction

Figure 1.2: Heavy Lift Vessel with a Trial Lifting [20]

works have to be done before doing offshore removal or installation. To save time, dynamic positioning (DP) systems are designed, which are digital control systems developed to maintain the position of the vessel using its propulsion systems [31, 85–87].

Nowadays, most heavy lift vessels are assisted by DP control methods, with human operators on board to adjust control gains and to control the crane manually. The state of the art of systems and operations involved in heavy lift construction work in a most general case is illustrated as in Figure 1.3. Currently, both the load controller and the vessel's position controller are operated by humans during the offshore construction work. Human operation and observation play an important role in such construction assignments. Although the vessel is partly automatic (i.e., with DP system and low-level load controller), most high-level control jobs are carried out by humans (i.e., adaptive tuning of the DP controller, load control, etc.). The harsh working environment and the very low frequency movement of the vessel under DP make it challenging for operators to observe changes in the system and to make correct decisions in time. Previous reports have also shown that during offshore heavy lift operations, the position of the vessel can become instable due to the large hoist force in the crane wires [42]. The instable behavior of the vessel position is difficult to observe by operators and incident might happen due to both current DP system and human error [29]. Thus smart systems are needed to assist or replace operators during offshore constructions.

1.2. CONTROL OF OFFSHORE HEAVY LIFT CONSTRUCTIONS

With the development of information and communication technologies (ICT), control systems are becoming popular in our everyday lives and in industries production to reduce cost and provide efficiency. Applications of control systems in heavy lift constructions mainly focus on three aspects:

- **Position control and motion control of vessels** [4, 15, 29, 50, 87, 100, 104]. Control

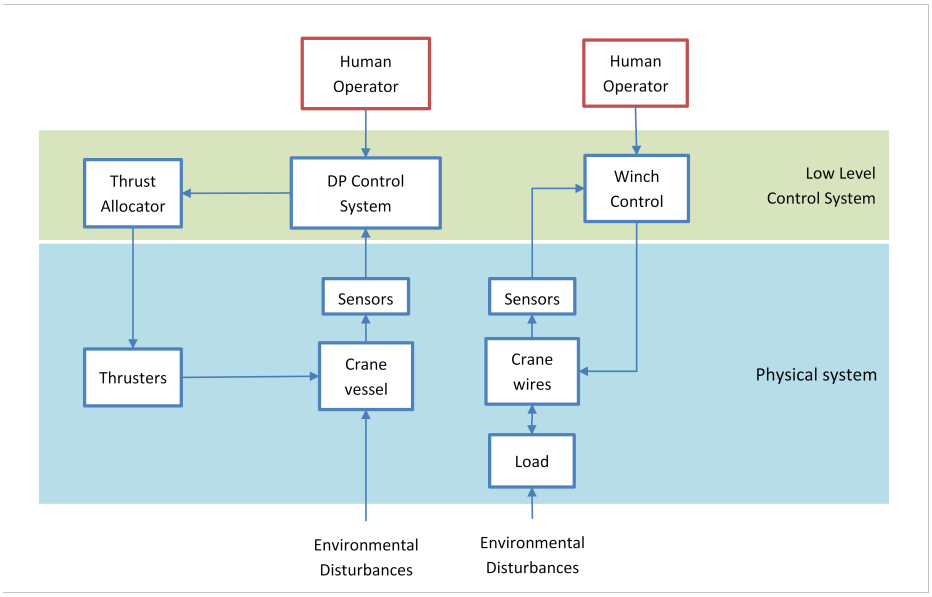

Figure 1.3: State of the Art of Offshore Heavy Lift Construction

of low frequency movement caused by slowly-varying environmental load is usually the main priority for the position control [31]. While active or passive heave, roll and pitch compensations are widely used for high frequency motion control caused by high frequency environmental disturbances [15]. Position control can be achieved by digital control systems with operator interfaces. Such a control system for offshore vessels includes three aspects: position keeping (i.e., dynamic positioning), trajectory tracking, and path following. Position keeping is used to keep the desired position of a vessel's Center of Gravity (CoG) and the yaw angle of the vessel using the propellers and thrusters on board. Trajectory tracking and path following both control the track of the vessel. Trajectory tracking systems take time into consideration, while path following controllers only control the position of the vessel regardless of time.

- **Control in crane operations** [26,66,88]. Control in crane operations includes load control and interaction systems for crane operators. The tasks of such control systems are to stabilize the load, or to unload/load the heavy structures to/from the desired position.

In this work, we will focus on both position control of the vessel and control of crane operations that can be utilized to reduce human error during offshore heavy lift operations. By designing and integrating these control systems, we achieve a high level of autonomy of the offshore heavy lift operations, which can assist or replace operators on board when needed (e.g., in bad weather conditions). To do so, we hereby in particular focus on heavy lift offshore removal work, and explore the increasing autonomy of

offshore heavy lift operations under DP control.

In general, a complete offshore removal work consists of two modes, as illustrated in Figure 1.4:

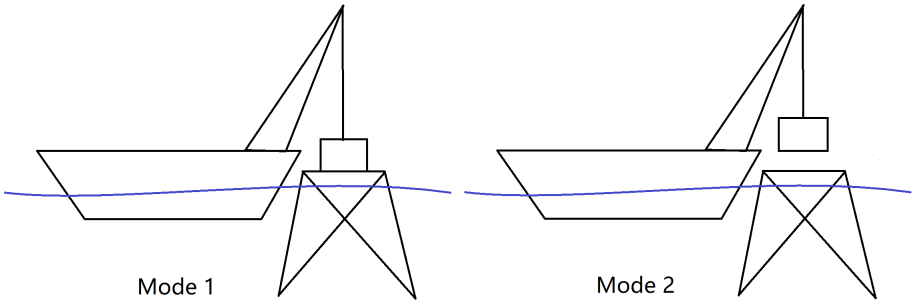

Figure 1.4: Heavy Lift Procedure under Dynamic Positioning

- Mode 1: The heavy lift vessel at the desired position with no load or with fixed load, where the load refers to the topside of the platform in the case of removal assignment, is connected to the heavy lift vessel via hooks attached to the crane wires. The load is gradually lifted up from the platform to the crane by the heavy lift vessel. This lifting process takes approximately 30 minutes, depending on the weight of the load [104].
- Mode 2: With free-hanging load. This step starts when the load is free-hanging above the platform. The heavy lift vessel needs to stay in position via DP control system for further examination.

For construction Mode 1, the dynamics of the vessel is different than the one for construction Mode 2. During the complete construction procedure, the modes are observed by human operators, and the DP systems are manually switched to adapt to the construction modes. This study will be based on the smart operation during the above mentioned modes.

1.3. RESEARCH QUESTIONS

Researches and observations from the industry show that Mode 1 and Mode 2 of heavy lift operation can be hazardous due to the limited clearance between the platform and the vessel, and due to the variety of vessel-load system with respect to the different modes [4, 29, 104]. This thesis focuses on proposing a novel ICT framework that can handle both the position control of the vessel and the stabilization of the crane load during offshore heavy lift removal assignments. This thesis aims at increasing the level of autonomy of offshore heavy lift operations, and at improving safety and reducing cost. The main research question of this research is:

How can we design smart control systems to improve the safety and reliability of offshore heavy lift operations under dynamic positioning?

Currently, the detection of the mode change and the switching of the DP controller are done manually by operators on board, which leads to high hazard of human error and high labor cost. The research objective in this thesis is to design a smart vessel and load position control system that can detect and react to the mode change during offshore heavy lift operations without human input. Such a system can assist or replace operators on board when needed (e.g., in case of bad weather conditions).

To achieve smart offshore heavy lift operation, we need collaboration of position control, load control, and the detection of mode change. Thus the following specific research questions are defined to address the main research question:

Subquestion 1: What is the state of the art in smart offshore heavy lift operations?

Researches have been done on the subject of smart control for offshore operations. Although not much work is directly related to offshore heavy lift operations, there are multiple studies on digital control systems in other offshore operations such as dredging and pipelaying. However, the gap between practical need and previous research still exist. We need to find out why we would like to study on this certain topic.

Subquestion 2: How to model dynamic positioned offshore heavy lift operations?

Offshore heavy lift vessel-load systems are time-dependent during the complete offshore operation. The model of such operations should also be a time-dependent model which can switch its operation mode.

Subquestion 3: How to solve the DP stability and robustness problem for heavy lift operations during Mode 1? and Subquestion 4: How to design a DP controller for heavy lift operations considering the mode switching during the operation?

Previous studies show that the DP controller for offshore heavy lift vessels can become unstable due to the large unknown crane force, and the changing model of the vessel due to the time-dependent crane force. In this thesis, we design an adaptive switching controller for DP during offshore heavy lift operation.

Subquestion 5: How to design a software-based system to detect the switching of the construction mode during offshore heavy lift operations?

For adaptive switching control, it is important to get to know the time for switching. A detection system should be designed to detect the switching time.

Subquestion 6: How to design a nonlinear control system for the under-actuated heavy load?

The crane load connected to the heavy lift vessel is an under-actuated system with only hoist force in the crane wires under control. A lot of previous studies have focused on the control system of a crane which can adjust its boom angle and rotate in the hori-

zontal plane. However, for heavy lift vessels, some cranes are fixed for being able of lifting heavy loads, and not able to rotate fast enough for control purposes. Thus a nonlinear control system is made for offshore heavy lift vessels with free-hanging load, in order to stabilize the load by adjusting the crane force.

Subquestion 7: How to integrate the designed systems into a smart offshore operation system?

The control systems and the detection system are separate systems, each of which can improve part of the offshore heavy lift operation. To achieve smart offshore heavy lift operation, an integration of the separate systems should be made.

1.4. RESEARCH METHODS

To tackle the main research question and subquestions, the following methods are developed: Before addressing the research question, a *literature review* is carried out. A *first-principle physical model* is designed for the time-dependent offshore operation assignment. For the design of smart control systems, three main methods are used in this thesis: *model-based detection system*, *adaptive switching control*, and *backstepping control*. The subsystems are then *integrated* into a smart system.

To answer *Subquestion 1*, we first provide a *Literature review* on smart systems for offshore heavy lift operation and related subjects, such as smart control of other offshore operation work. Based on the literature review, the research gap is proposed.

To answer *Subquestion 2*, we make *a first-principle model* based on the physical properties of the vessel-load system during heavy lift operations. The model is tested under various environmental load.

Adaptive switching control is proposed for DP control systems on board of the heavy lift vessel to answer *Question 3* and *Subquestion 3*. In this work, an adaptive switching controller [59] is made for heavy lift vessels with bounded uncertainties.

To answer *Subquestion 4*, we propose a *model-based detection system* to detect the mode change during the operation assignment. There are a few different methods to detect the system modes. The methods can be classified into two categories: signal-based and model-based [37]. For the heavy lift application, the system model is known with some uncertainties, thus a model-based detect system is used for the design of the detection of the mode switch.

A backstepping controller is designed to control the load motion by defining the desired hoist force in the crane wires and thus answers *Subquestion 5*. For nonlinear under-actuated systems that are difficult to use input output linearization methods, backstepping control can cancel the nonlinearity and find a control signal that can handle the under-actuated systems [28]. Thus in this work, a backstepping control method is used to obtain the desired crane force for the stabilization of the free-hanging crane load.

Integration of subsystems is done to combine all the described controller and detection system into one smart control system and thus answers *Subquestion 6*. The system is tested under different environmental loads with different construction scenarios. An illustration of the integration of the physical and digital systems included in this thesis is shown in Figure 1.5, where the red blocks represent the newly designed digital system

to assist or replace human operators.

In order to answer *Subquestion 7*, we will integrate the proposed control systems and the detection system into one smart system as shown in Figure 1.5. In figure 1.5, the inputs from human operators in Figure 1.3 are replaced with a high level smart system.

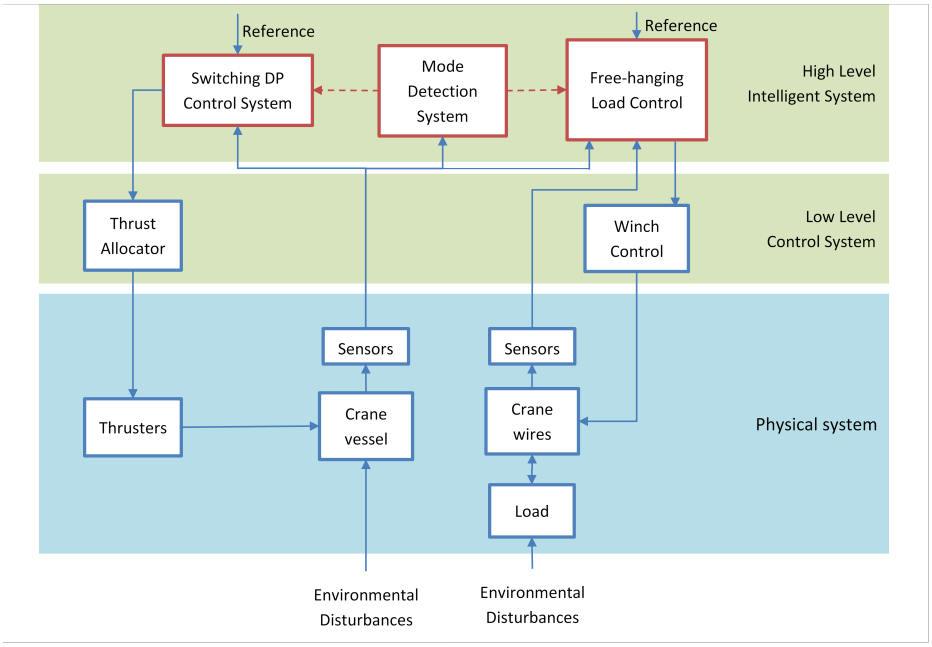

Figure 1.5: Proposed Offshore Heavy Lift Construction

1.5. CONTRIBUTION

This thesis proposes a complete smart detection and control scheme that can be adapted to the offshore heavy lift operation. The designed smart detection and control scheme is assessed using a first-principle physical model. The contributions of this thesis include:

- A detailed first-principle physical model which is designed for offshore heavy lift operations of offshore structures with different weights under various environmental disturbances. The model consists of vessel dynamics, load dynamics, a hydraulic crane winch, sensors for vessel position and velocity, and propulsion systems. This model is used for simulations and the control schemes are based on this model.
- A DP control system is designed based on adaptive switching control methods.
- A monitoring system is designed to detect the switch of the operation modes fast and secure. The model-based detection system uses input/ output data and assumes unmodeled bounded disturbances.

- A nonlinear under-actuated load controller based on backstepping control to stablize the hanging heavy load. The controller is based on an under-actuated crane load model which can only be controlled via the hoist force.

The DP controller, digital detection system, and load controller are then integrated as a complete smart heavy lift operation system, which is simulated under various environment.

1.6. THESIS OUTLINE

This thesis consists of eight chapters. The outline of the thesis is shown in Figure 1.6.

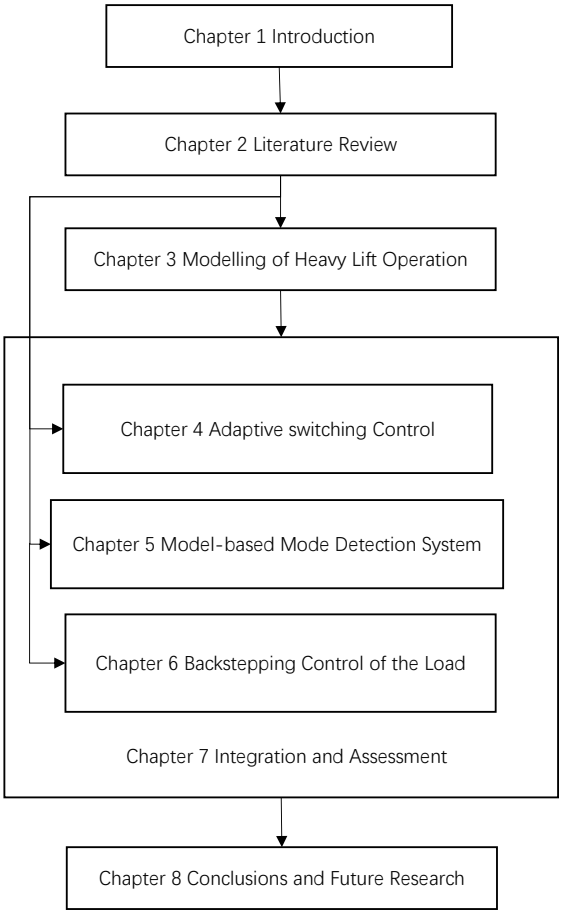

Figure 1.6: Dissertation Outline

Chapter 2 answers *Subquestion 1.* It provides a literature review of the state-of-the-

art methods for DP systems, detection systems, and control of offshore cranes. In the end of Chapter 2, the research gap is given and conclusions are drawn.

Chapter 3 answers *Subquestion 2*. It shows how the first-principle physical model of the offshore heavy lift operations, which includes the time-dependent subsystems on board of heavy lift vessel and the vessel dynamics under the influence of the environmental disturbances. The crane is modeled as a rigid body with a hydraulic winch. The heavy load is modeled as a mass block under hoist force and environmental disturbances.

Chapter 4 answers *Subquestion 3* and *Subquestion 4*. It provides a robust controller for offshore heavy lift in Mode 1. Based on the robust controller, an adaptive switching DP control scheme is proposed for the complete offshore operation procedure. The time-dependent nonlinear dynamics of the vessel is assumed to be known with parametric uncertainties, and the heavy load is assumed to be within a user-defined range. Simulations are performed with the physical model designed in Chapter 3 to test the proposed DP controller. The simulation results are given with different uncertainty settings and under different operation scenarios.

Chapter 5 answers *Subquestion 5*. It gives the details of the model-based mode detection system, which is designed to detect the mode change during offshore operation to assist the switching of the adaptive switching controller proposed in Chapter 4. The proposed detection system considers bounded measurement noise and environmental disturbance effects. The detection system is simulated and validated with the physical model. Results are given and analysed using different settings of noise bound.

Chapter 6 answers *Subquestion 6*. In this chapter, a backstepping controller is designed to obtain the desired crane force to ensure stable load position in the mode where the heavy load is disconnected to the platform, and is free-hanging by the crane wires. The control scheme is simulated and the results are analysed.

Chapter 7 answers *Subquestion 7*. This chapter provides an integrated system of mode detection system, adaptive switching DP controller, and backstepping load controller. The integrated system is described in detail and simulated with different loads and various environmental disturbances.

Conclusions and recommendations for future research are given in Chapter 8.

2

LITERATURE REVIEW

PREVIOUS endeavors to improve intelligence of heavy lift operations mainly focus on two aspects: DP control of the vessel and nonlinear control of the load during different construction modes, while the detection of the switch between different construction modes is done by human operators. In this section, we will discuss *Subquestion 1: What is the state of the art in smart offshore heavy lift operations?* To answer this research question, previous studies on both aspects and existing studies and applications on detection system are discussed. In Section 2.1, the current state of art regarding position control of offshore vehicles are discussed. In Section 2.2, the state of the art is given on digital systems that can detect model change and applications of such systems on offshore constructions. Then in Section 2.3, control methods with respect to offshore cranes are discussed. In Section 2.4, conclusions of the literature review are given.

2.1. DYNAMIC POSITIONING

Control of ship position and motion can be divided into two types, low frequency position control and high frequency motion control (Figure 2.1). For vessel's heave, roll and pitch motion, compensations are widely used for high frequency motion control, which can be achieved by either adding additional passive damper while designing the structure of the vessel [108], or using active compensation control system [18]. In this section, we will focus on stabilizing the low frequency vessel position, which is crucial in heavy lift operations to avoid collisions. The position of the vessel can be controlled either by external systems such as mooring system and jacket, or by a digital position control system. Digital position control systems for offshore vessels include three different aspects: position keeping, path following, and trajectory tracking. Position keeping, also known as dynamic positioning (DP), is widely used to keep the position of vessel's Center of Gravity (CoG) and the yaw angle (i.e., the heading angle) of the vessel at the desired position using the propellers and thrusters on board. Trajectory tracking and path following both control the track of the vessel. Trajectory tracking systems take time into consideration, while path following controller only controls the path of the vessel regardless of time [31].

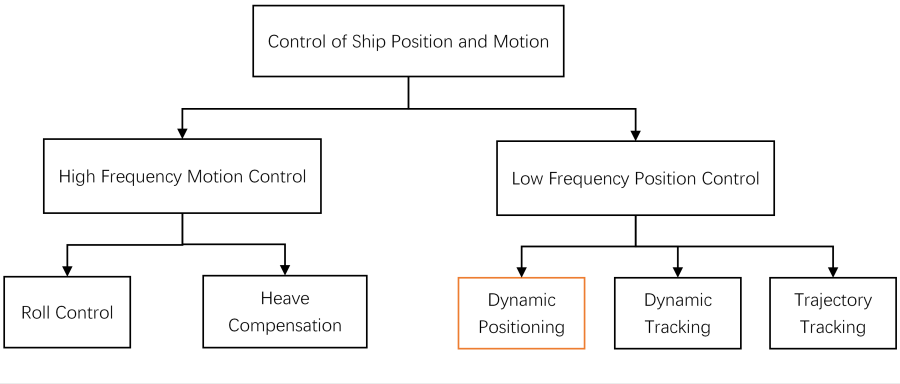

Figure 2.1: Classification of motion and position control of vessels

For offshore heavy lift construction, the vessel should stay in position during the assignments. Thus DP systems are used in such operations to keep the heavy lift vessels in position. An illustration of a DP system is shown in Figure 2.2. The digital DP control system consists of three components: observer, controller and thrust allocator. The observer is used to estimate the position and velocity of the vessel from the measurements of different sensors. The controller calculates the desired force that is needed for the vessel to stay in the desired position. The thrust allocator considers the number and the type of thrusters on board in order to distribute the desired force to each thruster [31]. These three components, especially the controller and the observer, have been the most widely studied parts in DP system as discussed next.

2.1.1. DYNAMIC POSITIONING SYSTEMS

The first DP systems were model-free systems based on lowpass filters and PID controllers. In order to reduce the time delay caused by the lowpass filter while filtering out the measurement noise and high frequency vessel motion, a new DP system was introduced using a Kalman filter as an observer [5]. However, the controller within the DP control system is still a PID controller which is not model based and the performance of the controller relied on the tuning of the parameters. The tuning of such model-free controller is not theoretically based which requires much efforts and can be time-consuming. However, though the stability of DP system with PID controllers is proven during practical use, the theoretical stability is never assessed. In order to build theoretical stable control systems, in 1995, a new DP system was proposed using model based control algorithm where an LQG feedback controller and a model reference feed forward controller are applied [87]. This was the first time that the design of DP system was based on vessel models. Vessel models were simplified and linearized to get access to linear control. As the vessel model with the environmental loads is nonlinear due to the rotation matrix between body frame and earth-fixed coordinate system, one had to linearize the vessel model with different heading angle before designing a

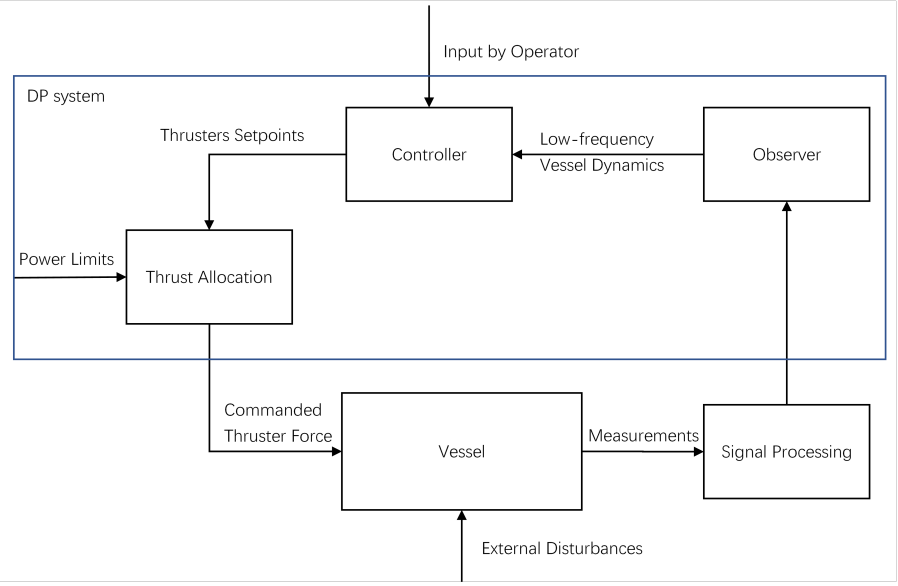

Figure 2.2: Overview of a DP control system

linear controller. Then from 1993 to 2000, passivity of ship position control is studied thoroughly [30, 32, 33, 50, 76, 85, 86]. Passivity is a physical term which refers to the energy inside a system, and a passivity control system is stable with bounded input [62]. In 2000, nonlinear controller and nonlinear observer are designed for DP vessels to reduce the design work for DP systems and for better performance during work under DP system [30]. Robustness of DP systems come into the sight of marine engineers after the stability was solved to handle model perturbation [50]. More recent research on DP systems are limited in the last decade, with most of the literature focus on uncertainties caused by external environmental disturbances and parametric uncertainties of vessel dynamics [21, 46, 91, 102, 110].

2.1.2. DYNAMIC POSITIONING FOR HEAVY LIFT VESSELS

Nowadays, DP systems are studied and designed for heavy lift vessels to avoid oscillation during the operations and to be reduce the required time for such operations. During offshore heavy lift operations, the heavy lift vessels have large external force generated by the crane wires from the load. The direction and value of the crane force are both not fixed. Thus they can change with the changing of the vessel and load movements.

Studies from the last decade on the DP systems of heavy lift vessels focused on the construction period during its mooring stage. In 2008, the stability problem of position control systems on board of heavy lift vessels during loading and offloading of the construction procedure has been observed by the industry [29]. A preliminary solution based on feedforward control was the first solution proposed to moored DP which did not consider thruster dynamics [100].

Recent studies on DP for crane vessels focused on:

- Attempting to reduce the overall stiffness within the system by tuning the PID controller or by applying feedforward force [4, 100, 104]
- Handling crane force as parametric uncertainty and external disturbances in the control design [21].

For the first category, the tuning of the controller is based directly on the measurement of the crane force [100], and is only valid for the construction mode when the load is still on the platform [4, 104]. For the second category, the controllers are designed for vessels with unknown environmental disturbances and unknown parameters [21, 22] that can be applied to offshore construction scenarios, but the proposed control schemes are not precisely designed for offshore heavy lift construction procedure. The designed controllers therefore neglected the dynamics differences of crane vessels with construction vessels, as well as neglecting the special hazardous working environment of offshore heavy lift vessels. From the literature review, we can tell that an observer-based DP controller for the complete procedure of offshore heavy lift constructions is still missing.

2.1.3. RESEARCH GAP

Literature	DP	Model-based	Consider Uncertainty	For heavy lift
[5]	∘	-	-	-
[32, 50, 85–87]	∘	∘	-	-
[29, 100]	∘	-	-	∘
[21, 46, 91, 102, 110]	∘	∘	∘	-
[4, 104]	∘	-	∘	∘

Table 2.1: Literature review in DP: ∘ represents that the relative category is considered in the literature, and - denotes that the relative category is missing in the literature

Table 2.1 shows the state of the art of the literature on DP systems. In general, the DP systems have been well-studied with vessels that are not affected by large external disturbances in offshore constructions. However, the overall stability of DP observer and DP controller, DP system for vessels with large construction force, and DP system with uncertainties caused by such construction force are still missing in the literature. Although some research has been done on controlling of offshore lifting vessels, this research either focuses on cranes with small load capacity, or only consider limited degrees of freedom.

Furthermore, solutions that have been proposed to improve DP systems on board of heavy lift vessels are only for certain stages of the construction work, which are either the loading and offloading modes when the vessel is connected to the platform via crane wires while the load is transferring from the platform to the vessel, or the mode when the load is free-hanging.

Thus, further research is in need in the field of observer-based DP controller, which can deal with both load uncertainty and dynamics uncertainty, and can work under dif-

ferent construction stages. Such research should also take into consideration all dimensions that are involved in offshore heavy lift constructions.

2.2. MONITORING SYSTEMS

Digital detection systems are monitoring systems that can detect the change in a model or a system. These systems are designed for fault and failure analysis, mode changing, and structural damage analysis. Such model-based detection systems are widely used in transportation to detect driving modes and to improve safety for automobiles and trucks. In 2002, drowsy driver detection systems based on videos and models was designed to assist long-time truck driving [40]. Similar applications include distraction detection of drivers' driving patterns [10, 16, 58, 95, 99], and collision detection systems [1, 74]. Other applications of model-based detection systems include failure mode detection [9, 13, 17, 38, 65], sensor fault detection [61, 78, 79, 109], and detection of structural damage [2, 52, 57, 103].

There are various methods to detect the system dynamics. The methods can be classified into two categories: signal-based and model-based [35]. For signal-based detection system, the models of the industrial process or the practical system are not required. The decisions of the change of system dynamics are made based upon prior knowledge on the behaviors of the normal systems. A model-based detection system, however, takes the model into consideration and builds a detection system based on the model. In this section, we will discuss existing studies on detection systems, especially model-based detection systems, and the application of such systems in the field of offshore constructions.

2.2.1. MODEL-BASED DETECTION SYSTEM

Model-based detection systems are widely used in transport and manufacturing industries. An illustration of model-based detection system is shown in Figure 2.3. The system is designed based on the physical model of the target system, and the input and output measurements of the system. The system model collects input and output data from the real system to derive an estimated output of the target system. The estimated output then is compared to the output of the real system to obtain the residual. The residual is further analyzed for different detection purposes.

2.2.2. DETECTION SYSTEM FOR OFFSHORE STRUCTURES

Detection systems and fault-tolerant controllers based on detection systems are developed and applied in offshore constructions extensively to increase safety during offshore constructions and offshore energy productions. Applications of detection systems for offshore structures includes applications on offshore wind farms [3, 14, 23], applications in oil and gas production [67, 69], and application during offshore construction [34, 84, 94].

In the field of offshore wind farms, such applications include fault diagnosis of offshore wind farms with multiple wind turbines in a cooperative framework for fault tolerant control [3], and fault diagnosis of offshore wind turbines to guarantee self diagnosis during offshore energy production [23] and fault diagnosis system based on a Kalman

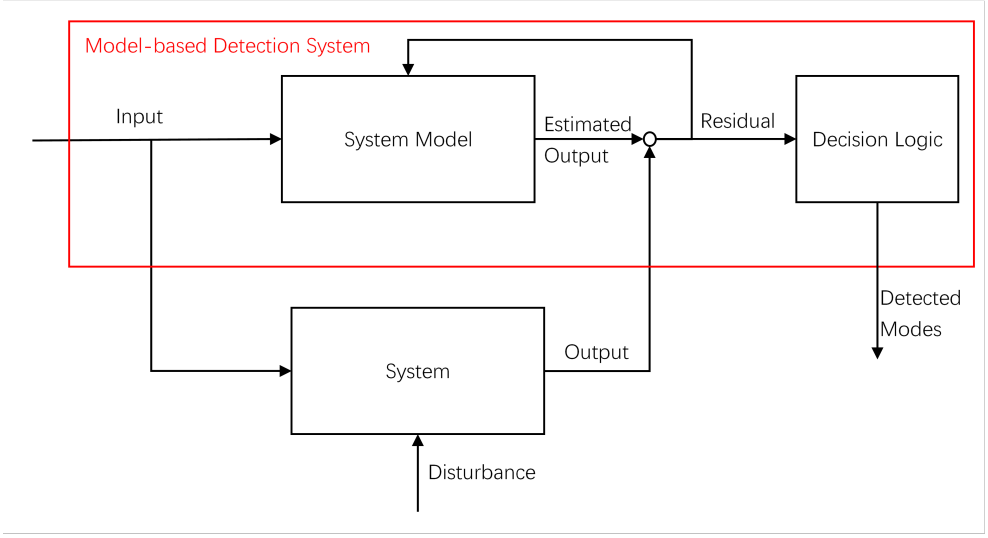

Figure 2.3: Model-based detection system

filter for blade pitch systems in floating wind turbines [14].

Similar to offshore wind energy production, offshore oil and gas production procedure is also hazardous due to the changing weather and the harsh working environment. The large and complex offshore oil platforms face the probability of failure in valves, pipelines, leakage from other parts, etc. Thus fault diagnosis systems are designed for fault detection (e.g. leakage detection [67]) and condition monitoring [69].

Apart from the above mentioned applications, detection systems are applied and integrated in the control systems for offshore construction vessels during offshore assignments. Such applications include fault and leakage detection systems in dredging [94], pipe laying [34], and crane operations [84].

2.2.3. RESEARCH GAP

Literature	Model-based	Offshore constructions	Heavy lift operations
[1, 2, 9, 10] [13, 16, 17, 38] [40, 52, 57, 58] [61, 65, 74, 78, 79] [95, 99, 103, 109]	∘	-	-
[3, 14, 23, 34] [67, 69, 84, 94]	∘	∘	-

Table 2.2: Literature review in detection systems: ∘ represents that the relative category is considered in the literature, and - denotes that the relative category is missing in the literature

According to Table 2.2, research on detection system for offshore heavy lift modes is still missing. Currently, the detection of different construction mode during offshore heavy lift operations is observed by operators on board, then the decision is made and transferred to DP operators by oral communication for further action. This detection method rely completely on the human observation and human decision, which can be subjective and can involve human errors. Such operations also provide a hazardous working environment for the operators. For underwater constructions, additional unmanned underwater vehicles are used for observation of the construction mode. In order to lower construction cost, reduce human errors on board and to improve the working environment for the crew, a detection system for construction modes should be investigated to replace or assist human decision.

2.3. CONTROL OF HEAVY LOAD

The control of the load position during offshore construction work is normally achieved via control of torque in the crane wires and control of angles and local position of the crane [25]. With the increasing number of offshore heavy lift constructions, the stability of offshore heavy loads has become an important research topic since the beginning of this century. Recent studies on the control of crane load can be classified into three categories:

- Studies on active heave compensation of load by controlling the crane winch to avoid oscillating in the vertical direction of the load [15, 53, 66].
- Studies on adaptive control for fully actuated mobile cranes with low load. These studies focus on the mobile cranes on board, which are mostly used for transporting containers in a port [48, 49, 70–72].
- Studies on nonlinear control systems for offshore boom cranes for load position stabilization and trajectory tracking [25, 26, 43, 63, 64, 77, 90].

Below, the literature on offshore load control within each category will be discussed.

2.3.1. HEAVE COMPENSATION

Offshore cranes are located on vessels, whose motions are influenced by the external disturbances such as wind force, wave force, and current force. The roll, pitch, and heave motions of the vessels make it difficult to stabilize the load in the heave direction. Thus heave compensation techniques are commonly used on crane vessels to stabilize the heave position of the lifted load. There are typically two types of heavy compensation techniques: passive heave compensation and active heave compensation [68].

A passive heave compensation system is a combination of spring and damper normally achieved using physical systems such as hydraulic systems, and acting on the external disturbances passively [73]. Active heave compensation systems usually consist of a disturbance observer to estimate the external disturbances, and the compensation systems that act on the vessel according to the estimated disturbances actively [19].

2.3.2. CONTROL OF LIGHT LOAD

Many research works have been carried out to control precisely the position of the load by controlling the movement of the crane and the hoist force. Such control methods can be applied to offshore cranes with low capacity and more maneuverability, such as cranes to move containers between vessels and ports. Adaptive control methods [71] and robust control methods [72] are proposed for trajectory tracking of the load. Anti-sway control methods are proposed for container cranes [70] to assist load position control and to reduce sway oscillation during trajectory tracking of the load. These control methods are designed for boom cranes with controllable boom angles and rotation angles or overhead cranes which can move in tracks.

2.3.3. LOAD STABILIZATION FOR HEAVY LIFT VESSELS

For large offshore cranes with high crane capacity, which are known as heavy lift vessels, the cranes have less maneuverability. Studies on control systems for load stabilization for such offshore cranes are limited. The state-of-the-art research on this topic which considers the ship motions, has modeled the ship-load dynamics only in 2 dimensions (i.e., in the vertical plane), and neglects movements in other dimensions [25, 26, 63, 64, 77, 90].

These studies design nonlinear models for under-actuated offshore boom cranes with the crane-load system in 3 DoFs, and provide nonlinear control methods for these under-actuated offshore boom cranes. The motions of the vessel are partly considered or predicted in the design procedure.

2.3.4. RESEARCH GAP

Literature	Heave Compensation	Load Stabilization	Heavy Loads	3 Dimensions
[19, 53, 66, 68, 73]	∘	-	-	∘
[15]	∘	-	∘	∘
[70–72]	∘	∘	-	∘
[25, 26, 63, 64, 77, 90]	-	∘	∘	-

Table 2.3: Literature review in load control systems: ∘ represents that the relative category is considered in the literature, and - denotes that the relative category is missing in the literature

According to Table 2.3, existing research activities either focus on only 2 dimensions, or work with mobile cranes with small capacities. However, in offshore heavy lift applications, the motions of the vessel is in 6 DoFs, with each DoF has its impact on the motion of the load. The load itself also moves in 6 DoFs. Control methods for crane-load systems in only two dimensions can therefore not be applied directly on heavy lift vessels, which normally work in 3 dimensions. Furthermore, the crane movements are less flexible comparing to cranes used for transporting containers in ports due to the very heavy loads and the large cranes.

Thus, to fill in the gap of the above-mentioned research studies, a nonlinear controller for offshore crane load in 3 DoFs with heavy load and very limited actuator is in need.

2.4. CONCLUSIONS

In this chapter, a literature review has been carried out to answer *Subquestion 1: What is the state of the art in smart offshore heavy lift operations?* Currently, most heavy lift vessels with DP systems require human input and encounter stability problems during offshore construction. Thus smart heavy lift vessels with few crew on board which can handle heavy lift operations would help with offshore installation work. By making heavy lift operations smart, the offshore heavy lift assignments need less waiting time due to the weather condition, and can allow construction work within a certain time period because of less communication time between crew.

For heavy lift vessels, becoming fully unmanned is more difficult than cargo vessels because of the complexity of offshore heavy lift constructions. The control of the crane and the control of the vessel position can be integrated and designed in a more intelligent way so that the vessel can handle a heavy lift assignment without human input to the crane control system or position control system. Based on the literature review, three main components and the integration of the components are missing in previous studies: An observer-based adaptive controller for position control of heavy lift vessels handling heavy loads during a complete offshore heavy lift assignment, nonlinear under-actuated control systems for crane load using fixed crane, and a monitoring system to detect the transferring between different construction modes.

To fill this gap, an automated system which consists of a mode detection system, an adaptive switching control for vessel position, and a nonlinear under-actuated load controller should be developed and integrated.

In the next chapter, we will focus on modelling of offshore heavy lift operations and provide a time-dependent model for the heavy lift problem.

3

MODELLING OF OFFSHORE HEAVY LIFT OPERATIONS

LITERATURE related to smart control of offshore heavy lift operation, and the research gap between practical needs and previous scientific studies have been explained in the previous chapter. In order to design and to simulate a smart system for offshore construction operations, the physical model of such operations needs to be studied.

In this chapter, we focus on the research *Subquestion 2: How to model dynamic positioned offshore heavy lift operations?* To answer this question, a detailed physical model of offshore heavy lift operation is provided.

The rest of the chapter is organized as followed: Section 3.1 introduces the two modes involved in offshore heavy lift operations. Section 3.2 shows the coordinate systems involved in this work. Section 3.3 provides the motion of the vessel under environmental disturbances and with crane force. Section 3.4.1 provides the motion of the load under environmental load. Section 3.5 presents the modelling of propulsion system and hydraulic winch. In section 3.7, simulation results of the physical model under with a PID DP controller are shown in figures. Conclusion of the chapter can be found in section 3.8. Parts of this chapter have been published in [105].

3.1. MODES IN OFFSHORE HEAVY LIFTING

During dynamic positioned offshore heavy lift operation, there are two different modes, each of which has its own physical features. Figure 1.4 shows the two offshore heavy lift construction modes under DP. In this chapter, the model will be described as in Mode 1 (i.e., when the load is on the platform with limitation of movements) and in Mode 2 (i.e., when the load is free-hanging in the air).

3.1.1. MODE 1: FIXED LOAD ON THE PLATFORM

When the vessel-load system is in Mode 1, the load is (partly) placed on the platform, and is not able to move or rotate in any direction. Thus the vessel could be seen as connected

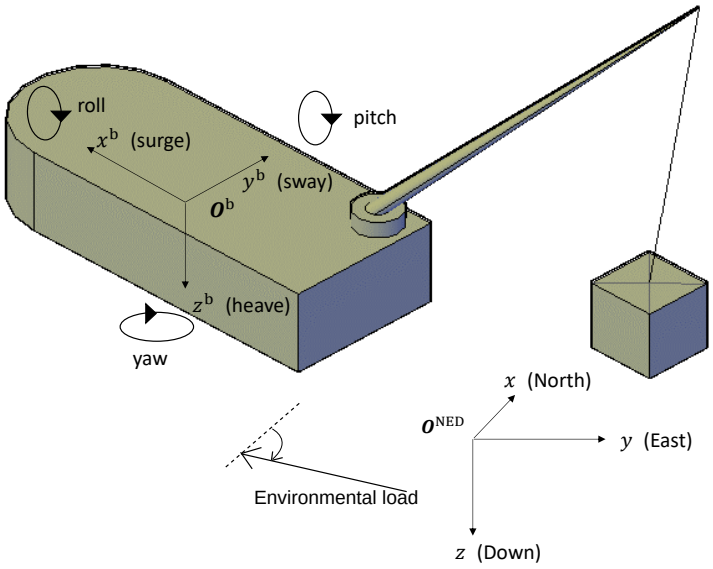

Figure 3.1: Illustration of the North-East-Down coordinate system and body-fixed coordinate system

to the platform via the crane wires. The hoist force in Mode 1 is changing according to the desired construction work. In the previous chapters, it has been pointed out that the number of offshore removal assignments is increasing due to environmental and financial reasons. So in this thesis, we will take offshore removal work as an example, which means that the tension is increasing from 0. A special case of Mode 1 is when the crane is not connected to the load (i.e. the hoist force is 0). When the load is fully lifted, the construction mode then switch to Mode 2.

3.1.2. MODE 2: FREE-HANGING LOAD

When the vessel-load system is in Mode 2, the load is free-hanging. In this case, the load is simplified as a non-dimensional mass point, and assumed to be able to move in 3 DoFs (i.e., in north, east, and down). The vessel is connected to the heavy load via crane wire.

3.2. COORDINATE SYSTEM

In this section, we will explain the coordinate systems that are used in the problem of automatic offshore heavy lift. Two coordinate systems are involved in this section: North-east-down coordinate system (NED) and body-fixed coordinate system (BODY) (Figure 3.1).

The 6 DoF motion of the research object in BODY frame can be expressed as:

- *Surge*: the movement of the vessel to the front or the aft.
- *Sway*: the movement of the vessel to the starboard or the portside.
- *Heave*: the up or down movement of the vessel.
- *Roll*: the rotation of the vessel around surge direction.
- *Pitch*: the rotation of the vessel around sway.
- *Yaw*: the heading of the vessel, which is also the rotation of the vessel around heave axial.

Let $\boldsymbol{\eta} = [x, y, z, \phi, \theta, \psi]^T$ describe the north, east and down positions, and rotation angles around north, east, and down axis of the research object respectively, and $\boldsymbol{\nu} = [u, v, w, p, q, r]^T$ describe the surge, sway, heave velocities, and roll, pitch, and yaw angular velocities of the research object in BODY respectively. Then the kinematic equation of motion are given by:

$$\dot{\boldsymbol{\eta}}(t) = \mathbf{J}_{\mathrm{b}}^{\mathrm{n}}(\phi, \theta, \psi)\boldsymbol{\nu}(t), \tag{3.1}$$

where $\mathbf{J}_b^n$ refers to the transformation matrix from BODY to NED, which is given by

$$\mathbf{J}_{\mathrm{b}}^{\mathrm{n}} = \begin{bmatrix} \mathbf{R}_{\mathrm{b}}^{\mathrm{n}}(\phi, \theta, \psi) & \mathbf{0} \\ \mathbf{0} & \mathbf{T}(\phi, \theta, \psi) \end{bmatrix}, \tag{3.2}$$

with

$$\mathbf{R}_{\mathrm{b}}^{\mathrm{n}}(\phi, \theta, \psi) = \begin{bmatrix} c_\psi c_\theta & -s_\psi c_\phi + c_\psi s_\theta s_\phi & s_\psi s_\phi + c_\psi c_\phi s_\theta \\ s_\psi c_\theta & c_\psi c_\phi + s_\phi s_\theta s_\psi & -c_\psi s_\phi + s_\theta s_\psi c_\phi \\ -s_\theta & c_\theta s_\phi & c_\theta c_\phi \end{bmatrix}, \tag{3.3}$$

$$\mathbf{T}(\phi, \theta, \psi) = \begin{bmatrix} 1 & s_\phi t_\theta & c_\phi t_\theta \\ 0 & c_\phi & -s_\phi \\ 0 & s_\phi / c_\theta & c_\phi / c_\theta \end{bmatrix}. \tag{3.4}$$

For floating vessels, the ϕ and θ angels are around 0 when the vessels are stabilized.

3.3. MOTION OF THE VESSEL

The motion of the vessel is given in this section. The proposed model should: 1) Be able to simulate the construction procedure with different heavy loads and under various environmental loads; 2) Be able to provide data related to the constructions; 3) Be a composite design such that the smart system can be implemented easily.

The following standard assumptions are made for the physical model of the vessel [31]:

Assumption 1: The vessel is symmetrical in starboard and port. The hydrodynamic added mass terms are fixed. This assumption holds for low-speed applications.

Assumption 2: The offset of the vessel in surge, sway and yaw is small as compared to the size of the ship. This is reasonable, because nowadays vessels are controlled by DP systems which keep the offsets within 5 meters.

Under the above mentioned assumptions, the motion of a crane vessel assuming 6 DoFs can be expressed as [31]:

$$(\mathbf{M}_{\mathrm{RB}}+\mathbf{M}_{\mathrm{A}})\dot{\boldsymbol{\nu}}_{\mathrm{v}}(t)+\mathbf{D}_{\mathrm{v}}\boldsymbol{\nu}(t)+\mathbf{C}_{\mathrm{v}}(\boldsymbol{\nu}(t))\boldsymbol{\nu}_{\mathrm{v}}(t)+\mathbf{G}_{\mathrm{v}}(\boldsymbol{\eta}(t))+\mathbf{g}_{\mathrm{v}}=\boldsymbol{\tau}_{\mathrm{thr}}(t)+\boldsymbol{\tau}_{\mathrm{e}}(t)+\boldsymbol{\tau}_{\mathrm{wires}}(t), \tag{3.5}$$

$$\dot{\boldsymbol{\eta}}_{\mathrm{v}}(t)=\mathbf{J}_{\mathrm{b}}^{\mathrm{n}}(\phi,\theta,\psi)\boldsymbol{\nu}_{\mathrm{v}}(t), \tag{3.6}$$

where $\boldsymbol{\nu}_{\mathrm{v}}=[u,v,w,p,q,r]^T$ is the vessel's velocity in the body-fixed coordinate system; $\boldsymbol{\eta}_{\mathrm{v}}=[x,y,z,\phi,\theta,\psi]^T$ is the vessel position in North-East-Down (NED) coordinate system; the signal $\boldsymbol{\tau}_{\mathrm{th}}\in\mathbb{R}^6$ is the force and moment given by the propulsion system; $\boldsymbol{\tau}_{\mathrm{e}}\in\mathbb{R}^6$ denotes the environmental forces and moments which are induced due to current, wind and wave; $\boldsymbol{\tau}_{\mathrm{wires}}=[\mathbf{F}_{\mathrm{wires}},\mathbf{T}_{\mathrm{wires}}]^T$ is the force and moment resulting from the crane load, with $\mathbf{F}_{\mathrm{wires}}\in\mathbb{R}^3,\mathbf{T}_{\mathrm{wires}}=\mathbf{r}_{\mathrm{ct}}\times\mathbf{F}_{\mathrm{wires}}$, where $\mathbf{r}_{\mathrm{ct}}\in\mathbb{R}^3$ is the vector from vessel's Center of Rotation to the crane tip; $\mathbf{M}_{\mathrm{RB}}\in\mathbb{R}^{6\times6}$ and $\mathbf{M}_A\in\mathbb{R}^6$ are the rigid body mass matrix and added mass matrix of the crane vessel; $\mathbf{D}_{\mathrm{v}}\in\mathbb{R}^{6\times6}$ is the damping matrix; $\mathbf{C}(\boldsymbol{\nu})$ is the Coriolis matrix, with z_{g} being the location of center of gravity wrt the location of center of origin in z; $\mathbf{g}_{\mathrm{v}}=[0,0,-M_{\mathrm{v}}g,0,0,0]^T$ is the mass gravity of the vessel, in which M_{v} is the vessel mass and g is the gravity acceleration; $\mathbf{G}_{\mathrm{v}}(\boldsymbol{\eta})$ refers to the hydrostatic force on the vessel [31].

In (3.5), the inertia matrix $\mathbf{M}_{\mathrm{RB}}$ is defined as:

$$\mathbf{M}_{\mathrm{RB}}=\begin{bmatrix} m_{\mathrm{v}}\mathbf{I}_{3\times3} & -m_{\mathrm{v}}\mathbf{S}(\mathbf{r}_{\mathrm{g}}^{\mathrm{b}}) \\ m_{\mathrm{v}}\mathbf{S}(\mathbf{r}_{\mathrm{g}}^{\mathrm{b}}) & \mathbf{I}_{\mathrm{v}} \end{bmatrix}, \tag{3.7}$$

with m being the weight of the vessel, and

$$\mathbf{I}_{\mathrm{v}}=\begin{bmatrix} I_x & I_{xy} & I_{xz} \\ I_{yx} & I_y & I_{yz} \\ I_{zx} & I_{zy} & I_z \end{bmatrix} \tag{3.8}$$

being the inertia moment matrix in roll pitch and yaw, $\mathbf{r}_{\mathrm{g}}^{\mathrm{b}}=[x_{\mathrm{g}},y_{\mathrm{g}},z_{\mathrm{g}}]^T$ is the vector from Center of Origin to Center of Gravity expressed in body frame, and the cross-product is defined as $\mathbf{a}\times\mathbf{b}=\mathbf{S}(\mathbf{a})\mathbf{b}$. The added mass and added inertia matrix of the vessel can be expressed as:

$$\mathbf{M}_{\mathrm{A}}=\begin{bmatrix} m_{11} & 0 & m_{13} & 0 & m_{15} & 0 \\ 0 & m_{22} & 0 & m_{24} & 0 & m_{26} \\ m_{31} & 0 & m_{33} & 0 & m_{35} & 0 \\ 0 & m_{42} & 0 & m_{44} & 0 & m_{46} \\ m_{51} & 0 & m_{53} & 0 & m_{55} & 0 \\ 0 & m_{62} & 0 & m_{64} & 0 & m_{66} \end{bmatrix}, \tag{3.9}$$

where m_{ij} can be expressed as: $m_{ij}=\rho\oint_S\varphi_i\frac{\partial\varphi_j}{\partial n}dS$, where ρ is the density of water, S is the wetted ship area, φ_i is the flow potential when the vessel is moving in ith direction. With the assumption that the vessel is symmetric in starboard and portside, the Coriolis

Matrix

$$\mathbf{C}(\boldsymbol{\nu}) = \begin{bmatrix} 0 & 0 & 0 & mz_{\mathrm{g}}r & mw & -mv \\ 0 & 0 & 0 & -mw & mz_{\mathrm{g}}r & mu \\ 0 & 0 & 0 & -m(z_{\mathrm{g}}p - v) & -m(z_{\mathrm{g}}q + u) & 0 \\ -mz_{\mathrm{g}}r & mw & m(z_{\mathrm{g}}p - v) & 0 & I_z r & -I_y q \\ -mw & -mz_{\mathrm{g}}r & m(z_{\mathrm{g}}q + u) & -I_z r & 0 & I_x p \\ mv & -mu & 0 & I_y q & -I_x p & 0 \end{bmatrix}. \tag{3.10}$$

3.4. DISTURBANCE MODEL

The disturbance model is designed to achieve a realistic heavy lift vessel model under environmental load and with measurement disturbance. In this section, the environmental disturbance and the measurement disturbance are provided.

3.4.1. ENVIRONMENTAL DISTURBANCE

The environmental loads acting upon the vessel can be categorized in three main categories:

- *Wave load* ($\boldsymbol{\tau}_{\mathrm{wave}}$): Including second order slowly varying wave load and first order high frequency disturbance.
- *Wind load* ($\boldsymbol{\tau}_{\mathrm{wind}}$): The wind load is related to the attack angle and the wind velocity.
- *Current load*: Current is simulated as a velocity that is relevant to vessel velocity.

Throughout this work, the environmental disturbances are subtracted from Chapter 8 in [31]. Consider the environmental disturbance, the motion of the vessel in BODY from Equation (3.5) can be rewritten as:

$$\begin{aligned}(\mathbf{M}_{\mathrm{RB}} + \mathbf{M}_A)\dot{\boldsymbol{\nu}}_{\mathrm{r}}(t) + \mathbf{D}_{\mathrm{v}}\boldsymbol{\nu}_{\mathrm{r}}(t) + \mathbf{C}_{\mathrm{v}}(\boldsymbol{\nu}_{\mathrm{r}}(t))\boldsymbol{\nu}_{\mathrm{r}}(t) + \mathbf{G}_{\mathrm{v}}(\boldsymbol{\eta}_{\mathrm{v}}(t)) + \mathbf{g}_{\mathrm{v}} \\ = \boldsymbol{\tau}_{\mathrm{thr}}(t) + \boldsymbol{\tau}_{\mathrm{wind}}(t) + \boldsymbol{\tau}_{\mathrm{wave}}(t) + \boldsymbol{\tau}_{\mathrm{wires}}(t),\end{aligned} \tag{3.11}$$

with

$$\boldsymbol{\nu}_{\mathrm{r}} = \boldsymbol{\nu}_{\mathrm{v}} - \boldsymbol{\nu}_{\mathrm{current}}, \tag{3.12}$$

where the vector $\boldsymbol{\nu}_{\mathrm{current}} \in \mathbb{R}^6$ denotes the current velocity.

Wind causes additional air pressure to the surface of the vessel. Wind load is related to the surface of the vessel, wind velocity and attack angle of the wind. For a vessel in DP control mode with zero speed over ground, the wind load can be defined as:

$$\boldsymbol{\tau}_{\mathrm{wind}}(t) = \begin{bmatrix} \frac{1}{2}\rho_{\mathrm{a}} V_{\mathrm{w}}^2(t) C_X(\gamma_{\mathrm{w}}(t)) A_{\mathrm{Fw}} \\ \frac{1}{2}\rho_{\mathrm{a}} V_{\mathrm{w}}^2(t) C_Y(\gamma_{\mathrm{w}}(t)) A_{\mathrm{Lw}} \\ \frac{1}{2}\rho_{\mathrm{a}} V_{\mathrm{w}}^2(t) C_Z(\gamma_{\mathrm{w}}(t)) A_{\mathrm{Fw}} \\ \frac{1}{2}\rho_{\mathrm{a}} V_{\mathrm{w}}^2(t) C_K(\gamma_{\mathrm{w}}(t)) A_{\mathrm{Lw}} H_{\mathrm{Lw}} \\ \frac{1}{2}\rho_{\mathrm{a}} V_{\mathrm{w}}^2(t) C_M(\gamma_{\mathrm{w}}(t)) A_{\mathrm{Fw}} H_{\mathrm{Fw}} \\ \frac{1}{2}\rho_{\mathrm{a}} V_{\mathrm{w}}^2(t)^2 C_N(\gamma_{\mathrm{w}}(t)) A_{\mathrm{Lw}} L_{\mathrm{oa}} \end{bmatrix}, \tag{3.13}$$

where ρ_a is air density, V_w is wind speed, which is modeled as a combination of slow-varying wind and wind gust, C_X, C_Y, C_Z, C_K, C_M, and C_N are nondimensional coefficients related to the attack angle of the wind. A_{Fw} and A_{Lw} are the frontal and lateral project areas above the waterline, while H_{Fw} and H_{Lw} are the centroids of the two areas, and γ_w is the attack angle of the wind. The wind angle is slowly varying around the mean wind angle. An example of wind load on the vessel during DP operation is shown in Figure 3.2 for the surge, sway and yaw directions with the mean wind speed of 2.5 m/s and a nominal wind angle of 210°.

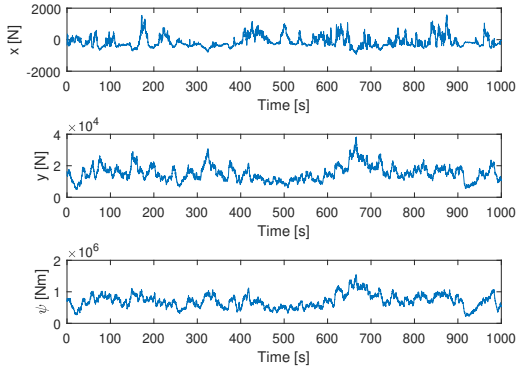

Figure 3.2: Example of wind load on the vessel ($\boldsymbol{\tau}_{wind}$) in surge, sway, and yaw

The wave load consists of a first order wave load and a second order slowly varying wave load.

$$\boldsymbol{\tau}_{wave}(t) = \boldsymbol{\tau}_{wave1}(t) + \boldsymbol{\tau}_{wave2}(t), \tag{3.14}$$

where the second order wave load $\boldsymbol{\tau}_{wave2}$ is modeled as a mean wave drift load without an oscillatory component. First order wave induced load $\boldsymbol{\tau}_{wave1}$ is a zero mean oscillation load. Where first order and second order wave loads can be found in [31]. Examples of the first order and second order wave loads with a significant wave height of 0.5m and a peak frequency of 0.8 rad/s with Jonswap spectrum are shown in Figure 3.3 and Figure 3.4. The overall environmental loads obtained from wave and wind effects are shown in Figure 3.5.

3.5. PROPULSION SYSTEM AND HYDRAULIC WINCH

Apart from the external disturbances, the propulsion systems and hydraulic winch on board of heavy lift vessels also have impacts on the smart control of heavy lift operations. In this section, the modelling of propulsion system and hydraulic winch is described.

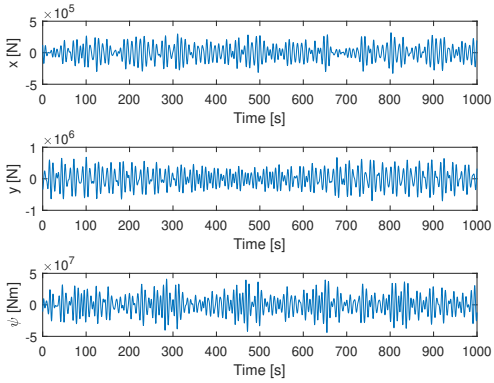

Figure 3.3: Example of first order wave load on the vessel ($\boldsymbol{\tau}_{\text{wave1}}$) in surge, sway, and yaw

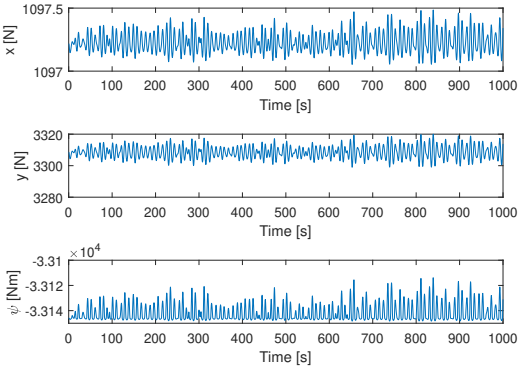

Figure 3.4: Example of second order wave load on the vessel ($\boldsymbol{\tau}_{\text{wave2}}$) in surge, sway, and yaw

3.5.1. PROPULSION SYSTEM

In order to properly capture the dynamics of the propulsion system, we use a mean-value first principle modelling approach to model the engine-propeller interaction. For more details on the modeling approach for each of the subcomponents, see [36]. The propulsion model in this work has been validated in [39]. We assume that there are 6 diesel engines and 6 propellers on board of the vessel.

The diesel engine is modeled as a four-stroke engine with six cylinders. The output tourque of the i-th diesel engine is:

$$M_{\text{bi}}(t) = M_{\text{b}}(t) = \frac{6H_{\text{e}}m_{\text{f}}k_{\text{LHV}}n_{\text{e}}(t)}{2\pi n_{\text{e}}(t)}, i \in \{1,2,3,4,5,6\}, \tag{3.15}$$

where M_{b} is the output torque, H_{e} is the efficiency, m_{f} is the fuel injection in mass, k_{LHV} is the ratio of energy and mass of the fuel, and n_{e} is the engine speed in rotation per

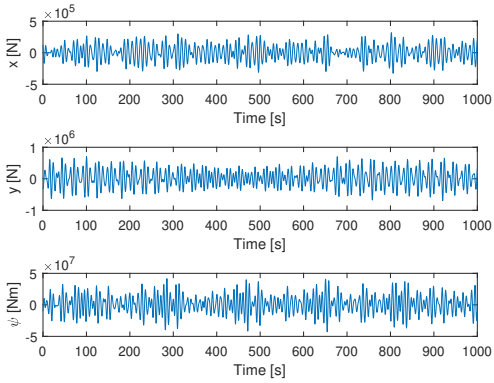

Figure 3.5: Example of wind load and wave load on the vessel ($\boldsymbol{\tau}_{\text{wind}}$+$\boldsymbol{\tau}_{\text{wave}}$) in surge, sway, and yaw

second, and i denotes the i-th diesel engine.

The thrust force for each thruster i is:

$$\bar{\tau}_{\text{thr}_i}(t) = \rho n_{\text{p}}(t)^2 D^4 K_t \tag{3.16}$$
$$= \rho n_{\text{p}}(t)^2 D^4 (K_{\text{ta}} J(t) + K_{\text{tb}}), \tag{3.17}$$

where ρ is the water density, n_{p} is the rate of revolution, D is the diameter of the propeller, K_{ta} and K_{tb} are two constant parameters, J is a nondimentional expression of the propeller which equals to $\frac{V_{\text{A}}(t)}{n(t)D}$, and $V_{\text{A}}(t)$ is the arriving water velocity.

Similarly, the propeller torque is:

$$T_{\text{p}_i}(t) = T_{\text{p}}(t) = \rho n_{\text{p}}(t)^2 D^5 K_{\text{q}} \tag{3.18}$$
$$= \rho n_{\text{p}}(t)^2 D^4 (K_{\text{qa}} J(t) + K_{\text{qb}}). \tag{3.19}$$

A shaft is connecting the diesel engine and the propeller.

$$n_{\text{p}_i} = n_{\text{p}} = \frac{n_{\text{e}}}{i_{\text{gb}}} \tag{3.20}$$
$$= \int \frac{M_{\text{b}} H_{\text{trm}} r_{\text{gb}} - T_{\text{p}}}{2\pi I_{\text{tot}}} dt, \tag{3.21}$$

where i_{gb} is the shaft transfer ratio, r_{gb} is the gearbox ratio, H_{trm} is the transmission efficiency, and I_{tot} is the total mass of inertia of the propulsion system.

For the overall thrust force on the vessel, the thruster force and moment in (3.5) can be calculated by

$$\boldsymbol{\tau}_{\text{thr}}(t) = \sum \boldsymbol{\tau}_{\text{thri}}(t), \tag{3.22}$$

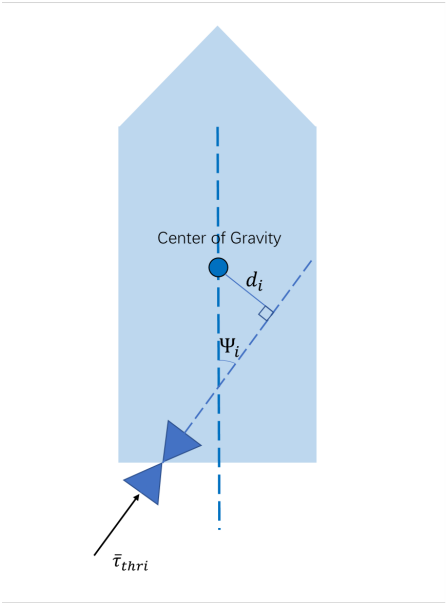

Figure 3.6: Calculation of thrust force for the i-th thruster ($\boldsymbol{\tau}_{\text{thri}}$)

where the summation is a vector summation, with

$$\boldsymbol{\tau}_{\text{thr}_i}(t) = \begin{bmatrix} c_{\Psi_\text{i}} \bar{\tau}_{\text{thr}_i}(t) \\ s_{\Psi_\text{i}} \bar{\tau}_{\text{thr}_i}(t) \\ 0 \\ 0 \\ 0 \\ -d_\text{i} \bar{\tau}_{\text{thri}}(t) \end{bmatrix}, \tag{3.23}$$

where Ψ_i and d_i denote the angle of the i-th thruster and the moment arm respectively, as shown in Figure 3.6.

3.5.2. HYDRAULIC CRANE

The crane winch is actuated by a hydraulic motor. The output torque of the hydraulic motor is [11]:

$$T(t) = \frac{\eta_{\text{hyd}} Q(t) \Delta p(t)}{2\pi}, \tag{3.24}$$

$$F_{\text{hoist}}(t) = \frac{T(t)}{r}, \tag{3.25}$$

where T is the torque output of the hydraulic motor, Q is the inlet flow rate per revolution, Δp is the pressure difference between the inlet flow and the outlet flow, η_{hyd} is the efficiency of the motor, r is the radius if the drum that the cable is wound on. During the simulation, the crane force is determined by the hydraulic motor. The hydraulic motor

is controlled by a PI controller, with the control gains K_{hp} and K_{hi}. Thus the PI controller in the hydraulic crane is:

$$Q(t) = K_{\text{hp}}\delta T(t) + K_{\text{hi}}\int \delta T(t)dt, \tag{3.26}$$

where δT is the difference between the desired torque and the actual torque. It is assumed that the pressure difference of the motor is constant in the simulation and only the inlet flow rate is changing to give desired crane force output.

3.6. LOAD MOTION

The load has different dynamics in 2 construction modes. In this section, the motion of the load in different modes is introduced.

3.6.1. MODE 1: FIXED POSITION

During Mode 1, the position of the load in NED is assumed to be fixed, i.e., $\dot{\boldsymbol{\eta}}_{\text{l}} = \mathbf{0}$. The lifting of the crane load is controlled by a hydraulic winch, i.e., F_{hoist} in (3.25) is controlled by a hydraulic winch [112]. The lifting process is not abrupt, but it evolves slowly.

3.6.2. MODE 2: FREE-HANGING

When the load is suspended, the vessel and the load can be seen as connected by hoist wires. As the load's rotation has less impact on the vessel's position stability compared to the impact from its position control, the load dynamics can be simplified to 3 DoFs:

$$\mathbf{M}_{\text{l}}\ddot{\boldsymbol{\eta}}_{\text{l}}(t) + \mathbf{D}_{\text{l}}\dot{\boldsymbol{\eta}}_{\text{l}}(t) + \mathbf{g}_{\text{l}} = \mathbf{F}_{\text{env}}(t) - \mathbf{R}_{\text{b}}^{\text{n}}(\boldsymbol{\Theta}(t))\mathbf{F}_{\text{wires}}(t), \tag{3.27}$$

where $\boldsymbol{\eta}_{\text{l}}$ is the position of the load in North-East-Down coordinate system (NED); $\mathbf{M}_{\text{l}} \in \mathbb{R}^{3\times3}$ is the mass matrix of the load; $\mathbf{D}_{\text{l}} \in \mathbb{R}^{3\times3}$ is the damping matrix of the load; $\mathbf{g}_{\text{l}} = [0, 0, -M_{\text{l}}g]^T$ is the mass gravity of the load, in which M_{l} is the mass of the load; $\boldsymbol{\Theta}$ is the rotation angles of the vessel; and $\mathbf{R}_{\text{b}}^{\text{n}} \in \mathbb{R}^{3\times3}$ is the rotation matrix from BODY to NED in 3 DoFs.

The force induced by the load can be expressed as:

$$\mathbf{F}_{\text{wires}}(t) = \frac{F_{\text{hoist}}(t)}{||\boldsymbol{\delta}_{\text{wires}}(t)||}\boldsymbol{\delta}_{\text{wires}}(t), \tag{3.28}$$

where

$$F_{\text{hoist}}(t) = \begin{cases} (K_{\text{wires}}\tilde{\delta}(t) + D_{\text{wires}}\dot{\tilde{\delta}}(t)), & \text{if } \tilde{\delta}(t) > 0; \\ 0, & \text{if } \tilde{\delta}(t) \leq 0. \end{cases} \tag{3.29}$$

In Equation (3.29),

$$\tilde{\delta}(t) = ||\boldsymbol{\delta}_{\text{wires}}(t)|| - ||\boldsymbol{\delta}_{\text{wires}}(0)|| \tag{3.30}$$

is the elastic elongation of the crane wires;

$$\boldsymbol{\delta}_{\text{wires}}(t) = \mathbf{p}_{\text{l}}(t) - \mathbf{p}_{\text{ct}}, \tag{3.31}$$

with $\mathbf{p}_{\text{ct}} = [x_{ct}, y_{ct}, z_{ct}]^T$ being the constant vector that denotes the position of crane-tip and $\mathbf{p}_{\text{l}} = [x_{\text{l}}, y_{\text{l}}, z_{\text{l}}]^T$ being the load position in vessel's body-fixed coordinate system, which satisfies

$$\mathbf{p}_{\text{l}} = \mathbf{R}_{\text{n}}^{\text{b}}(\phi, \theta, \psi)(\boldsymbol{\eta}_{\text{l}} - \boldsymbol{\eta}_3), \tag{3.32}$$

where $\boldsymbol{\eta}_3 = [x, y, z]^T$ is the vector of the first three elements of $\boldsymbol{\eta}_{\text{v}}$, and $\mathbf{R}_{\text{n}}^{\text{b}}$ is the transpose matrix of $\mathbf{R}_b^n$.

3.7. SIMULATION OF THE PHYSICAL MODEL

A simulation is made to assess the vessel-load system during a complete offshore construction. In this section, we present a simulation with load of 2400 tonnes. The simulations are made under sea state 2 where sea state is an oceanographic way to describe the condition of the water surface on a large scale with respect to wind and waves at certain location and time.The simulations in this section are made with a significant wave height of 0.5 meter, current speed of 0.6 m/s, and wind velocity of 2.5 m/s. The angles of the environmental loads is 120°. A PID controller for the DP system is applied to assist the simulated offshore removal process. The setpoint of the PID controller is set to $[0,\ 0,\ 0]^T$.

The whole removal process lasts 800s and contains four steps:

- *0-50*s: The vessel is connected to the structure to be removed but the removal process is not ongoing (Mode 1).
- *50-600*s: The vessel starts to remove the structure gradually with the tension increasing in the crane wires (Mode 1).
- *600-800*s: The vessel removes the structure, with the structure hanging on the crane (Mode 2).

The simulation results are shown in Figure 3.7 and Figure 3.8. Simulation results show that under traditional PID controller and without load control systems.

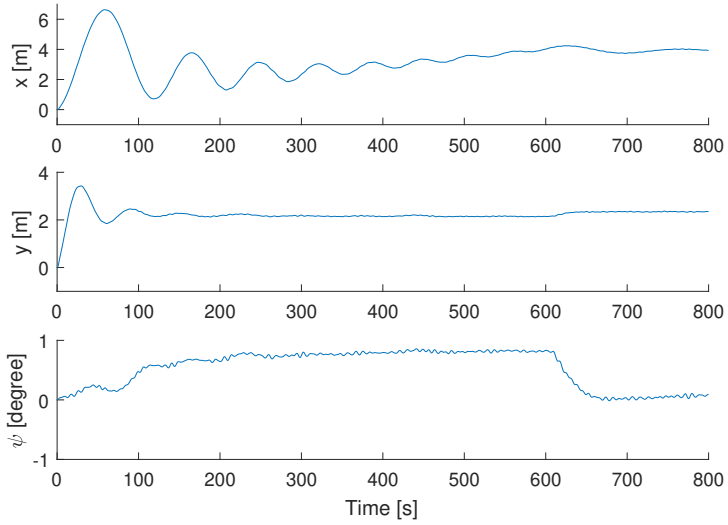

Figure 3.7: Simulation of the physical model with PID controller (vessel position $\boldsymbol{\eta}_{\mathrm{v}}$ in x, y, and yaw angle in ψ)

According to Figure 3.7, the vessel position is not stable at the beginning of the simulation. This is because the controller is tuned for Mode 2.

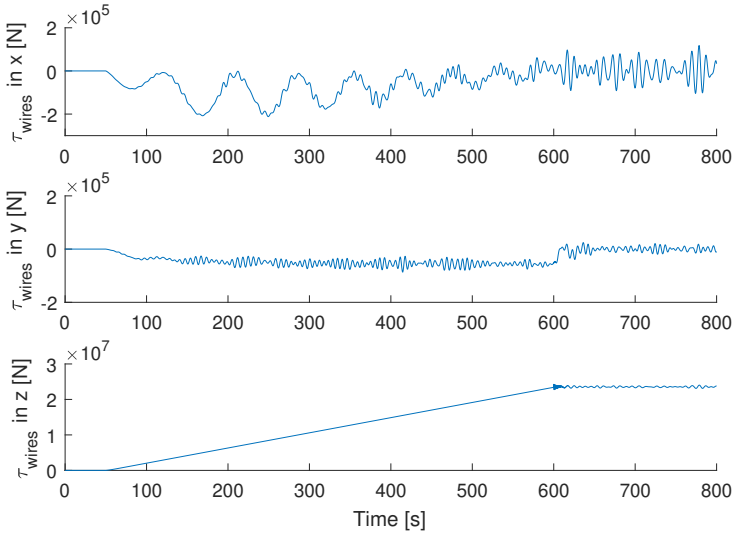

Figure 3.8: Simulation of the physical model with PID controller (crane force $\boldsymbol{\tau}_{\mathrm{wires}}$ in x, y, and z)

Crane force in surge, sway, and heave is illustrated in Figure 3.8. Due to the oscilla-

tion of the vessel position in surge direction, the crane force is also oscillating in surge. After 600s, the force in heave direction is not stabilized because the position of the free-hanging load is not under control. The oscillation in the load position results in the oscillation in the crane force.

In this simulation, the maximum offset of the vessel is 6.63m, as shown in Table 3.1. Such offset is not sufficient for offshore heavy lift operations, as the clearance between the edge of the vessel and the platform can be smaller than 5m. A good position control system should be able to maintain the position of the vessel with a maximum offset of less than 1m to avoid incidents.

Direction	North	East	Yaw
Maximum offset	6.63m	3.42m	0.86°

Table 3.1: The maximum offset in north, east, and yaw during offshore heavy lift operation controlled by a PID DP controller

3.8. CONCLUSIONS

In this chapter, a model of the dynamic positioned heavy lift vessel during offshore heavy lift is proposed. The contents in this chapter answer *Subquestion 2: How to model dynamic positioned offshore heavy lift operations?* The physical model of the vessel is in 6 DoFs, with a 3 DoF load model. The model consists of vessel dynamics, load dynamics, environmental disturbance, propulsion system, hydraulic winch and the transformation between BODY frame and NED frame. A simulation with the physical system shows a position and heading change at the time of the mode switch.

In the next chapter, a switching robust DP controller is designed for the offshore construction assignment. The controller is based on the physical model proposed in this chapter, and is assessed with the proposed model.

4

ROBUST SWITCHING DP CONTROL DURING OFFSHORE HEAVY LIFT

THE modelling of the offshore heavy lift operations was proposed in Chapter 3. Previous studies show that the position control using PID controller during such operations has a maximum offset of 6m, which means that an incident might happen during the construction. Thus a stable controller is described in this chapter to keep the vessel in position during offshore heavy lift operations.

In this chapter, we focus on the following research questions: *Subquestion 3: How to solve the DP stability and robustness problem for heavy lift operations during Mode 1?*, and *Subquestion 4: How to design a DP controller for heavy lift operations considering the mode switching during the operation?* A robust controller is designed for the vessel under Mode 1. Based on this robust controller, a switching controller is proposed for offshore heavy lift construction including Mode 1 and Mode 2. The stability of each controller is explained separately. Both control methods are assessed using simulations under different settings with the model from Chapter 1.

In this chapter, we first introduce the control objectives in Section 4.1. Then in Section 4.2 the robust controller for mode 1 is proposed with stability analysis. In Section 4.3, a switching DP controller is designed for offshore heavy lift operation consider mode switch. Simulation results are given in Section 4.4. In Section 4.5, conclusions of this chapter are given. Parts of this chapter have been published in [105–107].

4.1. PROBLEM DEFINITION AND CONTROL OBJECTIVE

Studies have reported cases of instability of DP systems during offshore operation caused by unmodelled dynamics, such as large oscillating tension through the crane wires [4, 29, 104]. Previous solutions on DP for heavy lift vessels mainly focus on two aspects: i) Feedforward or tuning solutions applied to the observer or the controller [100]; ii) Robust control methods that tackle the crane forces as unknown uncertainties [21]. For the first category, the ship propellers can have difficulties to handle the oscillation of the feed-

forward force. For the latter category, the control methods are not designed for heavy lift vessels, and did not consider large uncertain forces during heavy lift operations. For DP control of heavy lift vessels, there are two main challenges left: to design an observer-based controller that can deal with large oscillating force during Mode 1; and to design a controller that can handle both Mode 1, Mode 2, and the switching of the modes.

4.1.1. DP MODEL IN 3 DOFS

Usually, a DP system can only control the movement of vessels in surge, sway and yaw. Therefore, DP literature commonly adopts the following 3 DoFs (i.e. in surge, sway, and yaw direction) vessel model that is simplified from (3.5) and (3.6) [31, 106]:

$$\dot{\boldsymbol{\eta}}(t) = \mathbf{R}_3(\psi(t))\boldsymbol{\nu}(t), \tag{4.1}$$

$$\mathbf{M}\dot{\boldsymbol{\nu}}(t) = -\mathbf{D}\boldsymbol{\nu}(t) + \boldsymbol{\tau}_{c\sigma}(t) + \boldsymbol{\tau}(t) + \boldsymbol{\tau}_{l\sigma}(t) + \bar{\mathbf{d}}(t), \tag{4.2}$$

where $\mathbf{R}_3(\psi) = \begin{bmatrix} \cos(\psi) & -\sin(\psi) & 0 \\ \sin(\psi) & \cos(\psi) & 0 \\ 0 & 0 & 1 \end{bmatrix}$, with the assumption that θ, and ϕ close to 0, the state $\boldsymbol{\eta} = [x, y, \psi]^T$ comprises of north position, east position and heading angle of the ship in earth-fixed coordinate system, respectively; $\boldsymbol{\nu} = [u, v, r]^T$ is the vessel velocity/angular velocity in body-fixed coordinate system; $\overline{\mathbf{M}} = \mathbf{M}_{RB} + \mathbf{M}_A$ from (3.11)), and $\mathbf{M} \in \mathbb{R}^{3\times3}$ contains the surge, sway, and yaw elements in $\overline{\mathbf{M}}$; similarly, $\mathbf{D} \in \mathbb{R}^{3\times3}$ is the 3 DoFs version of $\mathbf{D}_v$; $\bar{\mathbf{d}}(t) \in \mathbb{R}^3$ denotes bounded external disturbances including environmental disturbance and unmodeled dynamics; $\boldsymbol{\tau} \in \mathbb{R}^3$ is the generalized control input to be designed; $\boldsymbol{\tau}_{c\sigma} \in \mathbb{R}^3$ denotes the force from the crane winch controlling the crane wires during Mode 1; $\boldsymbol{\tau}_{l\sigma} \in \mathbb{R}^3$ denotes bounded force from the hanging of the load during Mode 2; $\sigma \in 0, 1, 2$ denotes the operation phases, which is introduced in Table 4.1.

Table 4.1: The Three Phases in Offshore Heavy-Lift Operation, with $\mathbf{F}\boldsymbol{\eta}$ denotes the mooring force with $\mathbf{F} \in \mathbb{R}^{3\times3}$ being the positive definite time-varying spring coefficient related to the tension in crane wires F_{crane}, which is a linearized notation for $\mathbf{F}_{\text{crane}}$ in surge, sway, and yaw.

Mode 1	Phase 0	$\boldsymbol{\tau}_{c0} = \mathbf{0},\ \boldsymbol{\tau}_{l0} = \mathbf{0}.$
	Phase 0	$\boldsymbol{\tau}_{c1} = -\mathbf{F}\boldsymbol{\eta},\ \boldsymbol{\tau}_{l1} = \mathbf{0}.$
Mode 2	Phase 1	$\boldsymbol{\tau}_{c2} = \mathbf{0},\ \boldsymbol{\tau}_{l2} \neq \mathbf{0}$

We first introduce the phases in Table 4.1. With construction Phase 0 represents a special condition of Mode 1, when the vessel is not connected to any load, and the hoist force equals zero. During Phase 0, the vessel is attached to the fixed load via crane wires, and the horizontal forces and moment generated from the crane wires can be simplified as a mooring force $-\boldsymbol{F\eta}$ as shown in the next section.

4.1.2. CALCULATION OF MOORING STIFFNESS

In this section, the details of the linearization of the mooring stiffness $\boldsymbol{F}$ are provided. During moored dynamic positioning, there is additional stiffness added to the vessel

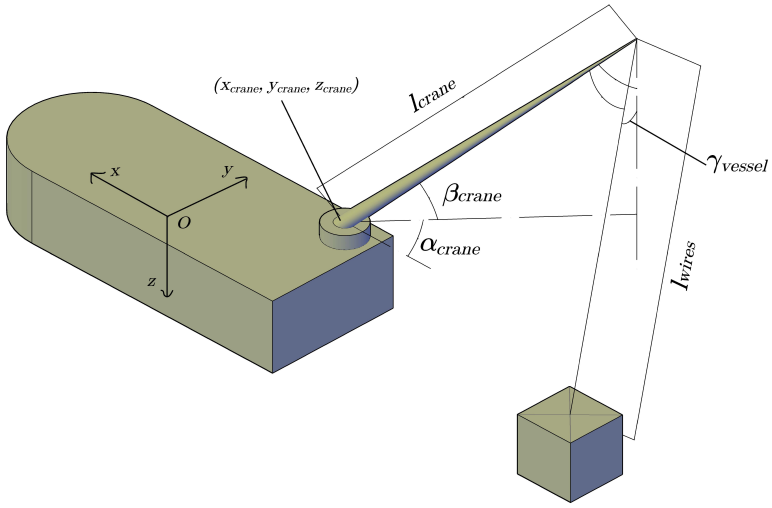

Figure 4.1: Illustration of the angles related to the calculation of mooring stiffness, where γ_{vessel} is the angle between the crane wires an z-axis in NED coordinate system

because of the crane force. The vessel during mooring status can be seen as added with extra horizontal stiffness.

The damping term of the wires can be neglected comparing to the stiffness of the wires [105]. The setpoint of the vessel position is chosen where the crane wires are vertical (i.e., $\gamma_{\text{vessel}} = 0$), and the horizontal crane force is $\mathbf{0}$. Assuming that the offset of the vessel comparing to the setpoint position is small, the moored crane force can be approximated as the influence of both the offset and a changing mooring stiffness:

$$F_{\text{hoist}} = K_{\text{wires}}\tilde{\delta}. \tag{4.3}$$

Assuming that the position of the vessel is controlled by a DP system with a small offset of x, y, and ψ, the roll and pitch angles are small and their influence on the crane force can be neglected, we have the following equations:

$$\sin\gamma_{\text{vessel}} = \frac{\sqrt{\Delta x^2 + \Delta y^2}}{||\boldsymbol{\delta}_{\text{wires}}(t)||}. \tag{4.4}$$

The horizontal component of F_{hoist} can be obtained by

$$F_{\text{horizon}} = F_{\text{hoist}} \sin\gamma_{\text{vessel}}, \tag{4.5}$$

where γ_{vessel} is the angle of the crane wires with respect to the Z-axis as shown in Figure 4.1, Δx is the surge position of the vessel comparing to the nominal position. Δy is the

sway position of the vessel comparing to the nominal sway position. In our case, the nominal position is **0**, i.e., $\Delta x = x, \Delta y = y$. Thus the mooring stiffness $\boldsymbol{F}$ is defined as the horizontal stiffness of the vessel added by the crane wires:

$$\boldsymbol{F}_{\text{horizon}} = \boldsymbol{F}\boldsymbol{\eta}. \tag{4.6}$$

During dynamic positioning, the vessel's position and velocity should be estimated as well as the horizontal force from the crane wires. In this section, a joint state-parameter estimator is made. The estimated parameters are the mooring stiffness from the crane force and the states to be estimated include the position and velocity of the vessel in surge, sway, and yaw. For the crane force in the surge and sway direction, the mooring stiffness can be simplified when the offset of vessel position is small.

Define the mooring stiffness in surge and sway as K_{surge} and K_{sway} respectively, then

$$K_{\text{surge}} = K_{\text{sway}} = K_0 = \frac{F_{\text{surge}}}{x} = \frac{F_{\text{horizon}}}{\sqrt{x^2+y^2}}, \tag{4.7}$$

we have

$$K_0 = F_{\text{hoist}} \frac{\sqrt{x^2+y^2}}{||\boldsymbol{\delta}_{\text{wires}}(t)||\sqrt{x^2+y^2}} = \frac{F_{\text{hoist}}}{||\boldsymbol{\delta}_{\text{wires}}(0)|| + \frac{F_{\text{hoist}}}{K_{\text{wires}}}}. \tag{4.8}$$

Thus the horizontal mooring stiffness in surge and sway direction can be approximated as:

$$K_0 \approx \frac{F_{\text{hoist}}}{||\boldsymbol{\delta}_{\text{wires}}(0)||}, \tag{4.9}$$

where $||\boldsymbol{\delta}_{\text{wires}}(0)||$ is the initial length of the crane wires at the beginning of the construction work.

If the coupling between sway force and yaw moment is taken into consideration, the approximated mooring stiffness matrix $\boldsymbol{F}$ can be written as:

$$\boldsymbol{F} = \begin{bmatrix} K_0 & 0 & 0 \\ 0 & K_0 & -R_{\text{ct}}K_0 \\ 0 & -R_{\text{ct}}K_0 & R_{\text{ct}}^2 K_0 \end{bmatrix} \boldsymbol{R}_3^T(\psi), \tag{4.10}$$

where R_{ct} is projection of the vector from Center of Gravity of the vessel to the crane tip on the horizontal plane.

Based on the construction work scenario depicted in Figure 1.4, the crane-vessel system (4.1)-(4.2) undergoes at least three main phase changes summarized in Table 4.1 and denoted with the terms Phase 0 "No load", Phase 1 "Mooring" and Phase 2 "Free-hanging". During Phase 1 the crane wires are attached to the load, resulting in a spring-type force (mooring force). During Phase 2 the load acts as an external disturbance. The load will also affect the mass matrix in Phases 2 and 3, such influence on the mass matrix is treated as part of uncertain dynamics.

To deal with the aforementioned challenges, DP controllers are designed for offshore construction under uncertain forces. First a Lyapunov-based DP method is proposed

to address this challenge. Not only stability is analyzed in the presence of uncertainties, but also indicators are provided to design the DP system and tune its performance. Then based on the robust controller, a novel switching control perspective is proposed which overcomes the stability, robustness and filtering limitations of the state of the art.

Remark 4.1 (3 DoFs vs. 6 DoFs)**.** *Reducing a system from 6 to 3 DoF clearly introduced some unmodelled dynamics. Modelling features in* (3.11) *as compared to* (4.12) *are:*

- *The terms* $\mathbf{C}_\mathrm{v}, \mathbf{G}_\mathrm{v}$ *and* $\mathbf{g}_\mathrm{v}$ *from* (3.11) *act as unmodelled dynamics (cf. part of* $\mathbf{d}(t)$*) for the proposed controller in* (4.2)*.*
- *The unknown thruster dynamics also act as unmodelled dynamics (cf. part of* $\mathbf{d}$*).*
- *In addition to the simplified spring-based mooring components (cf.* $\mathbf{F}$ *as in Table 4.1),* (3.11) *allows to model the damping components of the crane wires.*

The proposed DP system must be designed in such a way to tackle all such uncertainties. Therefore, the simulations using the 6 DoF will allow to test the performance of the proposed design in representative dynamical uncertain scenarios.

4.2. ROBUST OBSERVER-BASED CONTROLLER FOR MODE 1

While the performance of a DP system is better validated on realistic six DoFs dynamics as in (3.5) and (3.11), the design of DP controller is conventionally performed on three DoFs dynamics. Under the assumption that the vessel has a low velocity and acceleration, the DP system dynamics in Mode 1 are commonly represented along 3 DoFs as in [31]:

$$\dot{\boldsymbol{\eta}} = \mathbf{R}_3(\psi)\boldsymbol{\nu}, \tag{4.11}$$

$$\mathbf{M}\dot{\boldsymbol{\nu}} = -\mathbf{D}\boldsymbol{\nu} - \mathbf{F}\boldsymbol{\eta} + \boldsymbol{\tau} + \bar{\mathbf{d}}, \tag{4.12}$$

with $\boldsymbol{\tau}_c = -\mathbf{F}\boldsymbol{\eta}$, $\boldsymbol{\tau}_l = \mathbf{0}$, where $\boldsymbol{\tau} \in \mathbb{R}^3$ is the generalized control input. Without loss of generality, we consider $\boldsymbol{\eta}_\mathrm{d} = [0,0,0]^T$ to be the desired position of the vessel.

4.2.1. UNCERTAINTY SETTING

Henceforth, for compactness, $\mathbf{R}_3(\psi)$ will be represented as $\mathbf{R}_3$, and the system dynamics (4.11)-(4.12) is represented as

$$\dot{\boldsymbol{\eta}} = \mathbf{R}_3\boldsymbol{\nu}, \tag{4.13}$$

$$\dot{\boldsymbol{\nu}} = -\mathbf{A}_1\boldsymbol{\eta} - \mathbf{A}_2\boldsymbol{\nu} + \mathbf{M}^{-1}\boldsymbol{\tau} + \mathbf{d}, \tag{4.14}$$

where $\mathbf{A}_1 \triangleq \mathbf{M}^{-1}\mathbf{F}, \mathbf{A}_2 \triangleq \mathbf{M}^{-1}\mathbf{D}$ and $\mathbf{d} \triangleq \mathbf{M}^{-1}\bar{\mathbf{d}}$. Note that in crane vessels the exact values of the positive definite matrices $\mathbf{A}_1$ and $\mathbf{A}_2$ [31] are not known. The following assumption highlights the nature of uncertainties considered in this work for dynamics (4.12):

Assumption 4.1 (Uncertainty)**.** $\mathbf{A}_\mathrm{i}$*'s can be decomposed into two positive definite matrices* $\hat{\mathbf{A}}_\mathrm{i}$ *(nominal part) and* $\tilde{\mathbf{A}}_\mathrm{i}$ *(unknown perturbation), i.e.* $\mathbf{A}_\mathrm{i}(t) = \hat{\mathbf{A}}_\mathrm{i} + \tilde{\mathbf{A}}_\mathrm{i}(t)$*. Quantities available for control designs are: the maximum perturbation ranges* $\Delta\mathbf{A}_\mathrm{i} \in \mathbb{R}_{3\times3}$ *(such that* $||\Delta\mathbf{A}_\mathrm{i}|| \geq ||\tilde{\mathbf{A}}_\mathrm{i}(t)|| \ \forall t$*); the mass matrix* $\mathbf{M}$*; the upper bound* $\Delta\mathbf{d} \in \mathbf{R}_3$ *on the external disturbances (such that* $||\Delta\mathbf{d}|| \geq ||\mathbf{d}(t)|| \ \forall t$*).*

Remark 4.2 (Robustification philosophy)**.** *The perturbation ranges* $\Delta\mathbf{A}_i$ *define the worst-case uncertainty in crane induced and hydrodynamic damping forces. The upper bound* $\Delta\mathbf{d}$ *defines the worst-case environmental conditions. The knowledge of these terms is required if one aims at proving stability of the DP system in the worst-case uncertainty settings. Differently from mooring and hydrodynamic damping terms, the mass* $\mathbf{M}$ *of a vessel is typically known with little uncertainty. In fact, uncertainty in mass matrix arise from movements in water with high acceleration or deceleration (added mass terms), which are negligible during DP operation [31].*

4.2.2. OBSERVER-BASED ROBUST CONTROLLER DESIGN

Observer-based control is very common in DP as a way to filter high-frequency disturbances [32, 97]. An observer is a software-based system that provides an estimation of the internal state of a real system using its input and output signals. Construction of observers for positions and velocities via (4.15)-(4.16) helps to filter out high-frequency terms from the control action (4.17) and, thereby, helps to ease the thruster action.

Let us define $\tilde{\boldsymbol{\eta}} \triangleq \boldsymbol{\eta} - \hat{\boldsymbol{\eta}}$ and $\tilde{\boldsymbol{\nu}} \triangleq \boldsymbol{\nu} - \hat{\boldsymbol{\nu}}$; where $\hat{\boldsymbol{\eta}}$ and $\hat{\boldsymbol{\nu}}$ are the observed (filtered) values of $\boldsymbol{\eta}$ and $\boldsymbol{\nu}$ respectively, and $\tilde{\boldsymbol{\eta}} \triangleq \boldsymbol{\eta} - \hat{\boldsymbol{\eta}}$, $\tilde{\boldsymbol{\nu}} \triangleq \boldsymbol{\nu} - \hat{\boldsymbol{\nu}}$. Assuming no measurement noise, the proposed DP design can be described as:

$$\dot{\hat{\boldsymbol{\eta}}} = -\mathbf{K}\hat{\boldsymbol{\eta}} + \mathbf{K}_1\tilde{\boldsymbol{\eta}} + \mathbf{R}_3\hat{\boldsymbol{\nu}}, \tag{4.15}$$

$$\dot{\hat{\boldsymbol{\nu}}} = -\hat{\mathbf{A}}_1\hat{\boldsymbol{\eta}} - \hat{\mathbf{A}}_2\hat{\boldsymbol{\nu}} + \mathbf{M}^{-1}\boldsymbol{\tau} + \mathbf{K}_2\hat{\boldsymbol{\eta}}, \tag{4.16}$$

$$\boldsymbol{\tau} = \mathbf{M}\{(\hat{\mathbf{A}}_1 - \mathbf{K}_2 - \mathbf{R}_3^T)\hat{\boldsymbol{\eta}} + (\hat{\mathbf{A}}_2 - (\rho + \rho_1))\hat{\boldsymbol{\nu}}\}. \tag{4.17}$$

In order to handle the worst-case uncertainty settings, the observer and control gains $\mathbf{H}, \mathbf{K}, \mathbf{K}_1, \mathbf{K}_2, \rho_1$ and ρ should be properly designed. The design of such gains is proposed as:

$$\lambda_{\min}(\mathbf{K}_1) > ||\frac{1}{2\beta}(\Delta\mathbf{A}_1 - \mathbf{K}_2)^T\mathbf{H}^{-1}(\Delta\mathbf{A}_1 - \mathbf{K}_2)||, \tag{4.18}$$

$$\lambda_{\min}(\mathbf{K}) > ||\frac{1}{2\beta}(\Delta\mathbf{A}_1 + \mathbf{K}_2)^T\mathbf{H}^{-1}(\Delta\mathbf{A}_1 + \mathbf{K}_2)||, \tag{4.19}$$

$$\rho > ||(1/2\beta)\Delta\mathbf{A}_2^T\mathbf{H}^{-1}\Delta\mathbf{A}_2|| + ||\Delta\mathbf{d}||, \tag{4.20}$$

$$\rho_1(t) = \alpha\int_0^t ||(\mathbf{K}_1 + \mathbf{K})||||\hat{\boldsymbol{\eta}}(\zeta))||||\tilde{\boldsymbol{\eta}}(\zeta)||\mathrm{d}\zeta, \tag{4.21}$$

$$\mathbf{K}_2(t) = -\hat{\mathbf{A}}_1 + \mathbf{R}_3^T(\psi), \tag{4.22}$$

where $\lambda_{\min}(\mathbf{K})$ denotes the minimum eigen value of the matrix $\mathbf{K}$, $\alpha > 1$; β and $\mathbf{H}$ denote a positive scalar and a positive definite matrix that must satisfy:

$$||(3\beta/2)\mathbf{H}|| < \lambda_{\min}(\hat{\mathbf{A}}_2). \tag{4.23}$$

Remark 4.3 (Selection of gains)**.** *According to Assumption 4.1,* $\hat{\mathbf{A}}_2$ *is defined based on the nominal knowledge of* $\mathbf{A}_2$*. Therefore, condition (4.23) provides a selection criterion for* β *and* $\mathbf{H}$*, which in turn guides to select the other gains* $\mathbf{K}_1, \mathbf{K}, \rho$ *and* ρ_1 *from* (4.18), (4.19), (4.20) *and* (4.21)*, respectively. Note that* $\mathbf{R}_3$ *is an orthogonal matrix with* $||\mathbf{R}_3|| = 1\ \forall\psi$*; thus, one can easily compute the upper bounds of the right hand sides in* (4.18) *and* (4.19) *when designing* $\mathbf{K}_1$ *and* $\mathbf{K}$*.*

4.2.3. PRECOMPENSATION FOR UNKNOWN THRUSTER DYNAMICS

In reality, the propulsion system usually has an unknown time delay and a limitation of propulsion rate which and be modelled approximately as a low pass filter. Such low pass filter introduces unmodelled dynamics which, if left unattended, might lead to unstable closed-loop behaviour. In view of such scenario, inspired from [82], we employ an artificial delay based precompensation method as:

$$\bar{\tau}_{\mathrm{i}}(t) = N_{\mathrm{i}}\tau_{\mathrm{i}}(t) - \overline{N}_{\mathrm{i}}\tau_{\mathrm{i}}(t-h),\ i = 1,2,3, \tag{4.24}$$

where $\boldsymbol{\tau} = \{\tau_1,\ \tau_2,\ \tau_3\}$; $\bar{\tau}_{\mathrm{i}}$ denotes the input to the thrust allocator; N_{i} and $\bar{N}_{\mathrm{i}}$ are two positive scalars, $\tau_{\mathrm{i}}(t-h)$ requires to artificially use of a past control input of previous sampling time (being $h > 0$ the so-called artificial time delay).

To design N_{i} and $\overline{N}_{\mathrm{i}}$, one notes that boundedeness of $\boldsymbol{\tau}(t)$ will be established. Therefore, given an h, one needs to design N_{i} and $\bar{N}_{\mathrm{i}}$ such that boundedness of $\bar{\tau}_{\mathrm{i}}$ can be established from the boundedness of $\boldsymbol{\tau}(t)$. As the sampling time of DP system is of typically small (order of hundredth of a second), $\tau_{\mathrm{i}}(t-h)$ can be approximated via Padé approximation:

$$\begin{aligned} \bar{\tau}_{\mathrm{i}}(s) &= N_{\mathrm{i}}\tau_{\mathrm{i}}(s) - \bar{N}_{\mathrm{i}}\frac{-\frac{h}{2}s+1}{\frac{h}{2}s+1}\tau_i(s) \\ \Rightarrow \frac{\bar{\tau}_{\mathrm{i}}(s)}{\tau_{\mathrm{i}}(s)} &= \frac{(N_{\mathrm{i}}+\bar{N}_{\mathrm{i}})hs + 2(N_{\mathrm{i}}-\bar{N}_{\mathrm{i}})}{hs+2}, \end{aligned} \tag{4.25}$$

where s is the Laplace operator. One can verify that *any choice* satisfying $0 < \bar{N}_{\mathrm{i}} < N_{\mathrm{i}}$ will lead to minimum phase dynamics for (4.25), i.e. the pre-compensation scheme (4.25) will not invalidate the closed-loop stability, described in Section 4.2.4.

Remark 4.4 (Available measurements)**.** *The proposed observer-based robust controller requires position measurements but no velocity measurements. The practical reason for this choice is that velocity measurements are more 'noisy' (i.e. with high-frequency noise) and its usage in DP controllers it not suggested in literature [31, 32].*

4.2.4. STABILITY ANALYSIS

We first give the stability analysis of the proposed controller and consequently, we highlight some key performance indicators to drive the selection of the design parameters.

Definition 4.1 (Globally Uniformly Ultimately Bounded Stability [51])**.** *System* (4.13)-(4.14) *is globally uniformly ultimately bounded if there exists a convex and compact set* Υ *such that for every initial condition* $(\boldsymbol{\eta}(0), \boldsymbol{\nu}(0))$*, there exists a finite* $T(\boldsymbol{\eta}(0), \boldsymbol{\nu}(0))$ *such that* $(\boldsymbol{\eta}(t), \boldsymbol{\nu}(t)) \in \Upsilon$ *for all* $t \geq T$.

Theorem 4.1. *Under Assumption 4.1, the system* (4.13)-(4.14) *employing the controller (4.15)-(4.17) remains Uniformly Ultimately Bounded (UUB) if, for a given* $\beta > 0$ *and* $\mathbf{H} > \mathbf{0}$*, the selection of the gains* $\mathbf{K}, \mathbf{K}_1, \mathbf{K}_2, \hat{\mathbf{A}}_2, \rho$ *and* ρ_1 *satisfy* (4.18)-(4.23).

Proof. The closed-loop system stability is proved using the following Lyapunov function:

$$V(\boldsymbol{\xi}) = V_1(\tilde{\boldsymbol{\eta}}, \tilde{\boldsymbol{\nu}}) + V_2(\hat{\boldsymbol{\eta}}, \hat{\boldsymbol{\nu}}), \tag{4.26}$$

where

$$\boldsymbol{\xi} \triangleq [\tilde{\boldsymbol{\eta}}^T \ \tilde{\boldsymbol{\nu}}^T \ \hat{\boldsymbol{\eta}}^T \ \hat{\boldsymbol{\nu}}^T]^T \tag{4.27}$$

$$V_1 \triangleq (\frac{1}{2}\tilde{\boldsymbol{\eta}}^T\tilde{\boldsymbol{\eta}} + \frac{1}{2}\tilde{\boldsymbol{\nu}}^T\tilde{\boldsymbol{\nu}}) \tag{4.28}$$

$$V_2 \triangleq (\frac{1}{2}\hat{\boldsymbol{\eta}}^T\hat{\boldsymbol{\eta}} + \frac{1}{2}\hat{\boldsymbol{\nu}}^T\hat{\boldsymbol{\nu}}). \tag{4.29}$$

Using (4.13)-(4.16), the observer error dynamics are

$$\dot{\tilde{\boldsymbol{\eta}}} = \dot{\boldsymbol{\eta}} - \dot{\hat{\boldsymbol{\eta}}} = \mathbf{R}_3\tilde{\boldsymbol{\nu}} + \mathbf{K}\hat{\boldsymbol{\eta}} - \mathbf{K}_1\tilde{\boldsymbol{\eta}}, \tag{4.30}$$

$$\dot{\tilde{\boldsymbol{\nu}}} = \dot{\boldsymbol{\nu}} - \dot{\hat{\boldsymbol{\nu}}} = -\hat{\mathbf{A}}_1\tilde{\boldsymbol{\eta}} - \tilde{\mathbf{A}}_1(\tilde{\boldsymbol{\eta}} + \hat{\boldsymbol{\eta}}) - \mathbf{K}_2\hat{\boldsymbol{\eta}} - \hat{\mathbf{A}}_2\tilde{\boldsymbol{\nu}} - \tilde{\mathbf{A}}_2(\tilde{\boldsymbol{\nu}} + \hat{\boldsymbol{\nu}}) + \mathbf{d}. \tag{4.31}$$

4

From (4.26) and (4.30)-(4.31), the following can be achieved:

$$\begin{aligned}\dot{V}_1 &= -\tilde{\boldsymbol{\eta}}^T\mathbf{K}_1\tilde{\boldsymbol{\eta}} - \tilde{\boldsymbol{\nu}}^T(\hat{\mathbf{A}}_2 + \tilde{\mathbf{A}}_2)\tilde{\boldsymbol{\nu}} + \tilde{\boldsymbol{\eta}}^T\mathbf{K}\hat{\boldsymbol{\eta}} - \tilde{\boldsymbol{\nu}}^T(\tilde{\mathbf{A}}_1 - \mathbf{K}_2)\tilde{\boldsymbol{\eta}} - \tilde{\boldsymbol{\nu}}^T\tilde{\mathbf{A}}_2\hat{\boldsymbol{\nu}} - \tilde{\boldsymbol{\nu}}^T(\tilde{\mathbf{A}}_1 + \mathbf{K}_2)\hat{\boldsymbol{\eta}} + \tilde{\boldsymbol{\nu}}^T\mathbf{d} \\ &\leq -\tilde{\boldsymbol{\eta}}^T\mathbf{K}_1\tilde{\boldsymbol{\eta}} - \tilde{\boldsymbol{\nu}}^T\hat{\mathbf{A}}_2\tilde{\boldsymbol{\nu}} + \tilde{\boldsymbol{\eta}}^T\mathbf{K}\hat{\boldsymbol{\eta}} + \tilde{\boldsymbol{\nu}}^T\mathbf{d} - \tilde{\boldsymbol{\nu}}^T\tilde{\mathbf{A}}_2\hat{\boldsymbol{\nu}} - \tilde{\boldsymbol{\nu}}^T(\tilde{\mathbf{A}}_1 - \mathbf{K}_2)\tilde{\boldsymbol{\eta}} - \tilde{\boldsymbol{\nu}}^T(\tilde{\mathbf{A}}_1 + \mathbf{K}_2)\hat{\boldsymbol{\eta}},\end{aligned} \tag{4.32}$$

where we have used the fact that $\tilde{\mathbf{A}}_2$ is positive definite from Assumption 4.1. Further, using (4.15)-(4.17), the following can be deduced:

$$\begin{aligned}\dot{V}_2 &= \hat{\boldsymbol{\eta}}^T(-\mathbf{K}\hat{\boldsymbol{\eta}} + \mathbf{K}_1\tilde{\boldsymbol{\eta}} + \mathbf{R}_3\hat{\boldsymbol{\nu}}) + \hat{\boldsymbol{\nu}}^T(-(\rho + \rho_1)\hat{\boldsymbol{\nu}} - \mathbf{R}_3^T\hat{\boldsymbol{\eta}}) \\ &= -\hat{\boldsymbol{\eta}}^T\mathbf{K}\hat{\boldsymbol{\eta}} - (\rho + \rho_1)||\hat{\boldsymbol{\nu}}||^2 + \tilde{\boldsymbol{\eta}}^T\mathbf{K}_1\hat{\boldsymbol{\eta}}.\end{aligned} \tag{4.33}$$

Given any scalar $\beta > 0$ and a positive definite matrix $\mathbf{H}$, the following holds for any two non-zero vectors $\mathbf{z}$ and $\mathbf{z}_1$,

$$\pm 2\mathbf{z}^T\mathbf{z}_1 \leq \beta\mathbf{z}^T\mathbf{H}\mathbf{z} + (1/\beta)\mathbf{z}_1^T\mathbf{H}^{-1}\mathbf{z}_1. \tag{4.34}$$

Applying (4.34) to the last three terms of (4.32) and utilizing the definitions of maximum perturbations from Assumption 4.1, the following relations are obtained:

$$-\tilde{\boldsymbol{\nu}}^T(\tilde{\mathbf{A}}_1 - \mathbf{K}_2)\tilde{\boldsymbol{\eta}} \leq (\beta/2)\tilde{\boldsymbol{\nu}}^T\mathbf{H}\tilde{\boldsymbol{\nu}} + (1/2\beta)\tilde{\boldsymbol{\eta}}^T(\Delta\mathbf{A}_1 - \mathbf{K}_2)^T\mathbf{H}^{-1}(\Delta\mathbf{A}_1 - \mathbf{K}_2)\tilde{\boldsymbol{\eta}}, \tag{4.35}$$

$$-\tilde{\boldsymbol{\nu}}^T\tilde{\mathbf{A}}_2\hat{\boldsymbol{\nu}} \leq (\beta/2)\tilde{\boldsymbol{\nu}}^T\mathbf{H}\tilde{\boldsymbol{\nu}} + (1/2\beta)\hat{\boldsymbol{\nu}}^T\Delta\mathbf{A}_2^T\mathbf{H}^{-1}\Delta\mathbf{A}_2\hat{\boldsymbol{\nu}}. \tag{4.36}$$

$$-\tilde{\boldsymbol{\nu}}^T(\tilde{\mathbf{A}}_1 + \mathbf{K}_2)\hat{\boldsymbol{\eta}} \leq (\beta/2)\tilde{\boldsymbol{\nu}}^T\mathbf{H}\tilde{\boldsymbol{\nu}} + (1/2\beta)\hat{\boldsymbol{\eta}}^T(\Delta\mathbf{A}_1 + \mathbf{K}_2)^T\mathbf{H}^{-1}(\Delta\mathbf{A}_1 + \mathbf{K}_2)\hat{\boldsymbol{\eta}}. \tag{4.37}$$

Substituting (4.35)-(4.37) in (4.32), adding (4.32) and (4.33) yields:

$$\begin{aligned}\dot{V} \leq &-\tilde{\boldsymbol{\eta}}^T\{\mathbf{K}_1 - (1/2\beta)(\Delta\mathbf{A}_1 - \mathbf{K}_2)^T\mathbf{H}^{-1}(\Delta\mathbf{A}_1 - \mathbf{K}_2)\}\tilde{\boldsymbol{\eta}} - \tilde{\boldsymbol{\nu}}^T\{\hat{\mathbf{A}}_2 - (3\beta/2)\mathbf{H}\}\tilde{\boldsymbol{\nu}} \\ &- \hat{\boldsymbol{\eta}}^T\{\mathbf{K} - (1/2\beta)(\Delta\mathbf{A}_1 + \mathbf{K}_2)^T\mathbf{H}^{-1}(\Delta\mathbf{A}_1 + \mathbf{K}_2)\}\hat{\boldsymbol{\eta}} - \hat{\boldsymbol{\nu}}^T\{\rho\mathbf{I} - (1/2\beta)\Delta\mathbf{A}_2^T\mathbf{H}^{-1}\Delta\mathbf{A}_2\}\hat{\boldsymbol{\nu}} \\ &- \rho_1||\hat{\boldsymbol{\nu}}||^2 + \tilde{\boldsymbol{\eta}}^T(\mathbf{K} + \mathbf{K}_1)\hat{\boldsymbol{\eta}} + \tilde{\boldsymbol{\nu}}^T\Delta\mathbf{d}.\end{aligned} \tag{4.38}$$

From the definition of $\boldsymbol{\xi}$ we have $||\boldsymbol{\xi}|| \geq ||\hat{\boldsymbol{\nu}}||$ and $||\boldsymbol{\xi}|| \geq ||\tilde{\boldsymbol{\nu}}||$. Moreover, $\alpha\int_0^t ||(\mathbf{K}_1 + \mathbf{K})||||\hat{\boldsymbol{\eta}}(\psi))||||\tilde{\boldsymbol{\eta}}(\psi)||\mathrm{d}\psi \geq \alpha||(\mathbf{K}_1 + \mathbf{K})||||\hat{\boldsymbol{\eta}}(t))||||\tilde{\boldsymbol{\eta}}(t)|| \ \forall\, t \geq 0$ where $\alpha > 1$ by design. Hence,

using the design conditions (4.18)-(4.20) we define the following positive definite matrices:

$$\mathbf{Q}_1 \triangleq \{\mathbf{K}_1 - \frac{1}{2\beta}(\Delta\mathbf{A}_1 - \mathbf{K}_2)^T\mathbf{H}^{-1}(\Delta\mathbf{A}_1 - \mathbf{K}_2)\},$$
$$\mathbf{Q}_2 \triangleq \{\hat{\mathbf{A}}_2 - ((3\beta/2)\mathbf{H})\},$$
$$\mathbf{Q}_3 \triangleq \{\mathbf{K} - \frac{1}{2\beta}(\Delta\mathbf{A}_1 + \mathbf{K}_2)^T\mathbf{H}^{-1}(\Delta\mathbf{A}_1 + \mathbf{K}_2)\},$$
$$\mathbf{Q}_4 \triangleq \{\rho\mathbf{I} - (1/2\beta)\Delta\mathbf{A}_2^T\mathbf{H}^{-1}\Delta\mathbf{A}_2\}.$$

Defining $\varrho_{\mathrm{m}} \triangleq \min_{i=1,2,3,4}\{\lambda_{\min}(\mathbf{Q}_i)\}$, from (4.38) we have:

$$\begin{aligned}\dot{V} &\leq -\lambda_{\min}(\mathbf{Q}_1)||\tilde{\boldsymbol{\eta}}||^2 - \lambda_{\min}(\mathbf{Q}_2)||\tilde{\boldsymbol{\nu}}|| - \lambda_{\min}(\mathbf{Q}_3)||\hat{\boldsymbol{\eta}}||^2 - \lambda_{\min}(\mathbf{Q}_4)||\hat{\boldsymbol{\nu}}||^2 \\ &\quad + ||(\mathbf{K}+\mathbf{K}_1)||||\tilde{\boldsymbol{\eta}}||||\hat{\boldsymbol{\eta}}|| + ||\tilde{\boldsymbol{\nu}}||||\mathbf{d}|| - \rho_1||\hat{\boldsymbol{\nu}}||^2 \\ &\leq -\varrho_{\mathrm{m}}||\boldsymbol{\xi}||^2 + ||\Delta\mathbf{d}||||\boldsymbol{\xi}|| - ||(\mathbf{K}+\mathbf{K}_1)||||\tilde{\boldsymbol{\eta}}||||\hat{\boldsymbol{\eta}}||(\alpha||\hat{\boldsymbol{\nu}}||^2 - 1). \end{aligned} \tag{4.39}$$

Consider a scalar $\sigma \in \mathbb{R}_3^+$ such that $0 < \sigma < \varrho_{\mathrm{m}}$. The definition of V in (4.26) yields $V \leq ||\boldsymbol{\xi}||^2$. Hence,

$$\begin{aligned}\dot{V} &\leq -\varrho_{\mathrm{m}}||\boldsymbol{\xi}||^2 + ||\Delta\mathbf{d}||||\boldsymbol{\xi}|| - ||(\mathbf{K}+\mathbf{K}_1)||||\tilde{\boldsymbol{\eta}}||||\hat{\boldsymbol{\eta}}||(\alpha||\hat{\boldsymbol{\nu}}||^2 - 1) \\ &= -(\varrho_{\mathrm{m}} - \sigma)||\boldsymbol{\xi}||^2 - \sigma||\boldsymbol{\xi}||^2 + ||\Delta\mathbf{d}||||\boldsymbol{\xi}|| - ||(\mathbf{K}+\mathbf{K}_1)||||\tilde{\boldsymbol{\eta}}||||\hat{\boldsymbol{\eta}}||(\alpha||\hat{\boldsymbol{\nu}}||^2 - 1) \\ &\leq -\sigma V - ||\boldsymbol{\xi}||\left\{(\varrho_{\mathrm{m}} - \sigma)||\boldsymbol{\xi}|| - ||\Delta\mathbf{d}||\right\} - ||(\mathbf{K}+\mathbf{K}_1)||||\tilde{\boldsymbol{\eta}}||||\hat{\boldsymbol{\eta}}||(\alpha||\hat{\boldsymbol{\nu}}||^2 - 1). \end{aligned} \tag{4.40}$$

Thus, one has $\dot{V} \leq -\sigma V$ when

$$\begin{aligned}\min\{||\hat{\boldsymbol{\nu}}||, ||\boldsymbol{\xi}||\} &\geq \max\{\left(||\Delta\mathbf{d}||/(\varrho_{\mathrm{m}} - \sigma)\right), \sqrt{1/\alpha}\} \\ &\Rightarrow ||\hat{\boldsymbol{\nu}}|| \geq \max\{\left(||\Delta\mathbf{d}||/(\varrho_{\mathrm{m}} - \sigma)\right), \sqrt{1/\alpha}\}. \end{aligned} \tag{4.41}$$

This affirms the Uniformly Ultimately Bounded (UUB) condition [51] implying $\tilde{\boldsymbol{\eta}}, \tilde{\boldsymbol{\nu}}, \hat{\boldsymbol{\eta}}, \hat{\boldsymbol{\nu}} \in \mathscr{L}_\infty \Rightarrow \boldsymbol{\eta}, \boldsymbol{\nu} \in \mathscr{L}_\infty$. □

4.2.5. KEY PERFORMANCE INDICATORS

From (4.41), an ultimate bound on the position error $\boldsymbol{\eta}$ and an upper bound of control input $\boldsymbol{\tau}$ can be computed, which can be used to define key performance indicators (KPIs), which are the maximum control input and the maximum position error in this case; KPIs help designers to tune the controller according to the application requirements (cf. Remark 4.5).

Let $\iota \triangleq \max\{\left(||\Delta\mathbf{d}||/(\varrho_{\mathrm{m}} - \sigma)\right), \sqrt{1/\alpha}\}$. From 4.26 we have $V \geq (1/2)||\hat{\boldsymbol{\nu}}||^2 \Rightarrow ||\hat{\boldsymbol{\nu}}|| \leq \sqrt{2V}$. Thus, from (4.41), we have $\dot{V} \leq -\sigma V$ when

$$\iota \leq ||\hat{\boldsymbol{\nu}}|| \leq \sqrt{2V} \Rightarrow V \geq \iota^2/2. \tag{4.42}$$

Therefore, one can deduce the upper bound of V as

$$V \leq \max\{V(0),\ \iota^2/2\} \triangleq \mathscr{B}. \tag{4.43}$$

Utilizing the relations $||\hat{\boldsymbol{\eta}}|| \leq \sqrt{2V}$, $||\tilde{\boldsymbol{\eta}}|| \leq \sqrt{2V}$ and $||\boldsymbol{\eta}|| = ||\tilde{\boldsymbol{\eta}}|| + ||\hat{\boldsymbol{\eta}}||$, the ultimate bound b on the position error $\boldsymbol{\eta}$ can be computed as follows:

$$b \in [0,\ 2\iota]. \tag{4.44}$$

Similarly, an upper bound on $\boldsymbol{\tau}$ can be derived from (4.17) as

$$\begin{aligned} ||\boldsymbol{\tau}|| &= ||\mathbf{M}\{\hat{\mathbf{A}}_1\hat{\boldsymbol{\eta}} + \hat{\mathbf{A}}_2\hat{\boldsymbol{\nu}} - \mathbf{K}_2\tilde{\boldsymbol{\eta}} - \mathbf{R}_3^T\hat{\boldsymbol{\eta}} - (\rho+\rho_1)\hat{\boldsymbol{\nu}}\}|| \\ &\leq \sqrt{2\mathscr{B}}||\mathbf{M}||\left\{||\hat{\mathbf{A}}_1 - \mathbf{R}_3^T|| + ||\hat{\mathbf{A}}_2 - (\rho+\rho_1)|| + ||\mathbf{K}_2||)\right\}. \end{aligned} \tag{4.45}$$

Remark 4.5 (Design guidelines)**.** *It can be noticed from* (4.41) *and* (4.43) *that high values of* $\mathbf{K}, \mathbf{K}_1, \rho$ *and* α *(determined from* (4.18)-(4.21)*) help to reduce* ι *and improve control performance. On the other hand, the upper bound* (4.45) *reveals that higher values of the above mentioned gains demands higher control input. Thus, a designer has to make a trade-off between the positioning performance (i.e. maximum position error) and control effort (i.e. maximum control input).*

Remark 4.6 (Innovative aspect of the proposed design)**.** *The notable feature of the stability result for the proposed DP scheme* (4.15)-(4.17) *is its composite nature: the design jointly provides robustness against model uncertainties and filtering against high-frequency state measurements. In state-of-the-art DP systems, no composite stability was proposed: either robustness is achieved neglecting high-frequency state measurement noises (cf. [12, 32, 41]), or state filtering is implemented while neglecting model uncertainties (cf. [21, 22, 46, 91, 102, 110]).*

4.3. OBSERVER-BASED ADAPTIVE SWITCHING CONTROL

In the previous section, a robust controller is designed for the vessel in Mode 1. However, during offshore heavy lift construction, the vessel-load system has different dynamics in Mode 1 and Mode 2, makes it difficult for one controller to handle a complete offshore heavy lift operation. In this section, a switching DP controller is designed to deal with different modes.

The structural changes summarized in (4.1)-(4.2) and Table 4.1 can be compactly captured by a switched dynamical framework

$$\dot{\boldsymbol{\eta}} = \mathbf{R}_3(\psi)\boldsymbol{\nu}, \tag{4.46}$$

$$\begin{aligned} \mathbf{M}_\sigma\dot{\boldsymbol{\nu}} &= -\mathbf{D}\boldsymbol{\nu} - \mathbf{F}_\sigma\boldsymbol{\eta} + \boldsymbol{\tau}_\sigma + \bar{\mathbf{d}} + \boldsymbol{\tau}_{l\sigma} \\ \Rightarrow \dot{\boldsymbol{\nu}} &= -\mathbf{A}_{1\sigma}\boldsymbol{\eta} - \mathbf{A}_{2\sigma}\boldsymbol{\nu} + \mathbf{M}_\sigma^{-1}\boldsymbol{\tau}_\sigma + \mathbf{d}_\sigma, \end{aligned} \tag{4.47}$$

where the signal $\sigma(\cdot)$ in (4.47) is a piece-wise constant *switching signal*, taking values in $\Omega = \{0,1,2\}$, with $\mathbf{F}_1 = \mathbf{F}_3 = \mathbf{0}$, $\boldsymbol{\tau}_{l1} = \boldsymbol{\tau}_{l2} = \mathbf{0}$, and

$$\mathbf{A}_{1\sigma} \triangleq \mathbf{M}^{-1}\mathbf{F}_\sigma, \tag{4.48}$$

$$\mathbf{A}_{2\sigma} \triangleq \mathbf{M}^{-1}\mathbf{D}, \tag{4.49}$$

$$\mathbf{d}_\sigma \triangleq \mathbf{M}^{-1}(\bar{\mathbf{d}} + \boldsymbol{\tau}_{l\sigma}). \tag{4.50}$$

In order to describe the duration of the different phases, the following class of switching signals is considered:

Definition 4.2. *(Average Dwell Time (ADT) [45]): For a switching signal $\sigma(\cdot)$ and each $t_2 \geq t_1 \geq 0$, let $N_\sigma(t_1, t_2)$ denote the number of discontinuities in the interval $[t_1, t_2)$. Then $\sigma(\cdot)$ has an average dwell time ϑ if for a given scalar $N_0 > 0$*

$$N_\sigma(t_1, t_2) \leq N_0 + (t_2 - t_1)/\vartheta, \quad \forall\, t_2 \geq t_1 \geq 0, \tag{4.51}$$

where N_0 is termed as chatter bound.

Remark 4.7 (The rationale for ADT)**.** *The average dwell time concept is well known in switching control literature [45, 80, 81, 111]. In offshore DP setting, this concept is useful to define the average duration of the different phases, which might depend on application requirements, e.g. Phase 0 ($\sigma = 0$)= 10 min, Phase 1 ($\sigma = 1$) = 20 min, Phase 2 ($\sigma = 2$) = 5 min [4, 55].*

4.3.1. UNCERTAINTY DESCRIPTION

The external disturbance is upper bounded as $||\mathbf{d}_\sigma(t)|| \leq ||\Delta\mathbf{d}_\sigma|| \;\forall\, t$ where $||\Delta\mathbf{d}_\sigma||$ is available for control design. For each phase, the mass matrix $\mathbf{M}$ is assumed to be known for control design, under the standard assumption that added mass terms are negligible during DP operation[1]. However, $\mathbf{F}_\sigma$ and $\mathbf{D}$ cannot be assumed to be known, as in practice they might even be time-varying: this leads to the positive definite matrices $\mathbf{A}_{1\sigma}$ and $\mathbf{A}_{2\sigma}$ [31] being time-varying and uncertain. The following assumption highlights the nature of uncertainties considered in this work.

Assumption 4.2 (Uncertainty for all Phases)**.** *Let $\mathbf{A}_{i\sigma}$ be decomposable into two positive definite matrices $\hat{\mathbf{A}}_{i\sigma}$ (known nominal part) and $\tilde{\mathbf{A}}_{i\sigma}$ (unknown perturbation) such that $\mathbf{A}_{i\sigma}(t) = \hat{\mathbf{A}}_{i\sigma} + \tilde{\mathbf{A}}_{i\sigma}(t)$. Let $\Delta\mathbf{A}_{i\sigma}$ be the maximum possible perturbation ranges such that $||\tilde{\mathbf{A}}_{i\sigma}(t)|| \leq ||\Delta\mathbf{A}_{i\sigma}|| \;\forall\, t$. The knowledge of $\hat{\mathbf{A}}_{i\sigma}$ and $\Delta\mathbf{A}_{i\sigma}$ is available for control design.*

4.3.2. CONTROLLER DESIGN

An observer-based switched robust controller is designed as:

$$\dot{\hat{\boldsymbol{\eta}}} = -\mathbf{K}_\sigma\hat{\boldsymbol{\eta}} + \mathbf{K}_{1\sigma}\tilde{\boldsymbol{\eta}} + \mathbf{R}_3\hat{\boldsymbol{\nu}}, \tag{4.52}$$

$$\dot{\hat{\boldsymbol{\nu}}} = -\hat{\mathbf{A}}_{1\sigma}\hat{\boldsymbol{\eta}} - \hat{\mathbf{A}}_{2\sigma}\hat{\boldsymbol{\nu}} + \mathbf{M}_\sigma^{-1}\boldsymbol{\tau}_\sigma + \mathbf{K}_{2\sigma}\hat{\boldsymbol{\eta}}, \tag{4.53}$$

$$\boldsymbol{\tau}_\sigma = \mathbf{M}_\sigma\{(\hat{\mathbf{A}}_{1\sigma} - \mathbf{K}_{2\sigma} - \mathbf{P}_{4\sigma}^{-1}\mathbf{R}_3^T\mathbf{P}_{3\sigma})\hat{\boldsymbol{\eta}} + (\hat{\mathbf{A}}_{2\sigma} - (\rho_\sigma + \rho_{1\sigma}))\hat{\boldsymbol{\nu}}\}, \tag{4.54}$$

where $\hat{\boldsymbol{\eta}}$ and $\hat{\boldsymbol{\nu}}$ are the estimations of $\boldsymbol{\eta}$ and $\boldsymbol{\nu}$ respectively, and $\tilde{\boldsymbol{\eta}} \triangleq \boldsymbol{\eta} - \hat{\boldsymbol{\eta}}$, $\tilde{\boldsymbol{\nu}} \triangleq \boldsymbol{\nu} - \hat{\boldsymbol{\nu}}$ are the corresponding estimation errors. Note that the observer dynamics (4.52)-(4.53) are constructed based on (4.46)-(4.47) with available system dynamics knowledge (cf. Assumption 4.2).

The observer and control gains $\mathbf{H}_\sigma, \mathbf{K}_\sigma, \mathbf{K}_{1\sigma}, \mathbf{K}_{2\sigma}, \rho_{1\sigma}, \rho_\sigma$ and $\mathbf{P}_{i\sigma}$ in (4.52)-(4.54) are

[1] As offshore heavy-lift vessels are large in size including the load, variation in mass and inertia parameters are usually negligible [31].

used for system stability and robustness against uncertainties, and are designed as

$$\lambda_{\min}(\mathbf{P}_{1\sigma}\mathbf{K}_{1\sigma}) > ||(1/2\beta)(\Delta\mathbf{A}_{1\sigma}-\mathbf{K}_{2\sigma})^T\mathbf{P}_{2\sigma}\mathbf{H}_\sigma^{-1}\mathbf{P}_{2\sigma}\times(\Delta\mathbf{A}_{1\sigma}-\mathbf{K}_{2\sigma})||, \tag{4.55}$$

$$\lambda_{\min}(\mathbf{P}_{3\sigma}\mathbf{K}_{\sigma}) > ||(1/2\beta)(\Delta\mathbf{A}_{1\sigma}+\mathbf{K}_{2\sigma})^T\mathbf{P}_{2\sigma}\mathbf{H}_\sigma^{-1}\mathbf{P}_{2\sigma}\times(\Delta\mathbf{A}_{1\sigma}+\mathbf{K}_{2\sigma})||, \tag{4.56}$$

$$\lambda_{\min}(\mathbf{P}_{4\sigma})\rho_\sigma > ||(1/2\beta)\Delta\mathbf{A}_{2\sigma}^T\mathbf{P}_{2\sigma}\mathbf{H}_\sigma^{-1}\mathbf{P}_{2\sigma}\Delta\mathbf{A}_{2\sigma}|| + ||\Delta\mathbf{d}_\sigma||, \tag{4.57}$$

$$\rho_{1\sigma} = \alpha\int_0^t ||(\mathbf{K}_{1\sigma}+\mathbf{K}_\sigma)||||\hat{\boldsymbol{\eta}}(\varpi)||||\tilde{\boldsymbol{\eta}}(\varpi)||\mathrm{d}\varpi, \tag{4.58}$$

$$\mathbf{K}_{2\sigma}(t) = -\hat{\mathbf{A}}_{1\sigma} + \mathbf{R}_{\mathrm{b}}^{\mathrm{n}T}(t), \tag{4.59}$$

$$\lambda_{\min}(\mathbf{P}_{2\sigma}\hat{\mathbf{A}}_{2\sigma}) > ||(3\beta/2)\mathbf{H}_\sigma||, \tag{4.60}$$

where $\alpha > 1$ and $\beta > 0$ are design scalars.

Let us define

$$\mathbf{P}_\sigma \triangleq diag\{\mathbf{P}_{1\sigma},\mathbf{P}_{2\sigma},\mathbf{P}_{3\sigma},\mathbf{P}_{4\sigma}\}, \tag{4.61}$$

$$\varrho_{\mathrm{m}} \triangleq \max_{\sigma\in\Omega}\lambda_{\max}(\mathbf{P}_\sigma),\ \varrho_{\mathrm{m}} \triangleq \min_{\sigma\in\Omega}\lambda_{\min}(\mathbf{P}_\sigma), \tag{4.62}$$

$$\kappa \triangleq 2\min_{\sigma\in\Omega}\min_{i=1,\cdots,4}(\lambda_{\min}(\mathbf{Q}_{i\sigma}))/\varrho_{\mathrm{m}}, \tag{4.63}$$

where $\mathbf{Q}_{i\sigma}$ are positive definite matrices defined as

$$\mathbf{Q}_{1\sigma} \triangleq \{\mathbf{P}_{1\sigma}\mathbf{K}_{1\sigma} - (1/2\beta)(\Delta\mathbf{A}_{1\sigma}-\mathbf{K}_{2\sigma})^T\mathbf{P}_{2\sigma}\mathbf{H}_\sigma^{-1}\mathbf{P}_{2\sigma}\times(\Delta\mathbf{A}_{1\sigma}-\mathbf{K}_{2\sigma})\},$$
$$\mathbf{Q}_{2\sigma} \triangleq \{\mathbf{P}_{2\sigma}\hat{\mathbf{A}}_{2\sigma} - ((3\beta/2)\mathbf{H}_\sigma)\},$$
$$\mathbf{Q}_{3\sigma} \triangleq \{\mathbf{P}_{3\sigma}\mathbf{K}_\sigma - (1/2\beta)(\Delta\mathbf{A}_{1\sigma}+\mathbf{K}_{2\sigma})^T\mathbf{P}_{2\sigma}\mathbf{H}_\sigma^{-1}\mathbf{P}_{2\sigma}\times(\Delta\mathbf{A}_{1\sigma}+\mathbf{K}_{2\sigma})\},$$
$$\mathbf{Q}_{4\sigma} \triangleq \{\rho_\sigma\mathbf{P}_{4\sigma} - (1/2\beta)\Delta\mathbf{A}_{2\sigma}^T\mathbf{P}_{2\sigma}\mathbf{H}_\sigma^{-1}\mathbf{P}_{2\sigma}\Delta\mathbf{A}_{2\sigma}\}.$$

Following Definition 1, let us consider the switching signal $\sigma(\cdot)$ with an average dwell time ϑ satisfying

$$\vartheta > \vartheta^* = \ln\mu/\zeta, \tag{4.64}$$

where $\mu \triangleq \varrho_{\mathrm{m}}/\varrho_{\mathrm{m}}$ and $0 < \zeta < \kappa$.

Remark 4.8 (Continuity of the states)**.** *During switching the control/observer gains switch, whereas the states $\boldsymbol{\eta},\boldsymbol{\nu}$ in* (4.46)-(4.47) *and their observed values $\hat{\boldsymbol{\eta}},\hat{\boldsymbol{\nu}}$ in* (4.52)-(4.53) *are common to all subsystems, i.e. they are continuous despite switching. Therefore, issues of chattering as in state-dependent switching (sliding mode) will be absent in ADT time-driven switching [45].*

Remark 4.9 (Selection of gains)**.** *According to Assumption 4.2, $\hat{\mathbf{A}}_{2\sigma}$ is the nominal knowledge of $\mathbf{A}_{2\sigma}$. Therefore, (4.60) provides a selection criterion for $\beta,\mathbf{H}_\sigma$ and $\mathbf{P}_{2\sigma}$, which in turn guide the selection of $\mathbf{P}_{1\sigma},\mathbf{P}_{3\sigma},\mathbf{P}_{4\sigma},\mathbf{K}_{1\sigma},\mathbf{K}_\sigma,\rho_\sigma$ and $\rho_{1\sigma}$ via (4.55), (4.56), (4.57) and (4.58).*

Remark 4.10 (Co-design of switching and control law)**.** *In switching control literature it is well known that stability cannot be achieved for arbitrarily switching signals [54, 81,*

111]. This implies that one should not only design a stabilizing control law, but also a stabilizing family of switching laws. In the proposed DP setting, the switching controller is (4.52)-(4.54)*, whereas the switching signal is given by* (4.64) *in the ADT framework of Definition 1. The parameter in* (4.64) *should be properly tuned so that ϑ^* represents the typical duration of the different construction phases (cf. Remark 4.9).*

4.3.3. STABILITY ANALYSIS

The closed-loop system stability is analyzed using the following Lyapunov function:

$$V(\boldsymbol{\xi}) = V_1(\tilde{\boldsymbol{\eta}}, \tilde{\boldsymbol{\nu}}) + V_2(\hat{\boldsymbol{\eta}}, \hat{\boldsymbol{\nu}}) = \frac{1}{2}\boldsymbol{\xi}^T \mathbf{P}_\sigma \boldsymbol{\xi}, \tag{4.65}$$

where $\boldsymbol{\xi} \triangleq [\tilde{\boldsymbol{\eta}}^T\ \tilde{\boldsymbol{\nu}}^T\ \hat{\boldsymbol{\eta}}^T\ \hat{\boldsymbol{\nu}}^T]^T$ and

$$V_1 \triangleq \frac{1}{2}(\tilde{\boldsymbol{\eta}}^T \mathbf{P}_{1\sigma} \tilde{\boldsymbol{\eta}} + \tilde{\boldsymbol{\nu}}^T \mathbf{P}_{2\sigma} \tilde{\boldsymbol{\nu}}),$$
$$V_2 \triangleq \frac{1}{2}(\hat{\boldsymbol{\eta}}^T \mathbf{P}_{3\sigma} \hat{\boldsymbol{\eta}} + \hat{\boldsymbol{\nu}}^T \mathbf{P}_{4\sigma} \hat{\boldsymbol{\nu}}).$$

The following theorem states the closed-loop system stability:

Theorem 4.2. *Under Assumption 4.2, the switched system* (4.46)-(4.47) *employing the switched control input law* (4.52)-(4.54) *and satisfying the gain selection criteria* (4.55)-(4.60) *is Globally Uniformly Ultimately Bounded (GUUB) for any ADT switching signal satisfying (4.64). This implies*

$$V(t) \leq \max\{bV(t_0), b\mu\mathscr{B}\}, \quad \forall\, t \geq t_0. \tag{4.66}$$
$$\text{where } b \triangleq \exp\left(N_0 \ln \mu\right),\ \mathscr{B} \triangleq \max_\sigma \left(\frac{2||\Delta \mathbf{d}_\sigma||^2}{\varrho_{\mathrm{m}}(\kappa-\zeta)^2}, \frac{\varrho_{\mathrm{m}}}{2\alpha}\right).$$

Proof. Using (4.46), (4.47), (4.52) and (4.53), the observer error dynamics can be formulated as

$$\dot{\tilde{\boldsymbol{\eta}}} = \dot{\boldsymbol{\eta}} - \dot{\hat{\boldsymbol{\eta}}} = \mathbf{R}_3 \tilde{\boldsymbol{\nu}} + \mathbf{K}_\sigma \hat{\boldsymbol{\eta}} - \mathbf{K}_{1\sigma} \tilde{\boldsymbol{\eta}}, \tag{4.67}$$
$$\dot{\tilde{\boldsymbol{\nu}}} = \dot{\boldsymbol{\nu}} - \dot{\hat{\boldsymbol{\nu}}} = -\hat{\mathbf{A}}_{1\sigma} \tilde{\boldsymbol{\eta}} - \tilde{\mathbf{A}}_{1\sigma}(\tilde{\boldsymbol{\eta}} + \hat{\boldsymbol{\eta}}) - \mathbf{K}_{2\sigma} \hat{\boldsymbol{\eta}} - \hat{\mathbf{A}}_{2\sigma} \tilde{\boldsymbol{\nu}} - \tilde{\mathbf{A}}_{2\sigma}(\tilde{\boldsymbol{\nu}} + \hat{\boldsymbol{\nu}}) + \mathbf{d}_\sigma. \tag{4.68}$$

The Lyapunov function $V(\cdot)$ is continuous in between switching instants but, due to switching to different $\mathbf{P}_\sigma$, it might be discontinuous at switching instants. The behaviour of the Lyapunov function is studied at $t_{l+1},\ l \in \mathbb{N}^+$. Let the active subsystem be $\sigma(t_{l+1}^-)$ when $t \in [t_l\ \ t_{l+1})$ and $\sigma(t_{l+1})$ when $t \in [t_{l+1}\ \ t_{l+2})$. We have before and after switching

$$V(t_{l+1}^-) = (1/2)\boldsymbol{\xi}^T(t_{l+1}^-)\mathbf{P}_{\sigma(t_{l+1}^-)}\boldsymbol{\xi}(t_{l+1}^-)$$
$$V(t_{l+1}) = (1/2)\boldsymbol{\xi}^T(t_{l+1})\mathbf{P}_{\sigma(t_{l+1})}\boldsymbol{\xi}(t_{l+1}),$$

respectively. Thanks to the continuity of $\hat{\boldsymbol{\eta}}, \hat{\boldsymbol{\nu}}$ in (4.52)-(4.53) and of $\tilde{\boldsymbol{\eta}}, \tilde{\boldsymbol{\nu}}$ in (4.67)-(4.68) (cf. Remark 3) we have $\hat{\boldsymbol{\eta}}(t_{l+1}^-) = \hat{\boldsymbol{\eta}}(t_{l+1})$, $\hat{\boldsymbol{\nu}}(t_{l+1}^-) = \hat{\boldsymbol{\nu}}(t_{l+1})$, $\tilde{\boldsymbol{\eta}}(t_{l+1}^-) = \tilde{\boldsymbol{\eta}}(t_{l+1})$ and $\tilde{\boldsymbol{\nu}}(t_{l+1}^-) =$

$\tilde{\boldsymbol{\nu}}(t_{l+1})$. This leads to $\boldsymbol{\xi}(t_{l+1}^-) = \boldsymbol{\xi}(t_{l+1})$. Since $\boldsymbol{\xi}^T(t)\mathbf{P}_{\sigma(t)}\boldsymbol{\xi}(t) \leq \varrho_{\mathrm{m}}\boldsymbol{\xi}^T(t)\boldsymbol{\xi}(t)$ and $\boldsymbol{\xi}^T(t)\mathbf{P}_{\sigma(t)}\boldsymbol{\xi}(t) \geq \varrho_{\mathrm{m}}\boldsymbol{\xi}^T(t)\boldsymbol{\xi}(t)$, it yields

$$\begin{aligned} V(t_{l+1}) - V(t_{l+1}^-) &= \frac{1}{2}\boldsymbol{\xi}^T(t_{l+1})(\mathbf{P}_{\sigma(t_{l+1})} - \mathbf{P}_{\sigma(t_{l+1}^-)})\boldsymbol{\xi}(t_{l+1}) \\ &\leq \frac{\varrho_{\mathrm{M}} - \varrho_{\mathrm{m}}}{2\varrho_{\mathrm{m}}}\boldsymbol{\xi}^T(t_{l+1})\mathbf{P}_{\sigma(t_{l+1}^-)}\boldsymbol{\xi}(t_{l+1}) \leq \frac{\varrho_{\mathrm{M}} - \varrho_{\mathrm{m}}}{\varrho_{\mathrm{m}}}V(t_{l+1}^-) \\ &\Rightarrow V(t_{l+1}) \leq \mu V(t_{l+1}^-), \end{aligned} \tag{4.69}$$

with $\mu = \varrho_{\mathrm{M}}/\varrho_{\mathrm{m}} \geq 1$. At this point, the behaviour of $V(\cdot)$ between two consecutive switching instants, i.e., when $t \in [t_l \;\; t_{l+1})$ can be studied.

Utilizing (4.67)-(4.68), the following can be achieved

$$\begin{aligned} \dot{V}_1 =& \tilde{\boldsymbol{\eta}}^T\mathbf{P}_{1\sigma}(-\mathbf{K}_{1\sigma}\tilde{\boldsymbol{\eta}} + \mathbf{K}_\sigma\hat{\boldsymbol{\eta}} + \mathbf{R}_3\tilde{\boldsymbol{\nu}}) - \tilde{\boldsymbol{\nu}}^T\mathbf{P}_{2\sigma}(\hat{\mathbf{A}}_{2\sigma} + \tilde{\mathbf{A}}_{2\sigma})\tilde{\boldsymbol{\nu}} - \tilde{\boldsymbol{\nu}}^T\mathbf{P}_{2\sigma}(\hat{\mathbf{A}}_{1\sigma} + \tilde{\mathbf{A}}_{1\sigma})\tilde{\boldsymbol{\eta}} \\ &- \tilde{\boldsymbol{\nu}}^T\mathbf{P}_{2\sigma}(\tilde{\mathbf{A}}_{1\sigma} + \mathbf{K}_{2\sigma})\hat{\boldsymbol{\eta}} - \tilde{\boldsymbol{\nu}}^T\mathbf{P}_{2\sigma}\tilde{\mathbf{A}}_{2\sigma}\hat{\boldsymbol{\nu}} + \tilde{\boldsymbol{\nu}}^T\mathbf{P}_{2\sigma}\mathbf{d}_\sigma \\ \leq& -\tilde{\boldsymbol{\eta}}^T\mathbf{P}_{1\sigma}\mathbf{K}_{1\sigma}\tilde{\boldsymbol{\eta}} - \tilde{\boldsymbol{\nu}}^T\mathbf{P}_{2\sigma}\hat{\mathbf{A}}_{2\sigma}\tilde{\boldsymbol{\nu}} + \tilde{\boldsymbol{\eta}}^T\mathbf{P}_{1\sigma}\mathbf{K}_\sigma\hat{\boldsymbol{\eta}} + \tilde{\boldsymbol{\nu}}^T\mathbf{P}_{2\sigma}\mathbf{d}_\sigma - \tilde{\boldsymbol{\nu}}^T\mathbf{P}_{2\sigma}(\tilde{\mathbf{A}}_{1\sigma} + \mathbf{K}_{2\sigma})\hat{\boldsymbol{\eta}} \\ &- \tilde{\boldsymbol{\nu}}^T\mathbf{P}_{2\sigma}(\tilde{\mathbf{A}}_{1\sigma} - \mathbf{K}_{2\sigma})\tilde{\boldsymbol{\eta}} - \tilde{\boldsymbol{\nu}}^T\mathbf{P}_{2\sigma}\tilde{\mathbf{A}}_{2\sigma}\hat{\boldsymbol{\nu}}. \end{aligned} \tag{4.70}$$

Further, using (4.52)-(4.54), the following can be deduced

$$\begin{aligned} \dot{V}_2 =& \hat{\boldsymbol{\eta}}^T\mathbf{P}_{3\sigma}(-\mathbf{K}_\sigma\hat{\boldsymbol{\eta}} + \mathbf{K}_{1\sigma}\tilde{\boldsymbol{\eta}} + \mathbf{R}_3\hat{\boldsymbol{\nu}}) + \hat{\boldsymbol{\nu}}^T\mathbf{P}_{4\sigma}(-(\rho_\sigma + \rho_{1\sigma})\hat{\boldsymbol{\nu}} - \mathbf{P}_{4\sigma}^{-1}\mathbf{R}_3^T\mathbf{P}_{3\sigma}\hat{\boldsymbol{\eta}}) \\ =& -\hat{\boldsymbol{\eta}}^T\mathbf{P}_{3\sigma}\mathbf{K}_\sigma\hat{\boldsymbol{\eta}} - (\rho_\sigma + \rho_{1\sigma})\hat{\boldsymbol{\nu}}^T\mathbf{P}_{4\sigma}\hat{\boldsymbol{\nu}} + \tilde{\boldsymbol{\eta}}^T\mathbf{K}_{1\sigma}\mathbf{P}_{3\sigma}\hat{\boldsymbol{\eta}}. \end{aligned}$$

Applying (4.34) to the last three terms of (4.70) and utilizing the maximum perturbations from Assumption 1 results in

$$\begin{aligned} \dot{V} \leq& -\tilde{\boldsymbol{\eta}}^T\{\mathbf{P}_{1\sigma}\mathbf{K}_{1\sigma} - (1/2\beta)(\Delta\mathbf{A}_{1\sigma} - \mathbf{K}_{2\sigma})^T\mathbf{P}_{2\sigma}\mathbf{H}_\sigma^{-1}\mathbf{P}_{2\sigma} \times (\Delta\mathbf{A}_{1\sigma} - \mathbf{K}_{2\sigma})\}\tilde{\boldsymbol{\eta}} \\ &- \tilde{\boldsymbol{\nu}}^T\{\mathbf{P}_{2\sigma}\hat{\mathbf{A}}_{2\sigma} - (3\beta/2)\mathbf{H}_\sigma\}\tilde{\boldsymbol{\nu}} \\ &- \hat{\boldsymbol{\eta}}^T\{\mathbf{P}_{3\sigma}\mathbf{K}_\sigma - (1/2\beta)(\Delta\mathbf{A}_{1\sigma} + \mathbf{K}_{2\sigma})^T\mathbf{P}_{2\sigma}\mathbf{H}_\sigma^{-1}\mathbf{P}_{2\sigma} \times (\Delta\mathbf{A}_{1\sigma} + \mathbf{K}_{2\sigma})\}\hat{\boldsymbol{\eta}} \\ &- \hat{\boldsymbol{\nu}}^T\{\rho_\sigma\mathbf{P}_{4\sigma} - (1/2\beta)\Delta\mathbf{A}_{2\sigma}^T\mathbf{P}_{2\sigma}\mathbf{H}_\sigma^{-1}\mathbf{P}_{2\sigma}\Delta\mathbf{A}_{2\sigma}\}\hat{\boldsymbol{\nu}} \\ &- \rho_{1\sigma}\lambda_{\min}(\mathbf{P}_{4\sigma})||\hat{\boldsymbol{\nu}}||^2 + \tilde{\boldsymbol{\eta}}^T(\mathbf{K}_\sigma + \mathbf{K}_{1\sigma})\hat{\boldsymbol{\eta}} + \tilde{\boldsymbol{\nu}}^T\Delta\mathbf{d}_\sigma. \end{aligned} \tag{4.71}$$

Observe that $||\boldsymbol{\xi}|| \geq ||\hat{\boldsymbol{\nu}}||$ and $||\boldsymbol{\xi}|| \geq ||\tilde{\boldsymbol{\nu}}||$. Moreover,

$$\alpha\int_0^t ||(\mathbf{K}_{1\sigma} + \mathbf{K}_\sigma)||||\hat{\boldsymbol{\eta}}(\varpi))||||\tilde{\boldsymbol{\eta}}(\varpi)||\mathrm{d}\varpi \geq \alpha||(\mathbf{K}_{1\sigma} + \mathbf{K}_\sigma)||||\hat{\boldsymbol{\eta}}(t))||||\tilde{\boldsymbol{\eta}}(t)|| \;\forall\, t \geq t_0$$

where $\alpha > 1$ by design. Using the design conditions (4.55)-(4.57), the fact $\mathbf{P}_{4\sigma} > \mathbf{0}$ and the definitions of $\mathbf{Q}_{i\sigma}$ in (4.63), we have

$$\begin{aligned} \dot{V} \leq& -\lambda_{\min}(\mathbf{Q}_{1\sigma})||\tilde{\boldsymbol{\eta}}||^2 - \lambda_{\min}(\mathbf{Q}_{2\sigma})||\tilde{\boldsymbol{\nu}}|| - \lambda_{\min}(\mathbf{Q}_{3\sigma})||\hat{\boldsymbol{\eta}}||^2 \\ &- \lambda_{\min}(\mathbf{Q}_{4\sigma})||\hat{\boldsymbol{\nu}}||^2 + ||(\mathbf{K}_\sigma + \mathbf{K}_{1\sigma})||||\tilde{\boldsymbol{\eta}}||||\hat{\boldsymbol{\eta}}|| + ||\tilde{\boldsymbol{\nu}}||||\mathbf{d}_\sigma|| - \rho_{1\sigma}||\hat{\boldsymbol{\nu}}||^2 \\ \leq& -\min_i(\lambda_{\min}(\mathbf{Q}_{i\sigma}))||\boldsymbol{\xi}||^2 + ||\Delta\mathbf{d}_\sigma||||\boldsymbol{\xi}|| - ||(\mathbf{K}_\sigma + \mathbf{K}_{1\sigma})||||\tilde{\boldsymbol{\eta}}||||\hat{\boldsymbol{\eta}}||(\alpha||\hat{\boldsymbol{\nu}}||^2 - 1). \end{aligned} \tag{4.72}$$

The form of V in (4.65) gives $\varrho_{\mathrm{m}}/2||\boldsymbol{\xi}||^2 \leq V \leq \varrho_{\mathrm{m}}/2||\boldsymbol{\xi}||^2$. Then, for a scalar ζ such that $0 < \zeta < \kappa$, (4.72) becomes

$$\dot{V} \leq -\zeta V - (\kappa - \zeta)V + ||\Delta \mathbf{d}_\sigma||\sqrt{2V/\varrho_{\mathrm{m}}} - ||(\mathbf{K}_\sigma + \mathbf{K}_{1\sigma})||||\tilde{\boldsymbol{\eta}}||||\hat{\boldsymbol{\eta}}||(\alpha||\hat{\boldsymbol{\nu}}||^2 - 1). \tag{4.73}$$

Further, utilizing the fact $||\boldsymbol{\xi}|| \geq ||\hat{\boldsymbol{\nu}}||$ one has $V \geq (\varrho_{\mathrm{m}}/2)||\boldsymbol{\xi}||^2 \geq (\varrho_{\mathrm{m}}/2)||\hat{\boldsymbol{\nu}}||^2$. Then, noting $\mathscr{B}$ from (4.66), one can verify that $\dot{V} \leq -\zeta V$ is guaranteed when $V \geq \mathscr{B}$.

In light of this, further analysis is needed to observe the behaviour of $V(t)$ between the two consecutive switching instants, i.e., $t \in [t_l \;\; t_{l+1})$, for two possible cases:

(i) when $V(t) \geq \mathscr{B}$, we have $\dot{V}(t) \leq -\zeta V(t)$ implying exponential decrease of the Lyapunov function;

(ii) when $V(t) < \mathscr{B}$, no exponential decrease can be derived.

The behaviour of $V(t)$ is discussed individually for the two cases.

Case (i): There exists a time, T_1, when $V(t)$ enters into the bound $\mathscr{B}$ and $N_\sigma(t)$ denotes the number of all switching intervals for $t \in [t_0 \;\; t_0 + T_1)$, where t_0 denotes initial time. Accordingly, for $t \in [t_0 \;\; t_0 + T_1)$, using (4.69) and $N_\sigma(t_0, t)$ from Definition 1 we have

$$\begin{aligned}
V(t) &\leq \mu \exp\left(-\zeta(t - t_{N_\sigma(t)-1})\right) V(t^-_{N_\sigma(t)-1}) \\
&\leq \mu \exp\left(-\zeta(t - t_{N_\sigma(t)-1})\right) \cdot \mu \exp\left(-\zeta(t_{N_\sigma(t)-1} - t_{N_\sigma(t)-2})\right) V(t^-_{N_\sigma(t)-2}) \\
&\quad \vdots \\
&\leq \mu \exp\left(-\zeta(t - t_{N_\sigma(t)-1})\right) \mu \exp\left(-\zeta(t_{N_\sigma(t)-1} - t_{N_\sigma(t)-2})\right) \cdots \mu \exp\left(-\zeta(t_1 - t_0)\right) V(t_0) \\
&= \mu^{N_\sigma(t_0,t)} \exp\left(-\zeta(t - t_0)\right) V(t_0) \\
&= b\left(\exp\left(-\zeta + (\ln \mu/\vartheta)\right)(t - t_0)\right) V(t_0),
\end{aligned} \tag{4.74}$$

where $b \triangleq \exp\left(N_0 \ln \mu\right)$ is a constant. Substituting the ADT condition $\vartheta > \ln \mu/\zeta$ in (4.74) yields $V(t) < bV(t_0)$ for $t \in [t_0, \; t_0 + T_1)$. Moreover, as $V(t_0 + T_1) < \mathscr{B}$, one has $V(t_{N_\sigma(t)+1}) < \mu\mathscr{B}$ from (4.69) at the next switching instant $t_{N_\sigma(t)+1}$ after $t_0 + T_1$. This implies that $V(t)$ may be larger than $\mathscr{B}$ from the instant $t_{N_\sigma(t)+1}$: however, using a recursive argument as in [81], we can come to the conclusion that $V(t) < b\mu\mathscr{B}$ for $t \in [t_0 + T_1 \;\; \infty)$.

Case (ii): It can be easily verified that the same argument in (4.74) also holds for Case (ii).

Thus, observing the stability arguments of the Case (i) and (ii), the UUB result (4.66) can be concluded, which further implies $\tilde{\boldsymbol{\eta}}, \tilde{\boldsymbol{\nu}}, \hat{\boldsymbol{\eta}}, \hat{\boldsymbol{\nu}} \in \mathscr{L}_\infty \Rightarrow \boldsymbol{\eta}, \boldsymbol{\nu} \in \mathscr{L}_\infty$. □

4.3.4. OVERALL CONTROL STRUCTURE

To summarize, the proposed control law and switching law comprise of the design steps as enumerated in Algorithm 1.

4.3.5. KEY PERFORMANCE INDICATORS:

From (4.66), upper bounds on the position error $\boldsymbol{\eta}$ and control input $\boldsymbol{\tau}$ can be computed. These bounds should serve the purpose of key performance indicators (KPIs).

Algorithm 1 Design steps of the proposed switching controller

Step 1 (preliminary gains): design suitable matrices $\mathbf{H}_\sigma, \mathbf{P}_{2\sigma}$ such that (4.60) is satisfied for user-defined positive scalar β;
Step 2 (observer and control gains): based on the results from Step 1, design $\mathbf{P}_{1\sigma}$, $\mathbf{P}_{3\sigma}, \mathbf{P}_{4\sigma}, \mathbf{K}_{1\sigma}, \mathbf{K}_\sigma, \rho_\sigma$ and $\rho_{1\sigma}$ via (4.55), (4.56), (4.57) and (4.58);
Step 3 (ADT gains): compute the gains $\varrho_{\mathrm{m}}, \varrho_{\mathrm{m}}$, and κ as in (4.61)-(4.63);
Step 4 (observer based robust law): the observer is as in (4.52)-(4.53) with control input $\boldsymbol{\tau}_\sigma$ according to (4.54);
Step 5 (switching law): the system can change dynamics according to any ADT switching law satisfying (4.64) resulting from Step 4. Furthermore, the controller is assumed to be manually switched with no time delay.

4

Using the relations $V \geq (\varrho_{\mathrm{m}}/2)||\boldsymbol{\xi}||^2 \geq (\varrho_{\mathrm{m}}/2)||\hat{\boldsymbol{\eta}}||^2$ and $V \geq (\varrho_{\mathrm{m}}/2)||\boldsymbol{\xi}||^2 \geq (\varrho_{\mathrm{m}}/2)||\tilde{\boldsymbol{\eta}}||^2$, the upper bound on $\boldsymbol{\eta}$ can be computed as follows:

$$||\boldsymbol{\eta}|| = ||\tilde{\boldsymbol{\eta}} + \hat{\boldsymbol{\eta}}|| \leq 2\sqrt{2V/\varrho_{\mathrm{m}}} \leq 2\sqrt{(2/\varrho_{\mathrm{m}})\max\{bV(t_0), b\mu\bar{\mathscr{B}}\}} \triangleq 2\bar{\mathscr{B}}. \tag{4.75}$$

Similarly, an upper bound on $\boldsymbol{\tau}_\sigma$ can be derived from (4.54) as

$$\begin{aligned} ||\boldsymbol{\tau}_\sigma|| &= ||\mathbf{M}_\sigma\{(\hat{\mathbf{A}}_{1\sigma} - \mathbf{K}_{2\sigma} - \mathbf{P}_{4\sigma}^{-1}\mathbf{R}_3^T\mathbf{P}_{3\sigma})\hat{\boldsymbol{\eta}} + (\hat{\mathbf{A}}_{2\sigma} - (\rho_\sigma + \rho_{1\sigma}))\hat{\boldsymbol{\nu}}\}|| \\ &\leq \bar{\mathscr{B}}||\mathbf{M}_\sigma||\{||(\hat{\mathbf{A}}_{1\sigma} - \mathbf{K}_{2\sigma} - \mathbf{P}_{4\sigma}^{-1}\mathbf{R}_3^T\mathbf{P}_{3\sigma})|| + ||(\hat{\mathbf{A}}_{2\sigma} - (\rho_\sigma + \rho_{1\sigma}))||\}. \end{aligned} \tag{4.76}$$

Remark 4.11 (Phase-dependent tuning)**.** *The control bounds in* (4.76) *are different for each phase, i.e. one can tune the gains in* (4.55)-(4.60) *independently for each phase. On the other hand, a single non-switching controller tuned only for one of the three phases might result in a too shallow/too aggressive control in the other phases.*

4.4. SIMULATION EXPERIMENTS

To assess the method proposed in Section 4.2 and Section 4.3, we carry out simulation experiments. Simulations are made with the model proposed in Chapter 3.In this section, we simulate the proposed controllers separately.

4.4.1. SIMULATIONS OF ROBUST CONTROLLER DURING MODE 1

In this section, the performance of the proposed controller is validated under the two following scenarios for a heavy lift vessel in Mode 1 (i.e. the heavy load is fully/partly on the platform):

S1: In the first scenario, the thrusters are considered to be ideal, i.e., no constraint is imposed on its ability of responding to variations in the control input.

S2: In the second scenario, non-ideal thrusters are considered, where low pass filters are used as a limiter in line with Section 4.2.3.

The thrusters on board consist of three bow thrusters and two propellers. The corresponding thrust allocator matrix is $\mathbf{B}_{\mathrm{ta}} = [0.50\ 0\ 0;\ 0.50\ 0\ 0;\ 0\ -2.67\ 0.03;\ 0\ 2.67\ 0;\ 0\ 1.00\ -0.03]$.

The nominal value $\hat{\mathbf{A}}_1$ is chosen based on the highest load during each simulation, when $\mathbf{F} = \mathbf{F}_{\max}$, where $\mathbf{F}_{\max}$ refers to the mooring stiffness $\mathbf{F}$ with maximum crane load. Thus $\hat{\mathbf{A}}_1 = 10^{-3}[2.7261\ 0\ 0;\ 0\ 2.0931\ -0.0004;\ 0\ -0.0004\ 0.0011]$;
nominal value of $\mathbf{A}_2$ is chosen as $\hat{\mathbf{A}}_2 = 10^{-1}[0.1762\ 0\ 0; 0\ 1.1312\ -0.6066; 0\ -0.0003\ 1.3604]$, which is 90% of the actual value of $\mathbf{A}_2$.

Other parameters involved in the simulation are chosen as:

$$\mathbf{M} = 10^{10}\begin{bmatrix} 0.0026 & 0 & 0 \\ 0 & 0.0033 & 0.0015 \\ 0 & 0.0015 & 6.5209 \end{bmatrix}, \tag{4.77}$$

the upper bound of disturbance is chosen as $\Delta\mathbf{d} = [0.1948,\ 1.4940,\ 0.0012]^T$. The upper bounds of the perturbation $\Delta\mathbf{A}_1$ and $\Delta\mathbf{A}_2$ are selected to be 10% and 100% of $\hat{\mathbf{A}}_1$ and $\hat{\mathbf{A}}_2$, respectively. The various control design parameters are selected as $\alpha = 2, \beta = 1$ and $\mathbf{H} = \Delta\mathbf{A}_2$. Consequently, according to (4.18) to (4.22), other control gains can be calculated: $\mathbf{K} = 289.78\mathbf{I}$; $\mathbf{K}_1 = 286.65\mathbf{I}$; $\rho = 1.53$. Apart from these choices, which are kept same for S1 and S2, the additional control parameters for S2 are selected as $\bar{N}_i = 300, N_i = 301$ and $h = 0.01\ \forall i = 1,2,3$. One can verify that such choices result in a minimum phase dynamics for the transfer function (4.25).

Throughout the simulation, the load is considered to be fixed on the platform, and the hoist force is considered to follow the pattern depicted in Figure 4.2: it increases during $0 \le t < 700$s, stays constant from 700s$\le t < 1300$s, and decreases from $t > 1300$s. Such profile emulates the lifting and offloading by a heavy lift vessel in Mode 1.

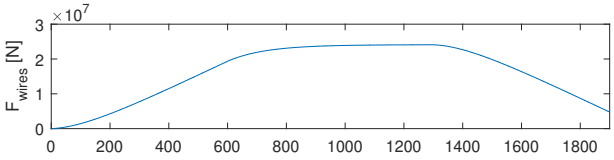

Figure 4.2: Hoist force (F_{hoist})

Simulation in Scenario S1

The simulation results in this scenario are shown in Figure 4.3 to Figure 4.5. Moreover, to study the effectiveness of the proposed scheme, its performance is compared with the design in [105], which employs a nonlinear passive observer in conjunction with a PID controller (cf. [105] for the detailed controller structure): the PID controller is not designed taking into account offshore uncertainties, and it is thus expected to exhibit poor performance during heavy lifting operation. The performance of both the proposed and the PID control strategy can be checked in the first column of Tables 4.4, 4.5 ($\vartheta = 0$). Both the root mean square error (RMSE) and the maximum offset from the desired equilibrium position are reported. From the values in these columns it is possible to see that the proposed approach reduces the RMSE by 89% in North direction, 50% in East direction and 82% in yaw. position error reductions are 95% in North direction, 78% in East direction and 83% in yaw. It is worth noticing that such improved performance is attained in the presence of the mooring forces reported in Figure 4.5.

Comparing to mooring forces in Figure 4.11, the forces and moment in Figure 4.5 are much lower.

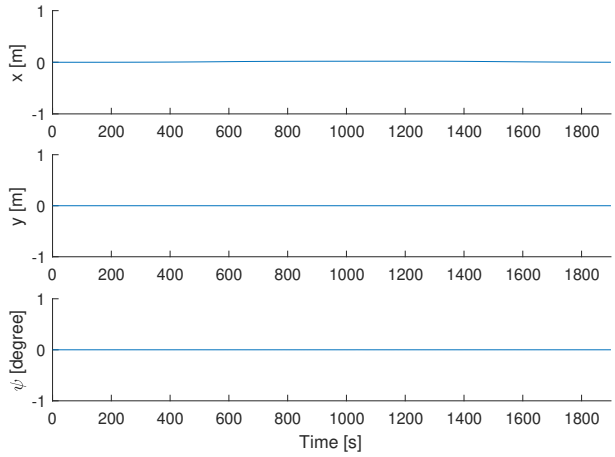

Figure 4.3: Vessel position error ($\boldsymbol{\eta}-\boldsymbol{\eta}_{\mathrm{d}}$) in S1 employing the observer-based robust controller with a maximum load of 2000t under sea state 2

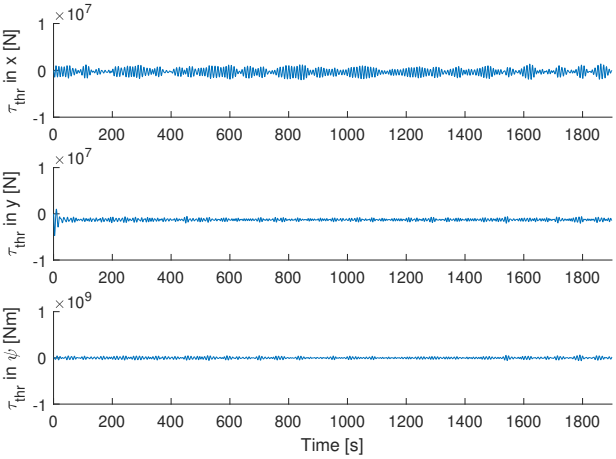

Figure 4.4: Thrust forces and moment ($\boldsymbol{\tau}_{\mathrm{thr}}$) in S1 with the observer-based robust controller with a maximum load of 2000t under sea state 2

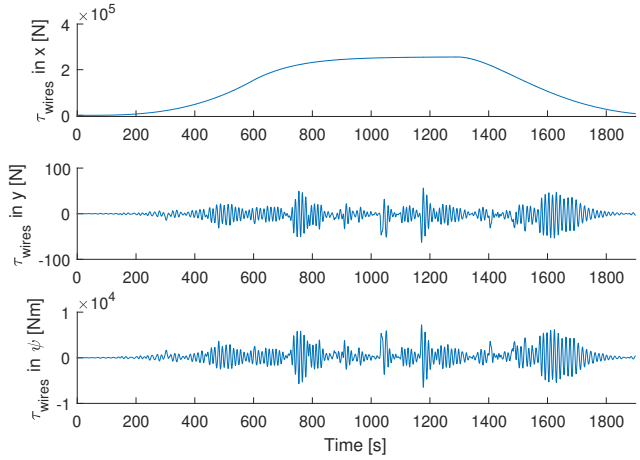

Figure 4.5: Crane force ($\boldsymbol{\tau}_{\text{wires}}$) in S1 with the observer-based robust controller with a maximum load of 2000t under sea state 2

With the assumption that there's no limitation to propulsion systems in S1, the thrust force has a high maximum value of 1.5×10^6N throughout the simulation in surge direction.

More simulations are made with: 1) different maximum loads under sea state 2, 2) and with a maximum load of 2000t under different sea states. The results are shown in Table 4.2 and Table 4.3. Simulation results show that the proposed robust controller is sensitive to the environmental loads. The controller has better performance in lower sea state.

Table 4.2: Simulation results of the proposed robust controller under different sea states

Sea state		0	1	2	3	4
RMSE	North [m]	0.01	0.02	0.06	0.10	0.13
	East [m]	0.00	0.03	0.08	0.08	0.10
	Yaw [°]	0.00	0.01	0.03	0.06	0.09
Maximum Position Error	North [m]	0.01	0.04	0.16	0.36	0.38
	East [m]	0.00	0.09	0.29	0.33	0.21
	Yaw [°]	0.00	0.02	0.11	0.25	0.29

Table 4.3: Simulation results of the proposed robust controller with different loads

Load [tonnes]		1600	1800	2000	2200	2400
RMSE	North [m]	0.04	0.06	0.06	0.05	0.07
	East [m]	0.08	0.08	0.08	0.08	0.08
	Yaw [°]	0.03	0.03	0.03	0.03	0.02
Maximum Position Error	North [m]	0.14	0.16	0.19	0.15	0.19
	East [m]	0.29	0.29	0.30	0.24	0.26
	Yaw [°]	0.09	0.11	0.14	0.09	0.07

Simulation in Scenario S2

In this scenario, the thrust allocators are considered to be embedded with low pass filters having the following characteristic transfer function:

$$H(s) = \frac{1}{\vartheta s + 1}, \tag{4.78}$$

where ϑ denotes the filter time constant.

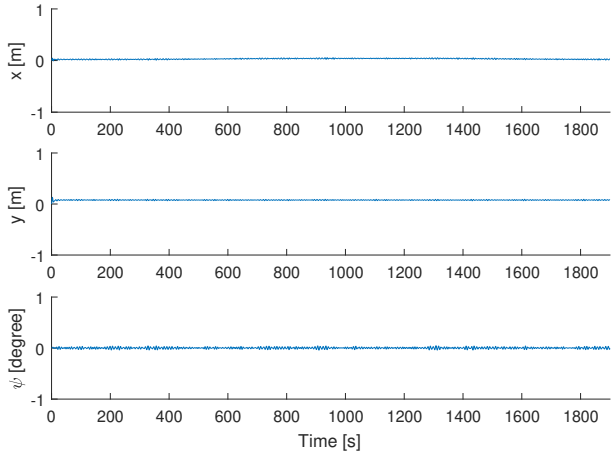

Figure 4.6: Vessel position error ($\boldsymbol{\eta} - \boldsymbol{\eta}_{\mathrm{d}}$) in S2 with the proposed controller, $\vartheta = 3$, with a maximum load of 2000t

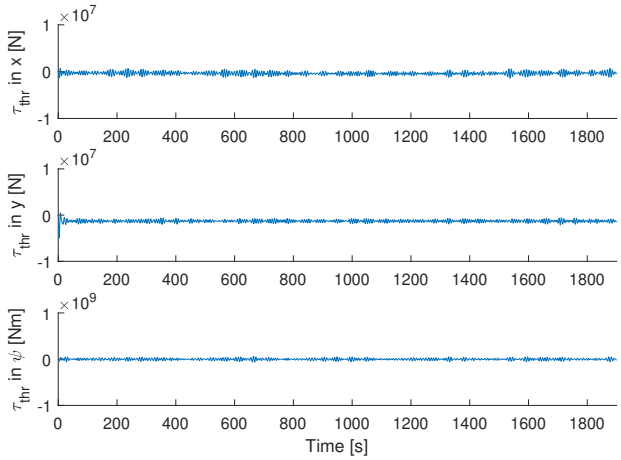

Figure 4.7: Thrust forces and moment ($\boldsymbol{\tau}_{\text{thr}}$) in S2 with the observer-based robust controller, $\vartheta = 3$, with a maximum load of 2000t

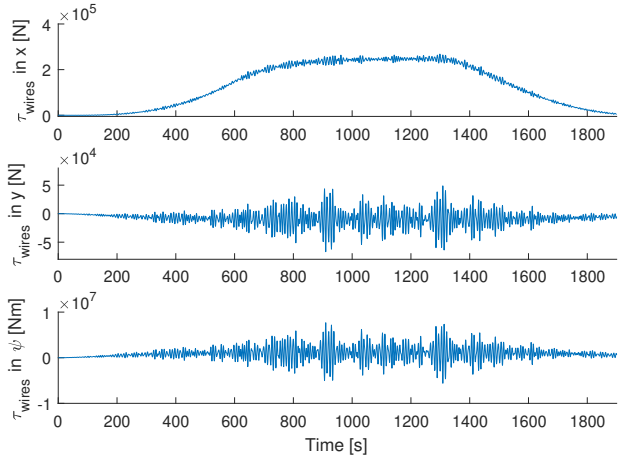

Figure 4.8: Crane force ($\boldsymbol{\tau}_{\text{wires}}$) in S2 with the proposed controller, $\vartheta = 3$, with a maximum load of 2000t

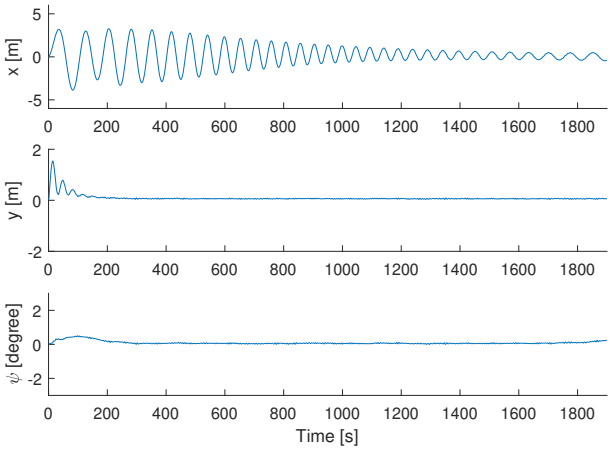

Figure 4.9: Vessel position error ($\boldsymbol{\eta} - \boldsymbol{\eta}_{\mathrm{d}}$) in S2 with PID controller, $\vartheta = 3$, with a maximum load of 2000t

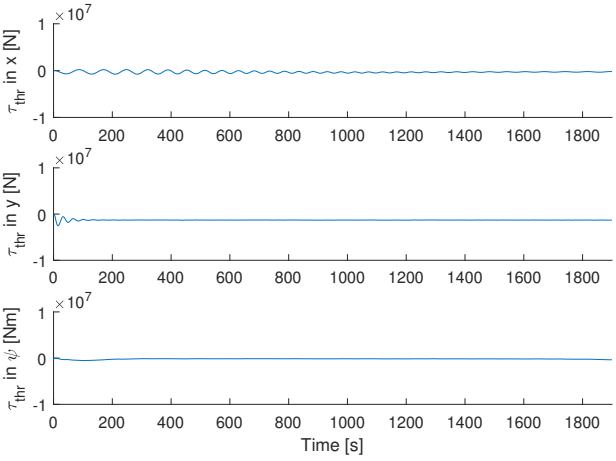

Figure 4.10: Thrust forces and moment ($\boldsymbol{\tau}_{\mathrm{thr}}$) in S2 with PID controller, $\vartheta = 3$, with a maximum load of 2000t

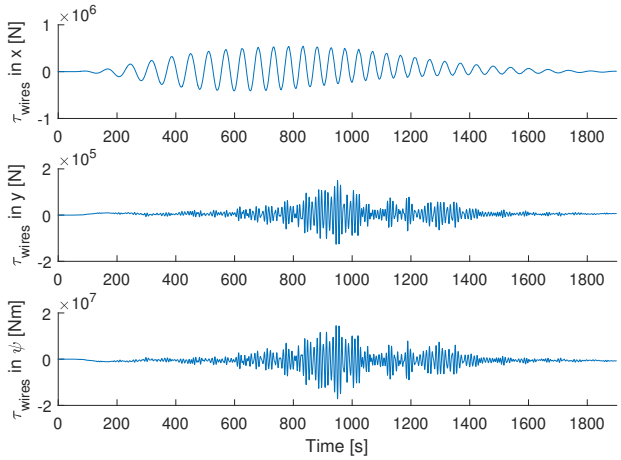

Figure 4.11: Crane force ($\boldsymbol{\tau}_{\text{wires}}$) in S2 with PID controller, $\vartheta = 3$, with a maximum load of 2000t

By comparing Figure 4.4 and Figure 4.7, we can see that the maximum values of the thrust forces and moment are reduced.

The performance of the proposed observer-based switching controller is assessed for five different ϑs as $\vartheta = 1,2,3,4$ and 5. We also use $\vartheta = 0$ to represent the case of ideal thrusters (i.e., Scenario S1). Moreover, in order to study the effectiveness of the proposed scheme, its performance is compared with [105], which employs a nonlinear passive observer in conjunction with a PID controller (cf. [105] for the detailed controller structure). The simulation results are tabulated in Figures 4.6 to 4.11, and Tables 4.4, 4.5, respectively for both scenarios S1 and S2, in terms of root-mean-squared-error (RMSE) and maximum error from the desired equilibrium position.

Table 4.4: Performance of the observer-based controller with low pass filter thruster dynamics

ϑ		0	1	2	3	4	5
RMSE	North [m]	0.05	0.02	0.03	0.03	0.05	0.07
	East [m]	0.08	0.08	0.08	0.08	0.08	0.09
	Yaw [°]	0.03	0.01	0.02	0.03	0.03	0.03
Maximum Position Error	North [m]	0.14	0.04	0.06	0.09	0.20	0.24
	East [m]	0.24	0.14	0.19	0.23	0.26	0.31
	Yaw [°]	0.11	0.04	0.08	0.09	0.11	0.09

Table 4.5: Performance of the PID controller [105] with low pass filter thruster dynamics

ϑ		0	1	2	3	4	5
RMSE	North [m]	0.44	0.52	0.68	1.32	4.76	12.75
	East [m]	0.16	0.16	0.16	0.17	0.18	0.21
	Yaw [°]	0.17	0.12	0.15	0.13	0.12	0.14
Maximum Position Error	North [m]	2.61	2.89	3.15	3.87	13.22	43.70
	East [m]	1.11	1.27	1.43	1.54	1.67	1.79
	Yaw [°]	0.63	0.39	0.55	0.50	0.44	0.52

The tabulated data reveal that with increased ϑ, both the proposed controller and the PID controller [105] loose performance. However, the proposed controller outperforms the PID controller for all ϑ. For the simulated vessel with crane at the aft, the maximum offset in the North direction is of prime importance. Significantly, the maximum offset in this direction for the proposed controller for $\vartheta = 5$ is smaller than the maximum offset controlled with the PID controller with ideal thrust system, i.e., when $\vartheta = 0$. This further substantiates the effectiveness of the proposed scheme.

More simulations are made with different environmental loads, and with different loads. The results are shown in Table 4.6 and Table 4.7. These simulation results show that the controller could handle the offsets in surge, sway within 0.3m, and the yaw angle within 0.3°. The proposed controller is not sensitive with different heavy loads. However, the performance of the controller decreases while the environmental loads increase. With increasing sea state, both the offset of the vessel and the RMSE of the vessel position increase.

Table 4.6: Simulation results of the proposed robust controller under different sea states, $\vartheta = 3$

Sea state		0	1	2	3	4
RMSE	North [m]	0.01	0.02	0.03	0.05	0.06
	East [m]	0.00	0.03	0.08	0.09	0.09
	Yaw [°]	0.00	0.01	0.02	0.06	0.08
Maximum Position Error	North [m]	0.01	0.03	0.09	0.15	0.21
	East [m]	0.00	0.07	0.23	0.25	0.30
	Yaw [°]	0.00	0.02	0.09	0.20	0.30

Table 4.7: Simulation results of the proposed robust controller with different loads, $\vartheta = 3$

Load [tonnes]		1600	1800	2000	2200	2400
RMSE	North [m]	0.03	0.03	0.03	0.04	0.04
	East [m]	0.08	0.08	0.08	0.08	0.08
	Yaw [°]	0.03	0.02	0.02	0.03	0.02
Maximum Position Error	North [m]	0.09	0.08	0.06	0.09	0.10
	East [m]	0.21	0.23	0.23	0.24	0.20
	Yaw [°]	0.08	0.08	0.09	0.11	0.08

4.4.2. ASSESSMENT OF SWITCHING CONTROLLER

The switching controller for a complete offshore heavy lift operation is assessed in this section under both modes. Comparisons of root mean square error (RMSE) of the vessel's position offset and maximum offset of the vessel position in 3 DoFs are made with different thruster dynamics. The following design parameters have been used based on the simulation model and the tuning algorithm 1:

$$\hat{\mathbf{A}}_{11} = \begin{bmatrix} 2.7\cdot10^{-5} & 0 & 0 \\ 0 & 2.1\cdot10^{-5} & -4.2\cdot10^{-9} \\ 0 & -4.2\cdot10^{-9} & 1.1\cdot10^{-8} \end{bmatrix},$$

$$\hat{\mathbf{A}}_{12} = \begin{bmatrix} 1.6\cdot10^{-3} & 0 & 0 \\ 0 & 1.2\cdot10^{-3} & -2.5\cdot10^{-7} \\ 0 & -2.5\cdot10^{-7} & 6.3\cdot10^{-7} \end{bmatrix},$$

$$\hat{\mathbf{A}}_{13} = \begin{bmatrix} 2.7\cdot10^{-4} & 0 & 0 \\ 0 & 2.1\cdot10^{-4} & -4.2\cdot10^{-8} \\ 0 & -4.2\cdot10^{-8} & 1.1\cdot10^{-7} \end{bmatrix},$$

$$\Delta\mathbf{A}_{11} = 0.4\hat{\mathbf{A}}_{11}, \Delta\mathbf{A}_{12} = 0.9\hat{\mathbf{A}}_{12}, \Delta\mathbf{A}_{13} = \hat{\mathbf{A}}_{13}$$

$$\hat{\mathbf{A}}_{21} = \hat{\mathbf{A}}_{22} = \hat{\mathbf{A}}_{23} = \begin{bmatrix} 1.8\cdot10^{-2} & 0 & 0 \\ 0 & 1.2\cdot10^{-1} & -6.3\cdot10^{-2} \\ 0 & 2.7\cdot10^{-5} & 1.4\cdot10^{-1} \end{bmatrix},$$

$$\Delta\mathbf{A}_{21} = \Delta\mathbf{A}_{22} = \Delta\mathbf{A}_{23} = 0.2\hat{\mathbf{A}}_{21},$$

$$\mathbf{P}_{21} = \mathbf{I},\ \mathbf{P}_{11} = \mathbf{P}_{31} = \mathbf{P}_{41} = 10\mathbf{P}_{21},$$

$$\mathbf{P}_{22} = 2\mathbf{I},\ \mathbf{P}_{12} = \mathbf{P}_{32} = \mathbf{P}_{42} = 10\mathbf{P}_{22},$$

$$\mathbf{P}_{23} = 1.5\mathbf{I},\ \mathbf{P}_{13} = \mathbf{P}_{33} = \mathbf{P}_{43} = 10\mathbf{P}_{23},$$

$$\mathbf{H}_1 = 1.1\cdot10^{-3}\mathbf{I}, \mathbf{H}_2 = 2.2\cdot10^{-3}\mathbf{I}, \mathbf{H}_3 = 1.7\cdot10^{-3}\mathbf{I},$$

$$\mathbf{K}_1 = 4.57\mathbf{I}, \mathbf{K}_2 = 4.57\mathbf{I}, \mathbf{K}_3 = 4.57\mathbf{I},$$

$$\mathbf{K}_{11} = 4.57\mathbf{I}, \mathbf{K}_{12} = 4.61\mathbf{I}, \mathbf{K}_{13} = 4.58\mathbf{I},$$

$$\rho_1 = 1.53, \rho_2 = 1.55, \rho_3 = 1.54, \alpha = 2, \beta = 1.$$

where the nominal value of $\mathbf{A}_{1\sigma}$ and $\mathbf{A}_{2\sigma}$ have been chosen based on the nominal knowledge of load, vessel's mass and damping matrix. The above gains and $\zeta = 0.9\kappa$ yield the ADT $\vartheta^* = 9.24$s according to (4.64).

The following simulation scenario is considered:

Phase 0 ($\sigma = 0$) : $0s - 150s$: There's no load in the crane wires; **Phase 1** ($\sigma = 1$) : $150s - 750s$: The load is fixed on the platform, and the hoist force is increasing; **Phase 2** ($\sigma = 2$) : $750s - 900s$: The load is fully lifted, and is free-hanging.

The performance of the proposed controller in Section 4.3 is shown in Figures 4.12 and 4.14. The switching between different σ is done manually assuming no time delay. To further show the performance of the switched design, we formulate a non-switching controller by applying the control gains in (4.52)-(4.54) for $\sigma = 2$ to all three phases. Performance of this non-switching design is shown in Figures 4.15 and 4.16, and are collected in Table 4.8 in terms of root-mean-squared error (RMSE) and maximum offset

of the vessel from the desired set-point. It is crucial to notice that the non-switching controller causes significant position offset and large oscillations (especially in the surge direction), which could cause collision between the platform and the vessel. Such oscillations confirm some reported real-life hazardous scenarios (cf. Figure 1.2 in [4]), and the necessity for switching control. Comparing to the proposed robust controller, the switching controller reduces the offsets and the RMSE of the vessel position largely during the beginning of Mode 2: the RMSE is increased 95% in North and yaw, and 60% in East; and the maximum offset is increased 95% in North, 87% in East, and 95% in yaw.

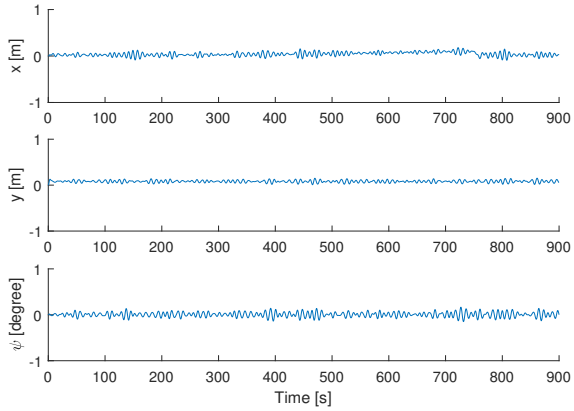

Figure 4.12: Vessel position error ($\boldsymbol{\eta} - \boldsymbol{\eta}_{\mathrm{d}}$) under proposed switched control, with Phase 1 0 – 150s, Phase 2 150s-750s, Phase 3 750s-900s.

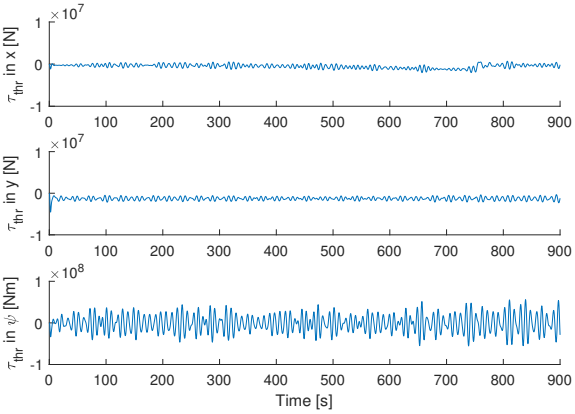

Figure 4.13: Thrust forces and moment ($\boldsymbol{\tau}_{\mathrm{thr}}$) under proposed switched control, with Phase 1 0 – 150s, Phase 2 150s-750s, Phase 3 750s-900s.

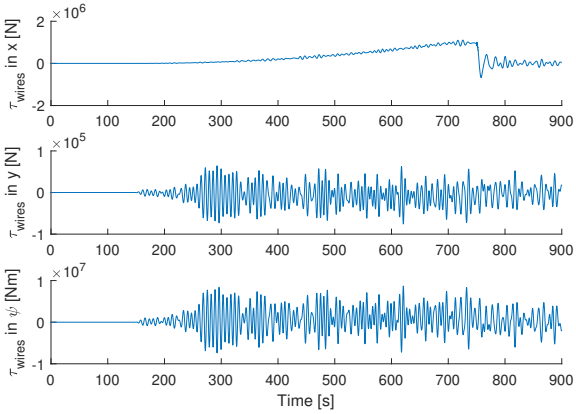

Figure 4.14: Crane force ($\boldsymbol{\tau}_{\text{wires}}$) under proposed switched control, with Phase 1 0 – 150s, Phase 2 150s-750s, Phase 3 750s-900s.

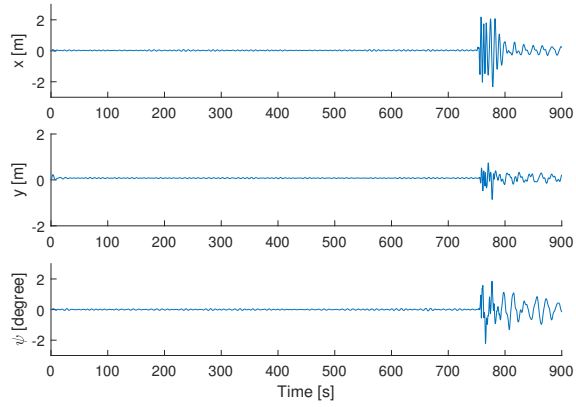

Figure 4.15: Vessel position error ($\boldsymbol{\eta}-\boldsymbol{\eta}_{\text{d}}$) under non-switching control, with Phase 1 0–150s, Phase 2 150s-750s, Phase 3 750s-900s.

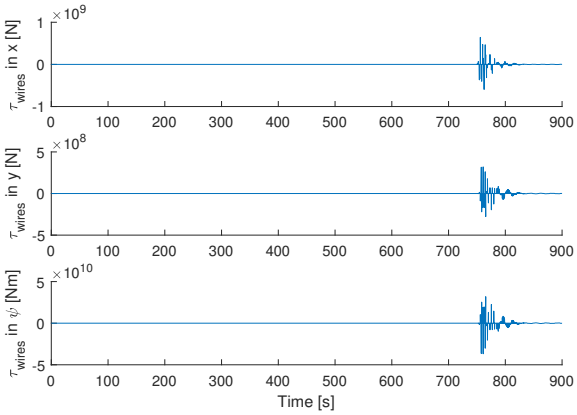

Figure 4.16: Crane force ($\boldsymbol{\tau}_{\text{wires}}$) under non-switching control, with Phase 1 0 – 150s, Phase 2 150s-750s, Phase 3 750s-900s.

Table 4.8: Performance Comparison of the Switching Controller and Non-switching Controller, with Phase 1 0 – 150s, Phase 2 150s-750s, Phase 3 750s-900s.

		Switching Controller			Non-switched Controller		
Phase		1	2	3	1	2	3
RMSE [m]	North	0.03	0.03	0.03	0.03	0.03	0.65
	East	0.1	0.08	0.08	0.08	0.08	0.20
	Yaw	0.02	0.03	0.03	0.02	0.03	0.60
Maximum Position Error [m]	North	0.08	0.08	0.09	0.08	0.08	2.32
	East	0.17	0.11	0.11	0.23	0.11	0.85
	Yaw	0.07	0.09	0.07	0.06	0.08	2.21

Simulations under different environmental loads and with different loads are done to assess the proposed switching controller. Results are shown in Table 4.9 and Table 4.10.

Table 4.9: Simulation results of the proposed switching controller under different sea states

Sea state		0	1	2	3	4
RMSE	North [m]	0.01	0.01	0.03	0.05	0.07
	East [m]	0.00	0.03	0.08	0.09	0.09
	Yaw [°]	0.00	0.00	0.02	0.05	0.09
Maximum Position Error	North [m]	0.07	0.11	0.13	0.14	0.20
	East [m]	0.00	0.05	0.15	0.17	0.20
	Yaw [°]	0.00	0.01	0.07	0.14	0.27

Table 4.10: Simulation results of the proposed switching controller with different loads

Load [tonnes]		1600	1800	2000	2200	2400
RMSE	North [m]	0.03	0.03	0.03	0.03	0.03
	East [m]	0.08	0.08	0.08	0.08	0.08
	Yaw [°]	0.03	0.02	0.02	0.03	0.02
Maximum Position Error	North [m]	0.09	0.11	0.13	0.18	0.21
	East [m]	0.17	0.14	0.15	0.15	0.17
	Yaw [°]	0.08	0.07	0.07	0.09	0.09

From Table 4.10, the RMSE and maximum offset of the vessel position have not improve significantly with different weights of the load. However, simulations under different sea state show that both the RMSE and maximum offset have increased with the increasing sea state (cf. Table 4.6). Thus the proposed controller works better under lower sea state. Under all simulations, the proposed switching controller is able to maintain the vessel's position with a maximum offset of less than 0.20m, and a maximum yaw angle of less than 0.30°.

4.5. CONCLUSIONS

In this chapter, we provided a 3 DoFs vessel model for the design of a DP controller during offshore heavy lift operations. Based on this switching model, a robust DP control method for Mode 1 and a switching control method for both modes are proposed. The latter controller is based on the design of the previous controller. Simulation results are given in figures and tables in order to assess the proposed controllers. Thus we answered research *Subquestion 3: How to solve the DP stability and robustness problem for heavy lift operations during Mode 1?* by designing a robust controller for Mode 1, and answered *Subquestion 4: How to design a DP controller for heavy lift operations considering the mode switching during the operation?* by extend the robust controller into a switching controller for Mode 1 and Mode 2. Comparing to the traditional PID controller, the proposed robust controller reduces the RMSE by 89% in North direction, 50% in East direction and 82% in yaw. Position error reductions are 95% in North direction, 78% in East direction and 83% in yaw. Comparing to the proposed robust controller, the switching controller reduces the offsets and the RMSE of the vessel position largely during the beginning of Mode 2: the RMSE is increased 95% in North and yaw, and 60% in East; and the maximum offset is increased 95% in North, 87% in East, and 95% in yaw. The offset of the vessel with switching controller is limited to 0.20m in East and North direction, and 0.30° in yaw, under sea state 4, which is the worst case scenario in all simulations.

However, the switching of the controller is based on human decision in this chapter. In the next chapter, we will discuss how to automate the switching procedure and reduce human operations on observation of the mode switch.

5

MODE DETECTION SYSTEM

In Chapter 4, an observer-based robust controller is designed for heavy lift operations during Mode 1. Based on the robust controller, a switching DP controller is proposed for offshore heavy lift operations. However, the switching of the controller between different construction modes is assumed to be manually carried out. To achieve an intelligent operation process, we need to design a digital detection system for monitoring the mode switching. Thus the next question we will answer is: *Subquestion 5: How to design a software-based system to detect the switching of the construction mode during offshore heavy lift operations?*

In this chapter, a model-based detection system will be proposed to automatically detect the construction mode switch. In Section 5.1, the outline of the proposed detection system is introduced. In Section 5.2, the details of the design method for the model-based detection system are provided. In Section 5.3, the proposed detection system is then assessed using simulation experiments with the model from Chapter 3. In Section 5.4 the conclusions are given.

5.1. OUTLINE OF THE DETECTION SYSTEM

This section provides the design of a decision-support monitoring system responsible for detecting the changes between two construction modes. It is assumed that there are available sensors to provide measurements of the position and velocity of the crane vessel, and the measurements of the tension force of the lifting wires. The detection system can replace the high level decision making process of the human operators.

An overview of the mode detection system is given in Figure 5.1. The inputs to this system are the sensor measurements and the controlled thrust force of the crane vessel. The output of this system is the decision about the construction mode, i.e., binary decision with 0 and 1 corresponding to "Mode 1" (fixed load) and "Mode 2" (free-hanging load) respectively.

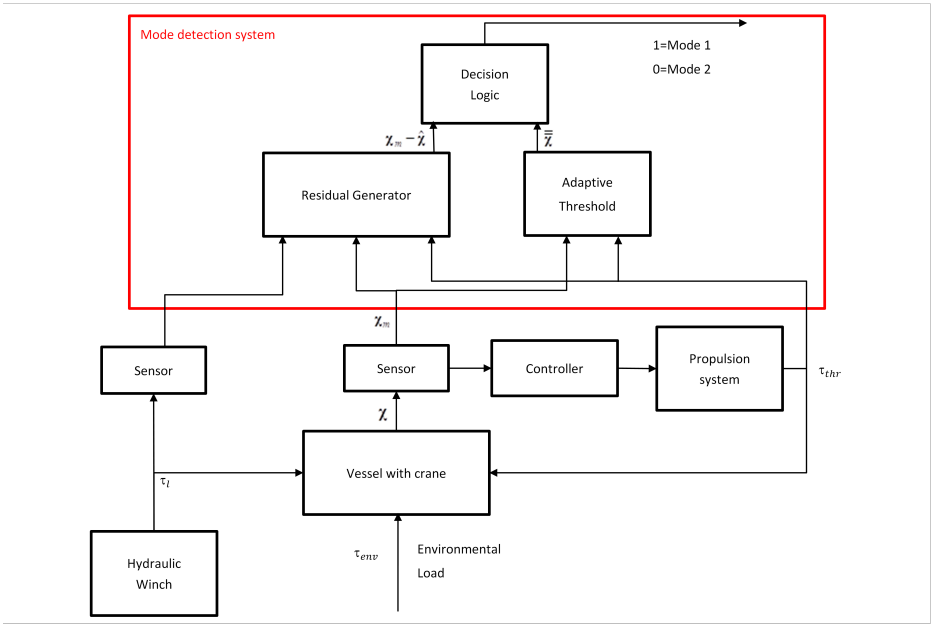

Figure 5.1: Detection system for offshore heavy lift construction

5.2. DESIGN OF MODE DETECTION SYSTEM

As the models of offshore heavy lift operations have already been studied in Chapter 3, we will follow a model-based approach in this chapter to obtain a more precise detection system. The proposed detection system consists of a residual generator, calculation of adaptive threshold, and a decision logic. The equations of motion of the crane vessel and the heavy load are stated in a state-space content. The dependence of signals on time is dropped for simplicity, and only when new variables are introduced, it will be highlighted. The state-space representation is derived by considering the DP of the crane vessel and the lifting of the heavy load by the wires as two interconnected subsystems; i.e., based on (3.5), (3.6) and (3.27), we obtain the following state-space system:

$$\Sigma^{(1)}: \dot{\boldsymbol{\chi}}^{(1)}(t) = \mathbf{A}^{(1)}\boldsymbol{\chi}^{(1)}(t) + \gamma^{(1)}(\boldsymbol{\chi}^{(1)}(t), \mathbf{u}^{(1)}(t)) + h^{(1)}(\boldsymbol{\chi}^{(1)}(t), \mathbf{u}^{(1)}(t), \boldsymbol{\zeta}^{(1)}(t), u_{\zeta}^{(1)}(t)) + \boldsymbol{\omega}_1^{(1)}(t), \tag{5.1}$$

$$\Sigma^{(2)}: \dot{\boldsymbol{\chi}}^{(2)}(t) = \mathbf{A}^{(2)}\boldsymbol{\chi}^{(2)}(t) + \gamma^{(2)}(\boldsymbol{\chi}^{(2)}(t), \mathbf{u}^{(2)}(t)) + h^{(2)}(\boldsymbol{\chi}^{(2)}(t), \mathbf{u}^{(2)}(t), \boldsymbol{\zeta}^{(2)}(t), \mathbf{u}_{\zeta}^{(2)}) + \boldsymbol{\omega}_1^{(2)}(t), \tag{5.2}$$

where $\Sigma^{(1)}$ denotes the first system (i.e., the vessel dynamics), and $\Sigma^{(2)}$ denotes the second system (i.e., the load dynamics) with

$$\boldsymbol{\chi}^{(1)}(t) = \begin{bmatrix} \boldsymbol{\eta}_{\mathrm{v}}(t) \\ \boldsymbol{\nu}_{\mathrm{v}}(t) \end{bmatrix}, \mathbf{u}^{(1)}(t) = \boldsymbol{\tau}_{\mathrm{thr}}(t), \boldsymbol{\zeta}^{(1)}(t) = \begin{bmatrix} \mathbf{I}_{3\times 3} & \mathbf{0}_{3\times 3} & \mathbf{0}_{3\times 1} \end{bmatrix} \boldsymbol{\chi}^{(2)}(t), \mathbf{u}_{\zeta}^{(1)}(t) = F_{\mathrm{hoist}}(t), \tag{5.3}$$

$$\boldsymbol{\chi}^{(2)}(t) = \begin{bmatrix} \boldsymbol{\eta}_{\mathrm{l}}(t) \\ \boldsymbol{\nu}_{\mathrm{l}}(t) \\ \tilde{\delta}(t) \end{bmatrix}, \mathbf{u}^{(2)}(t) = F_{\mathrm{hoist}}(t), \boldsymbol{\zeta}^{(2)}(t) = \begin{bmatrix} \mathbf{I}_{3\times 3} & \mathbf{0}_{3\times 3} & \mathbf{0}_{3\times 6} \end{bmatrix} \boldsymbol{\chi}^{(1)}(t), \mathbf{u}_{\zeta}^{(2)} = 0. \tag{5.4}$$

The first two terms of (5.1) and (5.2) describe the local known dynamics while the third term h represents the interconnection dynamics, and $\boldsymbol{\omega}$ denotes the disturbances. For $\Sigma^{(1)}$,

$$\mathbf{A}^{(1)} = \begin{bmatrix} \mathbf{0} & \mathbf{0} \\ -\overline{\mathbf{M}}^{-1}\mathbf{G}_{\mathrm{v}} & -\overline{\mathbf{M}}^{-1}\mathbf{D}_{\mathrm{v}} \end{bmatrix}, \tag{5.5}$$

$$\gamma^{(1)}(\boldsymbol{\chi}^{(1)}(t), \mathbf{u}^{(1)}(t)) = \begin{bmatrix} \mathbf{R}(\boldsymbol{\Theta}(t))\boldsymbol{\nu}(t) \\ \overline{\mathbf{M}}^{-1}(-\mathbf{C}_{\mathrm{v}}(\boldsymbol{\nu}(t))\boldsymbol{\nu}(t) + \mathbf{u}^{(1)}(t) - \mathbf{G}_{\mathrm{v}}) \end{bmatrix}, \tag{5.6}$$

$$\boldsymbol{\omega}_1^{(1)} = \begin{bmatrix} \mathbf{0} \\ \overline{\mathbf{M}}^{-1}\boldsymbol{\tau}_{\mathrm{e}}(t) \end{bmatrix}. \tag{5.7}$$

The interconnection term in $\Sigma^{(1)}$ can be expressed as:

$$\begin{aligned} & h^{(1)}(\boldsymbol{\chi}^{(1)}(t), \mathbf{u}^{(1)}(t), \boldsymbol{\zeta}^{(1)}(t), u_{\zeta}^{(1)}(t)) \\ &= \begin{bmatrix} \mathbf{0} \\ \overline{\mathbf{M}}^{-1}\boldsymbol{\tau}_{\mathrm{wires}}(t) \end{bmatrix} = \begin{bmatrix} \mathbf{0} \\ \overline{\mathbf{M}}^{-1}\begin{bmatrix} \mathbf{F}_{\mathrm{hoist}}(t) \\ \mathbf{T}_{\mathrm{wires}}(t) \end{bmatrix} \end{bmatrix} \\ &= \begin{bmatrix} \mathbf{0} \\ \overline{\mathbf{M}}^{-1}\begin{bmatrix} \frac{F_{\mathrm{hoist}}(t)}{||\mathbf{R}_3^T(\boldsymbol{\Theta}(t))(\boldsymbol{\eta}_{\mathrm{l}}(t)-\boldsymbol{\eta}(t))-\mathbf{p}_{\mathrm{ct}}||}(\mathbf{R}_3^T(\boldsymbol{\Theta}(t))(\boldsymbol{\eta}_{\mathrm{l}}(t)-\boldsymbol{\eta}(t))-\mathbf{p}_{\mathrm{ct}}) \\ \frac{F_{\mathrm{hoist}}(t)}{||\mathbf{R}_3^T(\boldsymbol{\Theta}(t))(\boldsymbol{\eta}_{\mathrm{l}}(t)-\boldsymbol{\eta}(t))-\mathbf{p}_{\mathrm{ct}}||}\mathbf{r}_{ct} \times (\mathbf{R}_3^T(\boldsymbol{\Theta}(t))(\boldsymbol{\eta}_{\mathrm{l}}(t)-\boldsymbol{\eta}(t))-\mathbf{p}_{\mathrm{ct}}) \end{bmatrix} \end{bmatrix}, \end{aligned} \tag{5.8}$$

where F_{hoist} is the control input with the winch as the actuator during mode 1, or is the uncontrolled force created by the connection through the wires in mode 2 and described by (3.29).

For $\Sigma^{(2)}$, during mode 1, the load position is fixed, thus $\dot{\boldsymbol{\chi}}^{(2)}(t) = \mathbf{0}$, and $\boldsymbol{\eta}_{\mathrm{l}}(t) = \boldsymbol{\eta}_{\mathrm{l}}^{\circ}$, where $\boldsymbol{\eta}_{\mathrm{l}}^{\circ}$ is constant.

The behavior of $\Sigma^{(2)}$ in mode 2 can be expressed by (5.2)as:

$$\mathbf{A}^{(2)} = \begin{bmatrix} \mathbf{0} & \mathbf{I} & \mathbf{0} \\ \mathbf{0} & -\overline{\mathbf{M}}_{\mathrm{l}}^{-1}\mathbf{D}_{\mathrm{l}} & \mathbf{0} \\ \mathbf{0} & \mathbf{0} & -\frac{K_{\mathrm{wires}}}{D_{\mathrm{wires}}} \end{bmatrix}, \tag{5.9}$$

$$\gamma^{(2)}(\boldsymbol{\chi}^{(2)}(t), \mathbf{u}^{(2)}(t)) = \begin{bmatrix} \mathbf{0} \\ -\overline{\mathbf{M}}^{-1}\mathbf{g}_{\mathrm{l}} \\ \frac{u^{(2)}(t)}{D_{\mathrm{wires}}} \end{bmatrix}. \tag{5.10}$$

$$\boldsymbol{\omega}_{\mathrm{l}}^{(2)} = \begin{bmatrix} \mathbf{0} \\ \overline{\mathbf{M}}_{\mathrm{l}}^{-1}\mathbf{F}_{\mathrm{env}}(t) \\ 0 \end{bmatrix}. \tag{5.11}$$

The interconnection term in $\Sigma^{(2)}$ can be expressed as:

$$h^{(2)} = \begin{bmatrix} \mathbf{0} \\ \frac{F_{\mathrm{hoist}}(t)}{||\mathbf{R}_3(\boldsymbol{\Theta}(t))\mathbf{p}_{\mathrm{ct}} + \boldsymbol{\eta}(t) - \boldsymbol{\eta}_{\mathrm{l}}(t)||}\overline{\mathbf{M}}^{-1}(\mathbf{R}_3(\boldsymbol{\Theta}(t))\mathbf{p}_{\mathrm{ct}} + \boldsymbol{\eta}(t) - \boldsymbol{\eta}_{\mathrm{l}}(t)) \\ 0 \end{bmatrix}. \tag{5.12}$$

In order to detect the switching of the construction mode, we define a residual vector that is time-dependent. The residual vector corresponds to the difference between the observed behavior (measured internal state) of system $\Sigma^{(1)}$ denoted by $\boldsymbol{\chi}_{\mathrm{m}}(t) \in \mathbb{R}^{12}$ and its expected behavior denoted by $\hat{\boldsymbol{\chi}}(t) \in \mathbb{R}^{12}$ that is the estimation of its state by a nonlinear observer. A model-based nonlinear observer is designed for the vessel's position and velocity estimation during mode 1, i.e. $\boldsymbol{\eta}_{\mathrm{l}} = \boldsymbol{\eta}^{\circ}$, based on (5.1), (5.3), and (5.5)-(5.8). The residual $\boldsymbol{\chi}_{\mathrm{m}}(t) - \hat{\boldsymbol{\chi}}(t)$ is then compared to the adaptive threshold denoted by $\bar{\bar{\boldsymbol{\chi}}}(t) \in \mathbb{R}^{12}$. If the magnitude of one or more residual is larger than the adaptive threshold, then it is inferred that the construction mode is 1, meaning that the load is lifted up. The designed nonlinear observer, adaptive threshold, and decision logic are described separately in this section.

5.2.1. RESIDUAL GENERATION

We will only use the measurements of system $\Sigma 1$ in the detection system, and will detect the mode change based on the dynamics of system $\Sigma 1$. In the rest of this chapter, we will drop the superscript $^{(1)}$ for simplicity. The nonlinear observer is designed as:

$$\dot{\hat{\boldsymbol{\chi}}}(t) = \mathbf{A}\hat{\boldsymbol{\chi}}(t) + \gamma(\boldsymbol{\chi}_{\mathrm{m}}(t), \mathbf{u}(t)) + h(\boldsymbol{\chi}_{\mathrm{m}}(t), \mathbf{u}(t), \boldsymbol{\zeta}, \mathbf{u}_{\zeta}(t)) + \mathbf{K}(\boldsymbol{\chi}_{\mathrm{m}}(t) - \hat{\boldsymbol{\chi}}(t)), \tag{5.13}$$

$$\boldsymbol{\zeta} = \boldsymbol{\eta}_{\mathrm{l}} = \boldsymbol{\eta}_{\mathrm{l}}^{\circ}, \tag{5.14}$$

where $\hat{\boldsymbol{\chi}}(t) \in \mathbb{R}^{12}$ is the estimated value of $\boldsymbol{\chi}$, $\boldsymbol{\chi}_{\mathrm{m}}(t) = [\boldsymbol{\eta}_{\mathrm{m}}, \boldsymbol{\nu}_{\mathrm{m}}]^T \in \mathbb{R}^{12}$ is the measurement of the vessel position and vessel velocity, the measurement

$$\boldsymbol{\chi}_{\mathrm{m}} = \boldsymbol{\chi} + \boldsymbol{\omega}_2, \tag{5.15}$$

where $\boldsymbol{\omega}_2(t) = [\boldsymbol{\omega}_{\eta}, \boldsymbol{\omega}_{\nu}]^T \in \mathbb{R}^{12}$ is the measurement noise, and $\mathbf{K} \in \mathbb{R}^{12\times 12}$ is the observer gain.

By using (5.1), (5.5)-(5.8) and (5.13), the state estimation error dynamics can be expressed as

$$\begin{aligned}\dot{\tilde{\boldsymbol{\chi}}} =&(\mathbf{A}-\mathbf{K})\tilde{\boldsymbol{\chi}} + (\gamma(\boldsymbol{\chi},\mathbf{u}) - \gamma(\boldsymbol{\chi}_{\mathrm{m}},\mathbf{u}))\\ &+ (h(\boldsymbol{\chi},\mathbf{u},\boldsymbol{\zeta},\mathbf{u}_{\zeta}) - h(\boldsymbol{\chi}_{\mathrm{m}},\mathbf{u},\boldsymbol{\zeta},\mathbf{u}_{\zeta})) + \boldsymbol{\omega}_1 - \mathbf{K}\boldsymbol{\omega}_2,\end{aligned} \tag{5.16}$$

where

$$\tilde{\boldsymbol{\chi}}(t) = \boldsymbol{\chi}(t) - \hat{\boldsymbol{\chi}}(t). \tag{5.17}$$

In order to estimate the states properly, we need a stable observer that could provide $\tilde{\chi} \to \mathbf{0}$ without any disturbances or measurement noise. For the stability of the observer, the gain $\mathbf{K}$ should be chosen such that matrix $\mathbf{A}-\mathbf{K}$ is Hurwitz Matrix as we analyze next.

By using (5.15), (5.17), the residual vector $\boldsymbol{\chi}_{\mathrm{m}} - \hat{\boldsymbol{\chi}}$ can be described with respect to the state estimation error as

$$\boldsymbol{\chi}_{\mathrm{m}}(t) - \hat{\boldsymbol{\chi}}(t) = \tilde{\boldsymbol{\chi}}(t) + \boldsymbol{\omega}_2(t). \tag{5.18}$$

Remark 5.1. *Considering the dynamic positioning system and the lifting of the load as two interconnected operations enables us to design the state-space observer given in* (5.13) *for the crane-vessel dynamics, i.e., for* $\Sigma^{(1)}$ *including only the dynamics of the system* $\Sigma^{(2)}$ *that affect* $\Sigma^{(1)}$ *due to the interconnection modeled by h. In this way, we have an observer of order 12 instead of an observer of order 19, which could be designed if we follow a centralized approach to estimate the state* $[\boldsymbol{\chi}^{(1)};\boldsymbol{\chi}^{(2)}]$ *of the crane-vessel-load system. This design leads to a smaller number of residuals and corresponding adaptive thresholds that should be checked online according to the decision logic presented in Section 5.2.3.*

5.2.2. ADAPTIVE THRESHOLD

Due to the presence of the bounded unknown disturbances and measurement noise (i.e., $\boldsymbol{\omega}_1$ and $\boldsymbol{\omega}_2$), the observed behavior always deviates from the measured data, which means that the residual will never be zero. To detect the change of the construction mode through the residual vector $\boldsymbol{\chi}_{\mathrm{m}}(t) - \hat{\boldsymbol{\chi}}(t)$, we compare at every time instant the residual vector to an adaptive threshold vector $\bar{\tilde{\boldsymbol{\chi}}}(t)$. This adaptive threshold vector is obtained assuming:

- the crane vessel and the heavy load are operating in mode 1;
- the disturbances and the measurement noise are unknown but bounded, i.e., $|\boldsymbol{\omega}_1(t)| \leq \bar{\boldsymbol{\omega}}_1$ and $|\boldsymbol{\omega}_2(t)| \leq \bar{\boldsymbol{\omega}}_2$ for all $t > 0$ with $\bar{\boldsymbol{\omega}}_1$ and $\bar{\boldsymbol{\omega}}_2$ being positive constants;
- the position of the crane load during mode 1 and the hoist force are exactly known.

The adaptive threshold is defined such that:

$$|\boldsymbol{\chi}_{\mathrm{m}}(t) - \hat{\boldsymbol{\chi}}(t)| \leq \bar{\tilde{\boldsymbol{\chi}}}(t), \tag{5.19}$$

where $\bar{\tilde{\boldsymbol{\chi}}}(t) \in \mathbb{R}^{12}$ is the adaptive threshold of the detection system.

The triangular inequality is used to calculate the threshold: *In Euclidean geometry and some other geometries, the triangle inequality is a theorem about distances, and it is written using vectors and vector lengths (norms):*

$$|\pm\mathbf{b}| \leq |\mathbf{a}| + |\mathbf{b}|. \tag{5.20}$$

Using (5.18) and applying the triangular inequality results in:

$$|\boldsymbol{\chi}_{\mathrm{m}}(t) - \hat{\boldsymbol{\chi}}(t)| \leq |\tilde{\boldsymbol{\chi}}(t)| + \bar{\boldsymbol{\omega}}_2(t) \leq \bar{\boldsymbol{\chi}}(t) + \bar{\boldsymbol{\omega}}_2(t) \triangleq \bar{\tilde{\boldsymbol{\chi}}}(t), \tag{5.21}$$

where $\bar{\boldsymbol{\omega}}_2(t) = [\bar{\boldsymbol{\omega}}_\eta(t), \bar{\boldsymbol{\omega}}_v(t)] = [\bar{\omega}_x, \bar{\omega}_y, \bar{\omega}_z, \bar{\omega}_\phi, \bar{\omega}_\theta, \bar{\omega}_\psi, \bar{\omega}_u, \bar{\omega}_v, \bar{\omega}_w, \bar{\omega}_p, \bar{\omega}_q, \bar{\omega}_r]$ is the measurement noise bound, and $\bar{\boldsymbol{\chi}}(t) \in \mathbb{R}^{12}$ is the adaptive bound on the state estimation error, i.e.

$$|\tilde{\boldsymbol{\chi}}| \leq \bar{\boldsymbol{\chi}}. \tag{5.22}$$

The bound $\bar{\boldsymbol{\chi}}$ can be calculated by solving the differential equation and applying the triangular inequality. Let us consider the following decomposition of the matrix $\mathbf{A} - \mathbf{K}$, we can assume

$$\mathbf{A} - \mathbf{K} = \boldsymbol{\lambda}, \tag{5.23}$$

where $\boldsymbol{\lambda} \in \mathbb{R}^{12\times 12}$ is the diagonal matrix $\boldsymbol{\lambda} = diag\{\lambda_1, \cdots, \lambda_{12}\}$ with elements of eigenvalues of the Hurwitz matrix $\mathbf{A} - \mathbf{K}$.

Based on (5.23), (5.17) can then be expressed as:

$$\dot{\tilde{\boldsymbol{\chi}}} = \boldsymbol{\lambda}\tilde{\boldsymbol{\chi}} + \tilde{\gamma} + \tilde{h} + \boldsymbol{\omega}_1 - (\mathbf{A} - \boldsymbol{\lambda})\boldsymbol{\omega}_2. \tag{5.24}$$

Solution of the equation above is:

$$\begin{aligned}\tilde{\boldsymbol{\chi}} &= e^{\boldsymbol{\lambda} t}\tilde{\boldsymbol{\chi}}(0) + \int_0^t e^{\boldsymbol{\lambda}(t-\tau)}[\tilde{\gamma} + \tilde{h} + \boldsymbol{\omega}_1 - (\mathbf{A} - \boldsymbol{\lambda})\boldsymbol{\omega}_2]d\tau \\ &= e^{\boldsymbol{\lambda} t}\tilde{\boldsymbol{\chi}}(0) + \int_0^t e^{\boldsymbol{\lambda}(t-\tau)}[\boldsymbol{\omega}_1 - (\mathbf{A} - \boldsymbol{\lambda})\boldsymbol{\omega}_2]d\tau + \int_0^t e^{\boldsymbol{\lambda}(t-\tau)}(\tilde{\gamma} + \tilde{h})d\tau,\end{aligned} \tag{5.25}$$

where $\tilde{\gamma}(t) = \gamma(\boldsymbol{\chi}, \mathbf{u}) - \gamma(\boldsymbol{\chi}_{\mathrm{m}}, \mathbf{u})$, and $\tilde{h}(t) = h(\boldsymbol{\chi}, \mathbf{u}, \boldsymbol{\zeta}, \mathbf{u}_\zeta) - h(\boldsymbol{\chi}_{\mathrm{m}}, \mathbf{u}, \boldsymbol{\zeta}, \mathbf{u}_\zeta)$.

Based on (5.25), $\tilde{\boldsymbol{\chi}}$ satisfies

$$|\tilde{\boldsymbol{\chi}}| \leq e^{\boldsymbol{\lambda} t}|\tilde{\boldsymbol{\chi}}(0)| + e^{\boldsymbol{\lambda} t}\int_0^t e^{-\boldsymbol{\lambda}\tau}(\bar{\boldsymbol{\omega}}_1 + |\mathbf{K}|\bar{\boldsymbol{\omega}}_2)d\tau + \int_0^t e^{\boldsymbol{\lambda}(t-\tau)}(\bar{\gamma}(\tau) + \bar{h}(\tau))d\tau. \tag{5.26}$$

According to the definition of first order filters in time domain, the last term of (5.26) is the output of a stable first order filter $\mathbf{H}(s)$ with input $\bar{\gamma} + \bar{h}$, with

$$\mathbf{H}(s) = diag\{\ H_1(s) \quad H_2(s) \quad \cdots \quad H_{12}(s)\ \}, \tag{5.27}$$

where $H_j(s) = \frac{1}{s-\lambda_j}$, for $j = 1, 2, ..., 12$.

Thus we have the adaptive bound $\bar{\boldsymbol{\chi}}$:

$$\bar{\boldsymbol{\chi}}(t) = e^{\boldsymbol{\lambda} t}\bar{\boldsymbol{\chi}}(0) + [-\boldsymbol{\lambda}^{-1}(\mathbf{I} - e^{\boldsymbol{\lambda} t})(\bar{\boldsymbol{\omega}}_1 + |\mathbf{K}|\bar{\boldsymbol{\omega}}_2)] + \mathbf{H}(s)(\bar{\gamma}(t) + \bar{h}(t)), \tag{5.28}$$

where $\bar{\boldsymbol{\chi}}(0)$ is the upper bound for the initial estimation error, $\bar{\boldsymbol{\omega}}_1 \in \mathbb{R}^{12}$ is the bound for the environmental load, $\boldsymbol{\lambda} = diag\{\lambda_1, \lambda_2, \cdots, \lambda_{12}\}$ is the diagonal matrix with the real negative eigen values of $\mathbf{A}-\mathbf{K}$, and $\mathbf{H}(s)$ is a stable first-order filter defined by elements in $\boldsymbol{\lambda}$ (see [47]). Next we will explain how to calculate $\bar{\gamma}(t)$ and $\bar{h}(t)$.

From (5.28), we know that $\bar{\gamma}(t) \in \mathbb{R}^{12}$ is the adaptive bound on $|\gamma(\boldsymbol{\chi}, \mathbf{u}) - \gamma(\boldsymbol{\chi}_{\mathrm{m}}, \mathbf{u})|$. The calculation of $\bar{\gamma}$ is described next.

Based on (5.2), we can get

$$\gamma(\boldsymbol{\chi}, \mathbf{u}) - \gamma(\boldsymbol{\chi}_{\mathrm{m}}, \mathbf{u}) = \begin{bmatrix} \mathbf{R}(\boldsymbol{\eta})\boldsymbol{\nu} - \mathbf{R}(\boldsymbol{\eta}_{\mathrm{m}})\boldsymbol{\nu}_{\mathrm{m}} \\ \overline{\mathbf{M}}^{-1}[-\mathbf{C}_{\mathrm{v}}(\boldsymbol{\nu})\boldsymbol{\nu} - (-\mathbf{C}_{\mathrm{v}}(\boldsymbol{\nu}_{\mathrm{m}})\boldsymbol{\nu}_{\mathrm{m}})] \end{bmatrix}. \tag{5.29}$$

In (5.29),

$$\begin{aligned} &\mathbf{R}(\boldsymbol{\eta})\boldsymbol{\nu} - \mathbf{R}(\boldsymbol{\eta}_{\mathrm{m}})\boldsymbol{\nu}_{\mathrm{m}} \\ &= \mathbf{R}(\boldsymbol{\eta})\boldsymbol{\nu} - \mathbf{R}(\boldsymbol{\eta})\boldsymbol{\nu}_{\mathrm{m}} + \mathbf{R}(\boldsymbol{\eta})\boldsymbol{\nu}_{\mathrm{m}} - \mathbf{R}(\boldsymbol{\eta}_{\mathrm{m}})\boldsymbol{\nu}_{\mathrm{m}} \\ &= -\mathbf{R}(\boldsymbol{\eta})\boldsymbol{\omega}_{\nu} + (\mathbf{R}(\boldsymbol{\eta}) - \mathbf{R}(\boldsymbol{\eta}_{\mathrm{m}}))\boldsymbol{\nu}_{\mathrm{m}}, \end{aligned} \tag{5.30}$$

where

$$|\mathbf{R}(\boldsymbol{\eta})\boldsymbol{\omega}_{\nu}| \leq \begin{bmatrix} ||\bar{\boldsymbol{\omega}}_{\nu}^{1-3}|| \\ ||\bar{\boldsymbol{\omega}}_{\nu}^{1-3}|| \\ ||\bar{\boldsymbol{\omega}}_{\nu}^{1-3}|| \\ ||\bar{\boldsymbol{\omega}}_{\nu}^{4-6}|| \\ ||\bar{\boldsymbol{\omega}}_{\nu}^{4-6}|| \\ ||\bar{\boldsymbol{\omega}}_{\nu}^{4-6}|| \end{bmatrix}, \tag{5.31}$$

where $\bar{\boldsymbol{\omega}}_{\nu}$ is the upper bound of the measurement noise $\boldsymbol{\omega}_{\nu}$, $\bar{\boldsymbol{\omega}}_{\nu}^{i-j}$ represents the vector with i-th to j-th elements in $\bar{\boldsymbol{\omega}}_{\nu}$.

Assume $(\mathbf{R}(\boldsymbol{\eta}) - \mathbf{R}(\boldsymbol{\eta}_{\mathrm{m}}))\boldsymbol{\nu}_{\mathrm{m}} = [a_{\mathrm{n}1}, a_{\mathrm{n}2}, a_{\mathrm{n}3}, a_{\mathrm{n}4}, a_{\mathrm{n}5}, a_{\mathrm{n}6}]^T$, then we have,

$$\begin{aligned} a_{\mathrm{n}1} &= (c_{\phi}c_{\theta} - c_{\phi_{\mathrm{m}}}c_{\theta_{\mathrm{m}}})u_{\mathrm{m}} + (c_{\psi}s_{\theta}s_{\phi} - s_{\psi}c_{\phi} - c_{\psi_{\mathrm{m}}}s_{\theta_{\mathrm{m}}}s_{\phi_{\mathrm{m}}} + s_{\psi_{\mathrm{m}}}c_{\phi_{\mathrm{m}}})v_{\mathrm{m}} \\ &\quad + (s_{\psi}s_{\phi} + c_{\psi}c_{\phi}s_{\theta} - s_{\psi_{\mathrm{m}}}s_{\phi_{\mathrm{m}}} - c_{\psi_{\mathrm{m}}}c_{\phi_{\mathrm{m}}}s_{\theta_{\mathrm{m}}})w_{\mathrm{m}}, \end{aligned} \tag{5.32}$$

$$\begin{aligned} a_{\mathrm{n}2} &= (s_{\psi}c_{\theta} - s_{\psi_{\mathrm{m}}}c_{\theta_{\mathrm{m}}})u_{\mathrm{m}} + (c_{\psi}c_{\phi} + s_{\phi}s_{\theta}s_{\psi} - c_{\psi_{\mathrm{m}}}c_{\phi_{\mathrm{m}}} - s_{\phi_{\mathrm{m}}}s_{\theta_{\mathrm{m}}}s_{\psi_{\mathrm{m}}})v_{\mathrm{m}} \\ &\quad + (s_{\theta}s_{\psi}c_{\phi} - c_{\psi}s_{\phi} - s_{\theta_{\mathrm{m}}}s_{\psi_{\mathrm{m}}}c_{\phi_{\mathrm{m}}} + c_{\psi_{\mathrm{m}}}s_{\phi_{\mathrm{m}}})w_{\mathrm{m}}, \end{aligned} \tag{5.33}$$

$$a_{\mathrm{n}3} = (s_{\theta_{\mathrm{m}}} - s_{\theta})u_{\mathrm{m}} + (c_{\theta}s_{\phi} - c_{\theta_{\mathrm{m}}}s_{\phi_{\mathrm{m}}})v_{\mathrm{m}} + (c_{\theta}c_{\phi} - c_{\theta_{\mathrm{m}}}c_{\phi_{\mathrm{m}}})w_{\mathrm{m}}, \tag{5.34}$$

$$a_{\mathrm{n}4} = (s_{\phi}t_{\theta} - s_{\phi_{\mathrm{m}}}t_{\theta_{\mathrm{m}}})q_{\mathrm{m}} + (c_{\phi}t_{\theta} - c_{\phi_{\mathrm{m}}}t_{\theta_{\mathrm{m}}})r_{\mathrm{m}}, \tag{5.35}$$

$$a_{\mathrm{n}5} = (c_{\phi} - c_{\phi_{\mathrm{m}}})q_{\mathrm{m}} + (s_{\phi_{\mathrm{m}}} - s_{\phi})r_{\mathrm{m}}, \tag{5.36}$$

$$a_{\mathrm{n}6} = (s_{\phi}/c_{\theta} - s_{\phi_{\mathrm{m}}}/c_{\theta_{\mathrm{m}}})q_{\mathrm{m}} + (c_{\phi}/c_{\theta} - c_{\phi_{\mathrm{m}}}/c_{\theta_{\mathrm{m}}})r_{\mathrm{m}}, \tag{5.37}$$

where $s_{\bullet}$, $c_{\bullet}$ denote $sin(\bullet)$ and $cos(\bullet)$ respectively.

An example for the calculation procedure of the boundary of $c_{\phi}c_{\theta} - c_{\phi_{\mathrm{m}}}c_{\theta_{\mathrm{m}}}$ is given

below:

$$c_\phi c_\theta - c_{\phi_\mathrm{m}} c_{\theta_\mathrm{m}} \tag{5.38}$$
$$= \frac{1}{2}(c_{\phi-\theta} + c_{\phi+\theta}) - \frac{1}{2}(c_{\phi_\mathrm{m}-\theta_\mathrm{m}} + c_{\phi_\mathrm{m}+\theta_\mathrm{m}}) \tag{5.39}$$
$$= \frac{1}{2}(c_{(\phi_\mathrm{m}-\omega_\phi)-(\theta_\mathrm{m}-\omega_\theta)} - c_{\phi_\mathrm{m}-\theta_\mathrm{m}}) + \frac{1}{2}(c_{(\phi_\mathrm{m}-\omega_\phi)+(\theta_\mathrm{m}-\omega_\theta)} - c_{\phi_\mathrm{m}+\theta_\mathrm{m}}) \tag{5.40}$$
$$= -s_{\frac{1}{2}(2\phi_\mathrm{m}-\omega_\phi-2\theta_\mathrm{m}+\omega_\theta)} s_{\frac{1}{2}(\omega_\theta-\omega_\phi)} - s_{\frac{1}{2}(2\phi_\mathrm{m}-\omega_\phi+2\theta_\mathrm{m}-\omega_\theta)} s_{\frac{1}{2}(-\omega_\phi-\omega_\theta)} \tag{5.41}$$
$$\leq \bar{\omega}_\theta + \bar{\omega}_\phi. \tag{5.42}$$

By assuming that the roll, pitch, and yaw angle of the vessel are small under DP control, the sine values of the angles approximately equals the values of the angles in rad, and the cosine values of the angles approximately equals 0. Then the boundary of $a_{\mathrm{n}1}, a_{\mathrm{n}2}, a_{\mathrm{n}3}, a_{\mathrm{n}4}, a_{\mathrm{n}5}$, and $a_{\mathrm{n}6}$ can be calculated as follows. For $i \in \{1, \cdots, 6\}$, denote $\bar{a}_{\mathrm{n}i}$ to be the upper bound of $a_{\mathrm{n}i}$, and assume $|(\mathbf{R}(\boldsymbol{\eta}) - \mathbf{R}(\boldsymbol{\eta}_\mathrm{m}))\boldsymbol{\nu}_\mathrm{m}| \leq |\bar{\mathbf{R}}\boldsymbol{\nu}_\mathrm{m}|$, then,

$$\bar{a}_{\mathrm{n}1} = (\bar{\omega}_\theta + \bar{\omega}_\phi)|u_\mathrm{m}| + (\bar{\omega}_\theta + 2\bar{\omega}_\phi + 2\bar{\omega}_\psi)|v_\mathrm{m}| + (\bar{\omega}_\theta + 2\bar{\omega}_\phi + 2\bar{\omega}_\psi)|w_\mathrm{m}|, \tag{5.43}$$
$$\bar{a}_{\mathrm{n}2} = (\bar{\omega}_\theta + \bar{\omega}_\psi)|u_\mathrm{m}| + (\bar{\omega}_\theta + 2\bar{\omega}_\phi + 2\bar{\omega}_\psi)|v_\mathrm{m}| + (\bar{\omega}_\theta + 2\bar{\omega}_\phi + 2\bar{\omega}_\psi)|w_\mathrm{m}|, \tag{5.44}$$
$$\bar{a}_{\mathrm{n}3} = \bar{\omega}_\theta|u_\mathrm{m}| + (\bar{\omega}_\theta + 2\bar{\omega}_\phi + 2\bar{\omega}_\psi)|v_\mathrm{m}| + (\bar{\omega}_\theta + 2\bar{\omega}_\phi + 2\bar{\omega}_\psi)|w_\mathrm{m}|, \tag{5.45}$$
$$\bar{a}_{\mathrm{n}4} = \frac{\bar{\omega}_\phi + 2\bar{\omega}_\theta}{1 - 2\bar{\omega}_\theta}|q_\mathrm{m}| + \frac{\bar{\omega}_\phi + 2\bar{\omega}_\theta}{1 - 2\bar{\omega}_\theta}|r_\mathrm{m}|, \tag{5.46}$$
$$\bar{a}_{\mathrm{n}5} = \bar{\omega}_\phi|q_\mathrm{m}| + \bar{\omega}_\phi|r_\mathrm{m}|, \tag{5.47}$$
$$\bar{a}_{\mathrm{n}6} = \frac{\bar{\omega}_\phi + \bar{\omega}_\theta}{1 - 2\bar{\omega}_\theta}|q_\mathrm{m}| + \frac{\bar{\omega}_\phi + \bar{\omega}_\theta}{1 - 2\bar{\omega}_\theta}|r_\mathrm{m}|. \tag{5.48}$$

Thus,

$$\bar{\mathbf{R}}(\bar{\boldsymbol{\omega}}_\eta) = \begin{bmatrix} \bar{\omega}_\theta + \bar{\omega}_\phi & \bar{\omega}_\theta + 2\bar{\omega}_\phi + 2\bar{\omega}_\psi & \bar{\omega}_\theta + 2\bar{\omega}_\phi + 2\bar{\omega}_\psi & 0 & 0 & 0 \\ \bar{\omega}_\theta + \bar{\omega}_\psi & \bar{\omega}_\theta + 2\bar{\omega}_\phi + 2\bar{\omega}_\psi & \bar{\omega}_\theta + 2\bar{\omega}_\phi + 2\bar{\omega}_\psi & 0 & 0 & 0 \\ \bar{\omega}_\theta & \bar{\omega}_\theta + 2\bar{\omega}_\phi + 2\bar{\omega}_\psi & \bar{\omega}_\theta + 2\bar{\omega}_\phi + 2\bar{\omega}_\psi & 0 & 0 & 0 \\ 0 & 0 & 0 & 0 & \frac{\bar{\omega}_\phi + 2\bar{\omega}_\theta}{1 - 2\bar{\omega}_\theta} & \frac{\bar{\omega}_\phi + 2\bar{\omega}_\theta}{1 - 2\bar{\omega}_\theta} \\ 0 & 0 & 0 & 0 & \bar{\omega}_\phi & \bar{\omega}_\phi \\ 0 & 0 & 0 & 0 & \frac{\bar{\omega}_\phi + \bar{\omega}_\theta}{1 - 2\bar{\omega}_\theta} & \frac{\bar{\omega}_\phi + \bar{\omega}_\theta}{1 - 2\bar{\omega}_\theta} \end{bmatrix}. \tag{5.49}$$

Now we calculate the second element of the vector shown in (5.29). The Coriolis term for the vessel which is symmetric around x-z plane is expressed as:

$$\mathbf{C}_\mathrm{v}(\boldsymbol{\nu}) = \begin{bmatrix} 0 & 0 & 0 & mz_\mathrm{g}r & mw & -mv \\ 0 & 0 & 0 & -mw & mz_\mathrm{g}r & mu \\ 0 & 0 & 0 & -m(z_\mathrm{g}p - v) & -m(z_\mathrm{g}q + u) & 0 \\ -mz_\mathrm{g}r & mw & m(z_\mathrm{g}p - v) & 0 & I_z r & -I_y q \\ -mw & -mz_\mathrm{g}r & m(z_\mathrm{g}q + u) & -I_z r & 0 & I_x p \\ mv & -mu & 0 & I_y q & -I_x p & 0 \end{bmatrix}. \tag{5.50}$$

Assume that $\tilde{\mathbf{C}}_\mathrm{v} = \mathbf{C}_\mathrm{v}(\boldsymbol{\nu})\boldsymbol{\nu} - \mathbf{C}_\mathrm{v}(\boldsymbol{\nu}_\mathrm{m})\boldsymbol{\nu}_\mathrm{m} = [c_1, c_2, c_3, c_4, c_5, c_6]^T$, and

$$|\tilde{\mathbf{C}}_\mathrm{v}| \leq \bar{\mathbf{C}}_\mathrm{v} = [\bar{c}_1, \bar{c}_2, \bar{c}_3, \bar{c}_4, \bar{c}_5, \bar{c}_6]^T, \tag{5.51}$$

an example of the calculation of $\bar{c}_1$ is given below:

$$\begin{aligned}\tilde{c}_1 =& mz_g(r_m p_m - rp) + m(w_m q_m - wq) - m(v_m r_m - vr) && (5.52)\\ =& -mz_g((r_m-\omega_r)(p_m-\omega_p) - r_m p_m) - m((w_m-\omega_w)(q_m-\omega_q) - w_m q_m)\\ &+ m((v_m-\omega_v)(r_m-\omega_r) - v_m r_m). && (5.53)\end{aligned}$$

Thus,

$$\begin{aligned}|c_1| \le& mz_g(\bar{\omega}_r\bar{\omega}_p + \bar{\omega}_r|p_m| + \bar{\omega}_p|r_m|) + m(\bar{\omega}_w\bar{\omega}_q + \bar{\omega}_w|q_m| + \bar{\omega}_q|w_m|)\\ &+ m(\bar{\omega}_v\bar{\omega}_r + \bar{\omega}_v|r_m| + \bar{\omega}_r|v_m|) && (5.54)\\ =& \bar{c}_1. && (5.55)\end{aligned}$$

For the full Coriolis force term,

$$\begin{aligned}|\tilde{\mathbf{C}}_v| &= |\mathbf{C}_v(\boldsymbol{\nu})\boldsymbol{\nu} - \mathbf{C}_v(\boldsymbol{\nu}_m)\boldsymbol{\nu}_m| && (5.56)\\ &\le \bar{\mathbf{C}}_v(\bar{\boldsymbol{\omega}}_v, \boldsymbol{\nu}_m(t)) && (5.57)\\ &= \bar{\mathbf{C}}_{v1}(\bar{\boldsymbol{\omega}}_v) + \bar{\mathbf{C}}_{v2}(\bar{\boldsymbol{\omega}}_v)|\boldsymbol{\nu}_m(t)| && (5.58)\\ &= \begin{bmatrix} m(\bar{\omega}_w\bar{\omega}_q + \bar{\omega}_v\bar{\omega}_r + z_g\bar{\omega}_q\bar{\omega}_r)\\ m(\bar{\omega}_w\bar{\omega}_p + \bar{\omega}_u\bar{\omega}_r + z_g\bar{\omega}_p\bar{\omega}_r)\\ m(\bar{\omega}_v\bar{\omega}_p + \bar{\omega}_u\bar{\omega}_q + 2z_g\bar{\omega}_p\bar{\omega}_q)\\ (I_z+I_y)\bar{\omega}_r\bar{\omega}_q + mz_g(\bar{\omega}_u\bar{\omega}_r + \bar{\omega}_w\bar{\omega}_p)\\ (I_z+I_x)\bar{\omega}_p\bar{\omega}_r + mz_g\bar{\omega}_r\bar{\omega}_v\\ (I_x+I_y)\bar{\omega}_p\bar{\omega}_q \end{bmatrix} && (5.59)\\ &+ \begin{bmatrix} 0 & m\bar{\omega}_r & m\bar{\omega}_q & 0\\ m\bar{\omega}_r & 0 & m\bar{\omega}_p & m(\bar{\omega}_w + z_g\bar{\omega}_r)\\ m\bar{\omega}_q & m\bar{\omega}_p & 0 & m(\bar{\omega}_v + z_g\bar{\omega}_q)\\ mz_g\bar{\omega}_r & 0 & mz_g\bar{\omega}_p & mz_g\bar{\omega}_w\\ 0 & mz_g\bar{\omega}_r & 0 & (I_x+I_z)\bar{\omega}_r\\ 0 & 0 & 0 & (I_x+I_y)\bar{\omega}_q \end{bmatrix} && (5.60)\\ &\begin{bmatrix} m(\bar{\omega}_w + z_g\bar{\omega}_r) & m(\bar{\omega}_v + z_g\bar{\omega}_q)\\ 0 & m(\bar{\omega}_u + z_g\bar{\omega}_p)\\ m(\bar{\omega}_u + z_g\bar{\omega}_p) & 0\\ (I_y+I_z)\bar{\omega}_r & (I_y+I_z)\bar{\omega}_q + mz_g\bar{\omega}_u\\ 0 & (I_x+I_z)\bar{\omega}_p + mz_g\bar{\omega}_v\\ (I_x+I_y)\bar{\omega}_p & 0 \end{bmatrix}\begin{bmatrix} |u_m|\\ |v_m|\\ |w_m|\\ |p_m|\\ |q_m|\\ |r_m| \end{bmatrix}. && (5.61)\end{aligned}$$

Thus, the threshold for the nonlinear term can be expressed as:

$$\begin{aligned}\bar{\gamma}(\bar{\boldsymbol{\omega}}_2, \boldsymbol{\chi}_m) &= \begin{bmatrix} \bar{\boldsymbol{\omega}}_v + |\bar{\mathbf{R}}\boldsymbol{\nu}_m| \\ \overline{\mathbf{M}}^{-1}\bar{\mathbf{C}}_v \end{bmatrix}. && (5.62)\\ &= \begin{bmatrix} [||[\bar{\omega}_{v1}, \bar{\omega}_{v2}, \bar{\omega}_{v3}]||[1,1,1], ||[\bar{\omega}_{v4}, \bar{\omega}_{v5}, \bar{\omega}_{v6}]||[1,1,1]]^T + |\bar{\mathbf{R}}(\bar{\boldsymbol{\omega}}_\eta)\boldsymbol{\nu}_m(t)| \\ \overline{\mathbf{M}}^{-1}\bar{\mathbf{C}}_v \end{bmatrix}. && (5.63)\end{aligned}$$

Similarly, $\bar{h}(t) \in \mathbb{R}^{12}$ is the adaptive bound on $|h(\boldsymbol{\chi}, \mathbf{u}, \boldsymbol{\zeta}, \mathbf{u}_\zeta) - h(\boldsymbol{\chi}_\mathrm{m}, \mathbf{u}, \boldsymbol{\zeta}, \mathbf{u}_\zeta)|$.
For the interconnected term $\bar{h}(t)$, we have

$$\begin{aligned} |h(\boldsymbol{\chi}, \mathbf{u}, \boldsymbol{\zeta}, \mathbf{u}_\zeta) - h(\boldsymbol{\chi}_\mathrm{m}, \mathbf{u}, \boldsymbol{\zeta}, \mathbf{u}_\zeta)| &= \left| \begin{bmatrix} \mathbf{0} \\ \overline{\mathbf{M}}^{-1} \boldsymbol{\tau}_\mathrm{wires} \end{bmatrix} - \begin{bmatrix} \mathbf{0} \\ \overline{\mathbf{M}}^{-1} \hat{\boldsymbol{\tau}}_\mathrm{wires} \end{bmatrix} \right| \\ &= \begin{bmatrix} \mathbf{0} \\ \overline{\mathbf{M}}^{-1} |\tilde{\boldsymbol{\tau}}_\mathrm{wires}| \end{bmatrix} \leq \bar{h}(\bar{\boldsymbol{\omega}}_2, \boldsymbol{\chi}_\mathrm{m}), \end{aligned} \tag{5.64}$$

with

$$\hat{\boldsymbol{\tau}}_\mathrm{wires} = \begin{bmatrix} \frac{F_\mathrm{hoist}}{||\mathbf{R}_3^T(\boldsymbol{\eta}_\mathrm{m})(\boldsymbol{\eta}_\mathrm{l} - \boldsymbol{\eta}_\mathrm{3m}) - \mathbf{p}_\mathrm{ct}||} (\mathbf{R}_3^T(\boldsymbol{\eta}_\mathrm{m})(\boldsymbol{\eta}_\mathrm{l} - \boldsymbol{\eta}_\mathrm{3m}) - \mathbf{p}_\mathrm{ct}) \\ \frac{F_\mathrm{hoist}}{||\mathbf{R}_3^T(\boldsymbol{\eta}_\mathrm{m})(\boldsymbol{\eta}_\mathrm{l} - \boldsymbol{\eta}_\mathrm{3m}) - \mathbf{p}_\mathrm{ct}||} \mathbf{r}_\mathrm{ct} \times (\mathbf{R}_3^T(\boldsymbol{\eta}_\mathrm{m})(\boldsymbol{\eta}_\mathrm{l} - \boldsymbol{\eta}_\mathrm{3m}) - \mathbf{p}_\mathrm{ct}) \end{bmatrix} \tag{5.65}$$

To calculate the threshold $\bar{h}$, the threshold of $\tilde{\boldsymbol{\tau}}$ is analyzed.

$$\begin{aligned} \tilde{\boldsymbol{\tau}}_\mathrm{wires} &= \boldsymbol{\tau}_\mathrm{wires} - \hat{\boldsymbol{\tau}}_\mathrm{wires} && (5.66) \\ &= \begin{bmatrix} \frac{F_\mathrm{hoist}}{||\mathbf{R}_3^T(\boldsymbol{\Theta})(\boldsymbol{\eta}_\mathrm{l} - \boldsymbol{\eta}) - \mathbf{p}_\mathrm{ct}||} (\mathbf{R}_3^T(\boldsymbol{\Theta})(\boldsymbol{\eta}_\mathrm{l} - \boldsymbol{\eta}) - \mathbf{p}_\mathrm{ct}) \\ \frac{F_\mathrm{hoist}}{||\mathbf{R}_3^T(\boldsymbol{\Theta})(\boldsymbol{\eta}_\mathrm{l} - \boldsymbol{\eta}) - \mathbf{p}_\mathrm{ct}||} \mathbf{r}_\mathrm{ct} \times (\mathbf{R}_3^T(\boldsymbol{\Theta})(\boldsymbol{\eta}_\mathrm{l} - \boldsymbol{\eta}) - \mathbf{p}_\mathrm{ct}) \end{bmatrix} \\ &- \begin{bmatrix} \frac{F_\mathrm{hoist}}{||\mathbf{R}_3^T(\boldsymbol{\eta}_\mathrm{m})(\boldsymbol{\eta}_\mathrm{l} - \boldsymbol{\eta}_\mathrm{3m}) - \mathbf{p}_\mathrm{ct}||} (\mathbf{R}_3^T(\boldsymbol{\eta}_\mathrm{m})(\boldsymbol{\eta}_\mathrm{l} - \boldsymbol{\eta}_\mathrm{3m}) - \mathbf{p}_\mathrm{ct}) \\ \frac{F_\mathrm{hoist}}{||\mathbf{R}_3^T(\boldsymbol{\eta}_\mathrm{m})(\boldsymbol{\eta}_\mathrm{l} - \boldsymbol{\eta}_\mathrm{3m}) - \mathbf{p}_\mathrm{ct}||} \mathbf{r}_\mathrm{ct} \times (\mathbf{R}_3^T(\boldsymbol{\eta}_\mathrm{m})(\boldsymbol{\eta}_\mathrm{l} - \boldsymbol{\eta}_\mathrm{3m}) - \mathbf{p}_\mathrm{ct}) \end{bmatrix}. && (5.67) \end{aligned}$$

We have

$$\frac{\mathbf{R}_3^T(\boldsymbol{\Theta})(\boldsymbol{\eta}_\mathrm{l} - \boldsymbol{\eta}_3) - \mathbf{p}_\mathrm{ct}}{||\mathbf{R}_3^T(\boldsymbol{\Theta})(\boldsymbol{\eta}_\mathrm{l} - \boldsymbol{\eta}_3) - \mathbf{p}_\mathrm{ct}||} = \frac{\mathbf{R}_3^T(\boldsymbol{\Theta})(\boldsymbol{\eta}_\mathrm{l} - \boldsymbol{\eta}_3) - \mathbf{p}_\mathrm{ct}}{||(\boldsymbol{\eta}_\mathrm{l} - \boldsymbol{\eta}_3) - \mathbf{R}_3(\boldsymbol{\eta})\mathbf{p}_\mathrm{ct}||}. \tag{5.68}$$

The denominator in (5.68) satisfies

$$\begin{aligned} &||(\boldsymbol{\eta}_\mathrm{l} - \boldsymbol{\eta}_3) - \mathbf{R}_3(\boldsymbol{\eta})\mathbf{p}_\mathrm{ct}|| && (5.69) \\ =&||(\boldsymbol{\eta}_\mathrm{l} - \boldsymbol{\eta}_\mathrm{3m}) - \mathbf{R}_3(\boldsymbol{\eta}_\mathrm{m})\mathbf{p}_\mathrm{ct} + (\boldsymbol{\eta}_\mathrm{3m} - \boldsymbol{\eta}) + (\mathbf{R}_3(\boldsymbol{\eta}_\mathrm{m}) - \mathbf{R}_3(\boldsymbol{\eta}))\mathbf{p}_\mathrm{ct}||, \\ \geq&\big|||(\boldsymbol{\eta}_\mathrm{l} - \boldsymbol{\eta}_\mathrm{3m}) - \mathbf{R}_3(\boldsymbol{\eta}_\mathrm{m})\mathbf{p}_\mathrm{ct}|| - ||\bar{\boldsymbol{\omega}}_{3\eta}|| - ||\bar{\mathbf{R}}_3\mathbf{p}_\mathrm{ct}||\big|, && (5.70) \\ & && (5.71) \end{aligned}$$

where $\bar{\boldsymbol{\omega}}_{3\eta} = [\bar{\omega}_x, \bar{\omega}_y, \bar{\omega}_z]^T$, $\bar{\mathbf{R}}_3 \in \mathbb{R}^{3\times3}$ denotes the surge, sway, and yaw components of $\mathbf{R}(\bar{\boldsymbol{\omega}}_\eta)$.

The numerator in (5.68) satisfies

$$\begin{aligned} &|\mathbf{R}_3^T(\boldsymbol{\Theta})(\boldsymbol{\eta}_\mathrm{l} - \boldsymbol{\eta}_3) - \mathbf{p}_\mathrm{ct}| \\ =&|\mathbf{R}_3^T(\boldsymbol{\Theta}_\mathrm{m})(\boldsymbol{\eta}_\mathrm{l} - \boldsymbol{\eta}_\mathrm{3m}) - \mathbf{p}_\mathrm{ct} + (\mathbf{R}_3^T(\boldsymbol{\Theta}_\mathrm{m})\boldsymbol{\eta}_\mathrm{3m} - \mathbf{R}_3^T(\boldsymbol{\Theta})\boldsymbol{\eta}) \\ &+ (\mathbf{R}_3^T(\boldsymbol{\Theta}) - \mathbf{R}_3^T(\boldsymbol{\eta}_\mathrm{m}))\boldsymbol{\eta}_\mathrm{l}|, && (5.72) \\ \leq&|\mathbf{R}_3^T(\boldsymbol{\Theta}_\mathrm{m})(\boldsymbol{\eta}_\mathrm{l} - \boldsymbol{\eta}_\mathrm{3m}) - \mathbf{p}_\mathrm{ct}| + |\bar{\mathbf{R}}_3^T\boldsymbol{\eta}_\mathrm{l}| + ||\bar{\boldsymbol{\omega}}_{3\eta}||[1,1,1]^T + |\bar{\mathbf{R}}_3^T\boldsymbol{\eta}_\mathrm{m}|. && (5.73) \end{aligned}$$

Thus, define the term $\bar{\boldsymbol{\beta}}$. Given (5.67) to (5.73), the bound on h is calculated as

$$\bar{h} = \begin{bmatrix} \mathbf{0} \\ \overline{\mathbf{M}}^{-1} \begin{bmatrix} F_{\text{hoist}} \bar{\boldsymbol{\beta}} \\ \mathbf{r}_{ct} \times F_{\text{hoist}} \bar{\boldsymbol{\beta}} \end{bmatrix} \end{bmatrix}, \tag{5.74}$$

we have

$$\begin{aligned} \bar{\boldsymbol{\beta}} = & \frac{|\mathbf{R}_3^T(\boldsymbol{\Theta}_{\text{m}})(\boldsymbol{\eta}_{\text{l}} - \boldsymbol{\eta}_{3\text{m}}) - \mathbf{p}_{\text{ct}}| + |\bar{\mathbf{R}}_3^T \boldsymbol{\eta}_{\text{l}}| + ||\bar{\boldsymbol{\omega}}_{3\eta}||[1,1,1]^T + |\bar{\mathbf{R}}_3^T \boldsymbol{\eta}_{\text{m}}|}{\left| ||(\boldsymbol{\eta}_{\text{l}} - \boldsymbol{\eta}_{3\text{m}}) - \mathbf{R}_3(\boldsymbol{\Theta}_{\text{m}})\mathbf{p}_{\text{ct}}|| - ||\bar{\boldsymbol{\omega}}_{3\eta}|| - ||\bar{\mathbf{R}}_3 \mathbf{p}_{\text{ct}}|| \right|} \\ & - \frac{\mathbf{R}_3^T(\boldsymbol{\Theta}_{\text{m}})(\boldsymbol{\eta}_{\text{l}} - \boldsymbol{\eta}_{3\text{m}}) - \mathbf{p}_{\text{ct}}}{||\mathbf{R}_3^T(\boldsymbol{\Theta}_{\text{m}})(\boldsymbol{\eta}_{\text{l}} - \boldsymbol{\eta}_{3\text{m}}) - \mathbf{p}_{\text{ct}}||}. \end{aligned} \tag{5.75}$$

Remark 5.2. *The implemented adaptive threshold is described by* (5.21), (5.28),(5.63), (5.74), *and* (5.75). *Note that if the measurement noise is zero, then the adaptive threshold becomes:*

$$\bar{\bar{\boldsymbol{\chi}}}(t) = e^{\boldsymbol{\lambda} t} \bar{\boldsymbol{\chi}}(0) + [-\boldsymbol{\lambda}^{-1}(\mathbf{I} - e^{\boldsymbol{\lambda} t}) \bar{\boldsymbol{\omega}}_1],$$

which is a constant adaptive threshold depends on the bound of system disturbances $\bar{\boldsymbol{\omega}}_{\text{l}}$.

In the next section, we will propose a decision logic which is based on the adaptive threshold and generated residual.

5.2.3. DECISION LOGIC

The transition from mode 1 to mode 2 is detected at the first time instant

$$|\hat{\boldsymbol{\chi}}(t) - \boldsymbol{\chi}_{\text{m}}(t)| > \bar{\boldsymbol{\chi}}(t) \tag{5.76}$$

that is, if one or more elements of the vector $|\hat{\boldsymbol{\chi}}(t) - \boldsymbol{\chi}_{\text{m}}(t)|$, exceeds its corresponding bound, we infer that the construction mode has changed to free-hanging. By the design of the residual and the adaptive threshold, if

$$|\hat{\boldsymbol{\chi}}(t) - \boldsymbol{\chi}_{\text{m}}(t)| \leq \bar{\boldsymbol{\chi}}(t) \tag{5.77}$$

is satisfied for all elements in $|\hat{\boldsymbol{\chi}}(t) - \boldsymbol{\chi}_{\text{m}}(t)|$, the interconnected system is inferred to operate in mode 1. The detected switching time is defined as:

$$\begin{aligned} t_{\text{D}} &= \min\{t_{\text{D}j} : j \in 1,2,3,...,12\}, \\ t_{\text{D}j} &= \min\{t : |\hat{\boldsymbol{\chi}}(t) - \boldsymbol{\chi}_{\text{m}}(t)| > \bar{\boldsymbol{\chi}}(t)\}. \end{aligned} \tag{5.78}$$

The detection time delay is defined as:

$$\tilde{t} = t_{\text{D}} - t_{\text{s}}, \tag{5.79}$$

where t_{s} is the actual mode switching time. Note that the validity of (5.76) and (5.77) is checked automatically at every time instant.

Remark 5.3. *The proposed mode detection scheme does not depend on the characteristics of the load or the wires. The mode detection scheme shown in Figure 5.1 can be embedded as a software-based module implemented in the digital computer used for the DP of the vessel, and there is no need to change its parameters every time that the crane vessel should lift a new load. If we have followed a centralized approach treating $\Sigma^{(1)}$ and $\Sigma^{(2)}$ as one system and design an observer for the augmented system, then it would be necessary to change the design parameters of the detection system with respect to the characteristics of the load.*

Remark 5.4. *The use of adaptive threshold instead of a fixed threshold reduces the conservativeness in the decision-making process. A fixed threshold is simpler than an adaptive threshold in its real implementation as fixed thresholds require less real time computation. But its determination would require a large amount of historical data during mode 1 before using the threshold in the detection scheme.*

5.3. SIMULATION EXPERIMENTS

In this section, a nominal simulation is performed with a load of 2000 tonnes under sea state 2. Then several simulations are made under different parameter settings, under environmental loads, and with different load, in order to assess the detection delay of the system with different simulation environments.

5.3.1. SIMULATION SETTINGS

The simulations in this section are made with a significant wave height of 0.5 meter, current speed of 0.6 m/s, and a nominal wind velocity of 2.5 m/s. Details of the controller and the simulated vessel (e.g., mass matrix, damping matrix, etc.) can be found in [106]. The environmental disturbances come from 30 degrees east of south. As described in the beginning of Section 3.2, the simulated bounds on the system disturbance and measurement noise are:

$$\bar{\boldsymbol{\omega}}_1 = 0.01\begin{bmatrix} 0 & 0 & 0 & 0 & 0 & 0 & 2 & 6 & 0.1 & 0.1 & 0.01 & 0.1 \end{bmatrix}^T, \tag{5.80}$$

$$\bar{\boldsymbol{\omega}}_2 = 0.1\begin{bmatrix} 1 & 1 & 1 & 1 & 1 & 1 & \frac{\pi}{180} & \frac{\pi}{180} & \frac{\pi}{180} & \frac{\pi}{180} & \frac{\pi}{180} & \frac{\pi}{180} \end{bmatrix}^T. \tag{5.81}$$

The observer gain $\mathbf{K}$ in (5.13) has been selected as a diagonal matrix such that the eigenvalues of the matrix are:

$$\boldsymbol{\lambda} = -0.1 \times diag\{\ 1 \quad 1 \quad 1 \quad 1 \quad 1 \quad 1 \quad 0.5 \quad 4 \quad 10 \quad 10 \quad 5 \quad 3\ \}. \tag{5.82}$$

The simulation consists of three steps with switching time at $t_s = 600s$, and a total simulation time of $800s$:

- During the first 50 seconds, there's no crane load on the vessel;
- Mode 1: From 50s up to 550s, the vessel is lifting the load. Then from 550s to 600s, the hoist force equals to the maximum force needed to lift the load with the load still on the platform. In this mode, the vessel can be seen as moored to the platform via crane wires with increasing crane load;

- Mode 2: From 600s to 800s, the load is fully lifted and is free-hanging.

The hoist force during the simulation is shown in Figure 5.2.

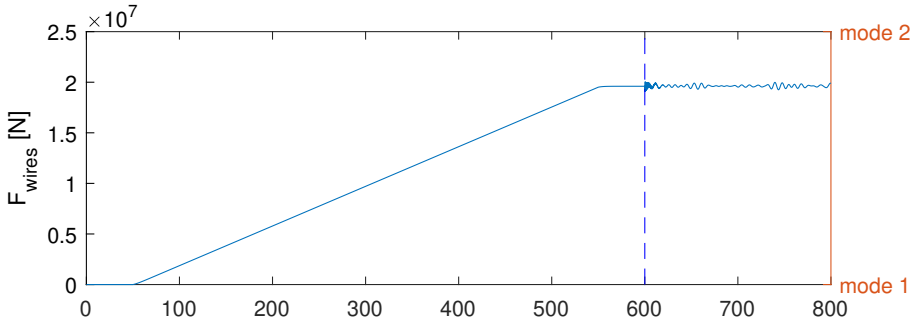

Figure 5.2: Tension in the Crane Wires (F_{hoist}) during the Simulation

The mode detection scheme is designed as shown in Section 5.3, where the nonlinear observer in (5.13) and (5.14) is structured using (5.82) and the fixed position of the load $\boldsymbol{\eta}_{\text{l}} = [-115, 0, -9.19]^T$. The adaptive thresholds are designed using (5.80) and (5.81) as the bounds on the disturbances and measurement noise respectively. The bound on the initial condition is set to

$$\bar{\boldsymbol{\chi}}(0) = 0.1 \begin{bmatrix} 1 & 1 & 1 & 1 & 1 & 1 & 1 & 1 & 1 & 1 & 1 & 1 \end{bmatrix}^T \tag{5.83}$$

5.3.2. SIMULATION RESULTS

Figure 5.3 to Figure 5.6 show the magnitude of the residual $|\boldsymbol{\chi}_{\text{m}i}(t) - \hat{\boldsymbol{\chi}}_i(t)|$ and the adaptive threshold $\bar{\boldsymbol{\chi}}_i(t)$ during the simulation. Figure 5.7 shows the actual switching time and the detected switching time. A detection time delay $\tilde{t} = 9s$ is observed in this case.

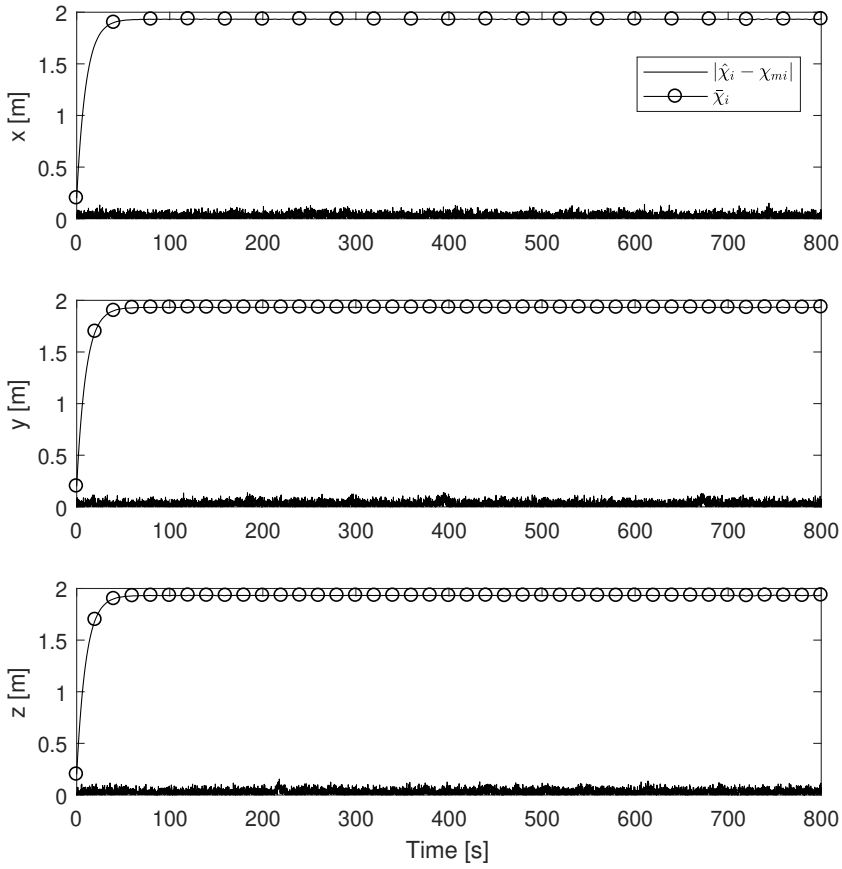

Figure 5.3: Residual ($|\hat{\chi}_i - \chi_{\mathrm{m}i}|$) and adaptive threshold ($\bar{\chi}_i$) for $i = 1, 2$, and 3

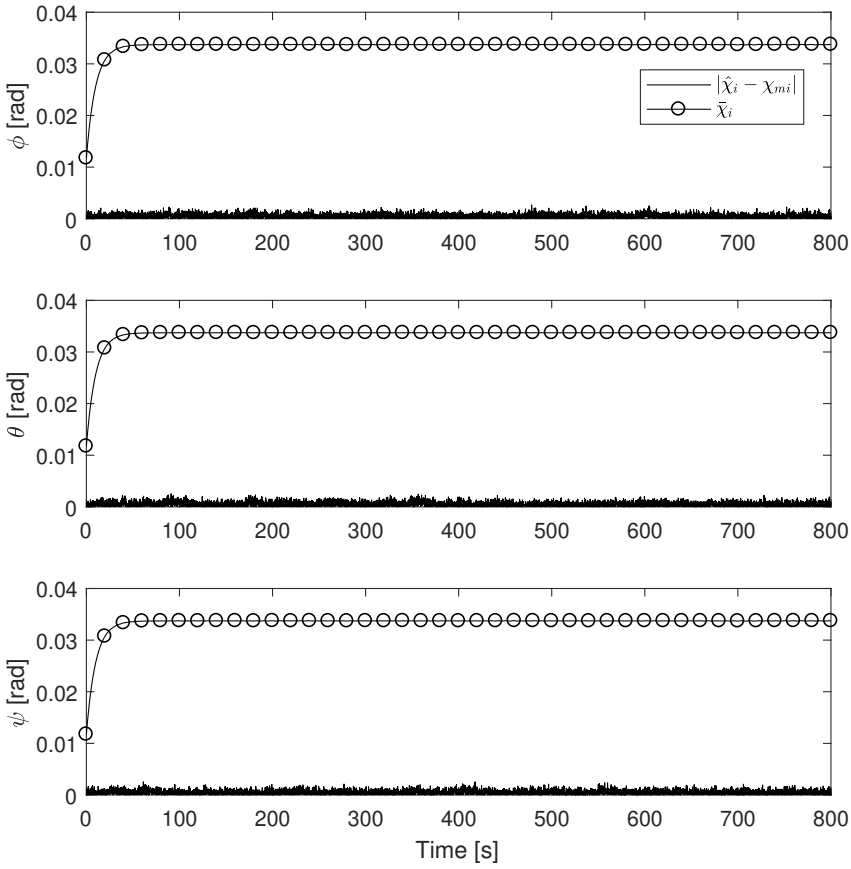

Figure 5.4: Residual ($|\hat{\chi}_i - \chi_{mi}|$) and adaptive threshold ($\bar{\chi}_i$) for $i = 4, 5$, and 6

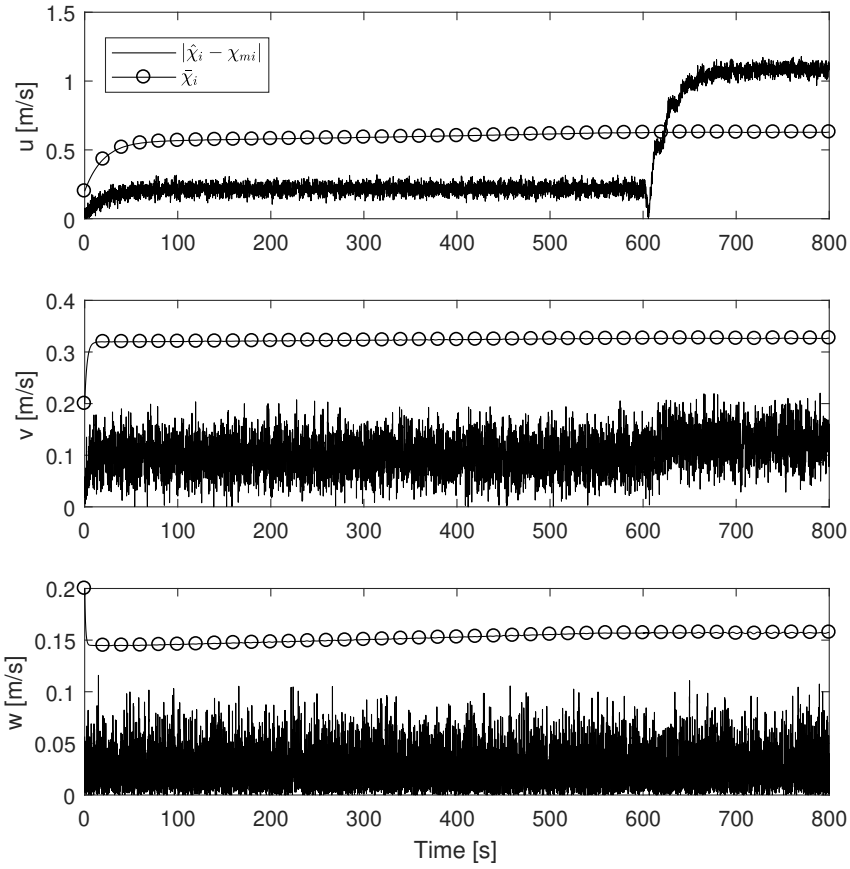

Figure 5.5: Residual ($|\hat{\chi}_i - \chi_{mi}|$) and adaptive threshold ($\bar{\chi}_i$) for $i = 7$, 8, and 9

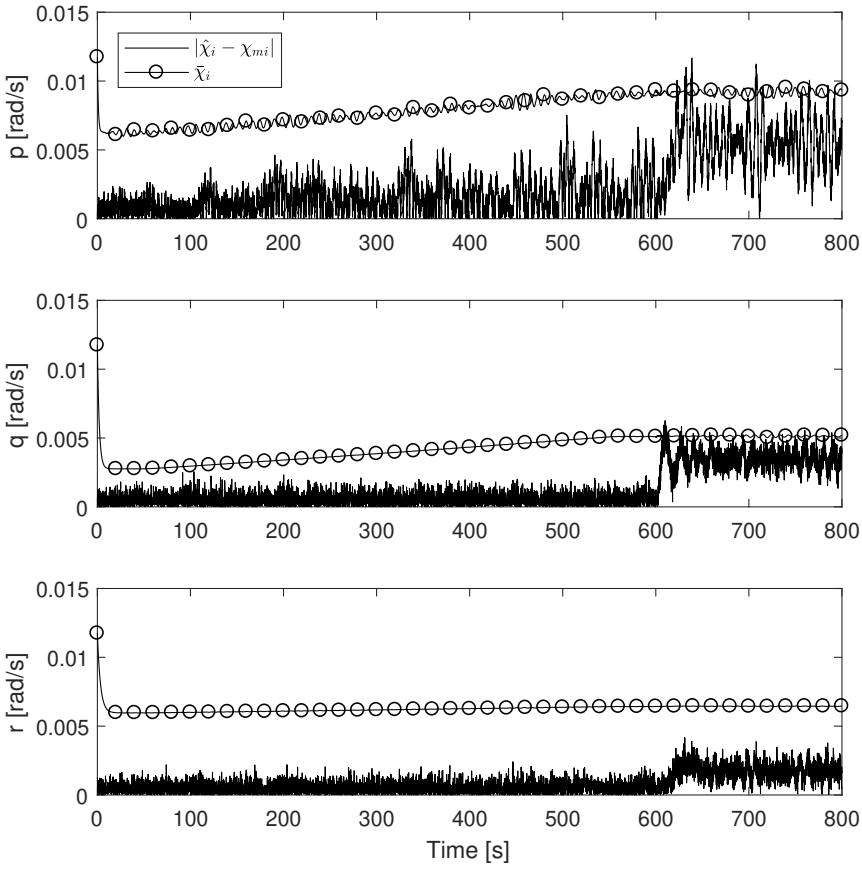

Figure 5.6: Residual ($|\hat{\chi}_i - \chi_{mi}|$) and adaptive threshold ($\bar{\chi}_i$) for $i = 10$, 11, and 12

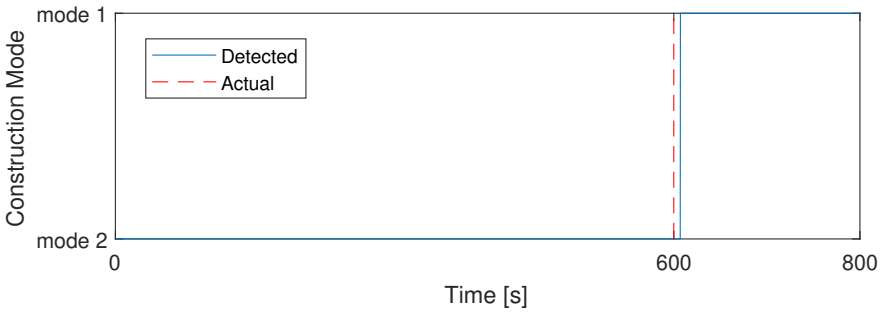

Figure 5.7: Mode switch and detected mode switch

Based on Figure 5.3 and Figure 5.4, we can observe that the first six residuals stay low during the whole simulation, and thus they are not influenced by the construction mode switching as they are only affected by the sensor noise. These residuals could be used for detecting sensor faults.

The behavior of the residual and the adaptive threshold highly depend on the disturbances $\boldsymbol{\omega}_1$, and the measurement noise $\boldsymbol{\omega}_2$ (related to the accuracy of the sensor) and the selection of the eigenvalues $\boldsymbol{\lambda}$. The proposed decision logic guarantees that there will be no false alarms, i.e. there will be no case that the detection system infers the transition to mode 2 although mode 1 is active. However, the delay between the time of detection and the time of the actual transition may be large, or we may have large delay if the bounds on the disturbances are overestimated or the design parameters of the observer are not optimized.

According to (5.21)-(5.75), the adaptive threshold mainly depends on the measurement noise bound. The sensitivity of the proposed detection system with respect to the bound of the measurement noise can be evaluated through the detection delay time. For the sensitivity analysis, we have simulated the adaptive thresholds given in (5.21)-(5.75), using an overestimated bound $\bar{\boldsymbol{\omega}}_2'$. The detection delay with respect to the ratio $\frac{\bar{\omega}_{2j}'}{\bar{\omega}_{2j}}$, $\forall\, j \in \{1, \cdots, 12\}$, where $\bar{\boldsymbol{\omega}}_2'$ denotes the overestimated upper bound for the measurement noise, and $\bar{\boldsymbol{\omega}}_2$ denotes the actual bound in (5.82). With a more conservative setting for the measurement noise, the detection time increases.

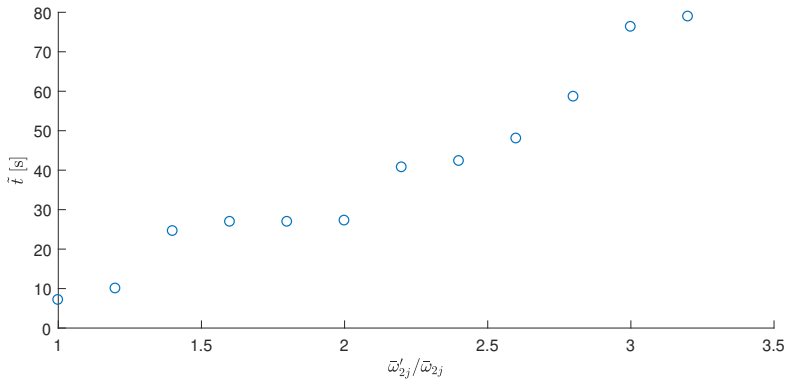

Figure 5.8: Detection time delay ($\tilde{t}$) under different measurement setting of $\bar{\boldsymbol{\omega}}_2$

As observed from Figure 5.8, the detection speed of the designed system decreases as the upper bound of the measurement noise used in the adaptive threshold calculation increases. The selection of the eigenvalues $\boldsymbol{\lambda}$ can be realized by applying optimization techniques, which are out of the scope of this work.

More simulations are made under different environmental loads and with different load weights to assess the sensitivity of the proposed detection system. The results are shown in Table 5.1 and Table 5.2. The detection system has a detection time delay of 26.9s when the load is 1600t. With higher loads, the detection time delay is shortened. For the simulations under different sea state, the detection system has a lower detection

time delay (5.5s) with no environmental loads, and the detection time delay increases with the environmental loads increase. In general, the proposed detection system has a better performance (i.e., a lower detection time) with heavier loads, and under lower sea states.

Mass of load [tonnes]	1600	1800	2000	2200	2400
Detection time delay [s]	26.9	10.8	8.9	7.6	6.5

Table 5.1: Detection time delay ($\tilde{t}$) with different load mass

Sea state	0	1	2	3	4
Detection time delay [s]	5.5	6.7	8.9	9.3	10.1

Table 5.2: Detection time delay ($\tilde{t}$) under different sea state

5.4. CONCLUSIONS

In this chapter, we answered Research *Subquestion 5: How to design a software-based system to detect the switching of the construction mode during offshore heavy lift operations?* by designing a digital mode detection system. A model-based mode detection system is proposed to detect the switching between different offshore heavy lift construction Mode 1 and Mode 2. The detection system is simulated with the physical model and simulation results show that the system could detect the switching of construction modes within 10s with a load of 2000t and under sea state 2. The sensitivity of the proposed detection system is related to the measurement noise bound and the external disturbance bound. The proposed detection system has a lower detection time delay under lower sea state and with higher mass of load. In Chapter 4 and Chapter 5 we presented a switching DP controller and a mode detection system. To achieve an automated offshore operation procedure, we still need to study the control of crane during free-hanging period to stabilize the motion of the load while the vessel is under DP control. Thus, in the next chapter, the control of crane force with free-hanging load will be introduced.

6

BACKSTEPPING CONTROL OF THE HANGING LOAD

In Chapter 4 and Chapter 5, a switching controller is proposed for DP, and a system to detect the switching of different construction modes is proposed for heavy lift vessels during offshore construction. To complete the smart control system of the heavy lift operations, a controller for the load needs to be designed to control the tension in the wires when the load is free-hanging. For most heavy lift vessels, the rotation angles of the cranes are fixed or with limited flexibility during offshore operations. Thus the load is under-actuated with only control input from the crane wires. In this chapter, we address *Subquestion 6: How to design a nonlinear control system for the under-actuated heavy load?*

The rest of this chapter is organized as follows: Section 6.1 introduces the problem formulation and the control objective. Section 6.2 introduce the controller designed for the crane force to stabilize the hanging load. Section 6.3 provides simulation results of the proposed control scheme. While conclusions are given in Section 6.4.

6.1. CONTROL OBJECTIVE

During offshore construction, the position of the heavy lift vessel is controlled by a Dynamic Positioning (DP) system, while the force in the crane wires is controlled via a crane winch. Figure 6.1 shows an illustration of the crane vessel with free-hanging load. For heavy lift vessels with hanging structures (i.e., loads), the proposed controller for the hanging load should be able to stabilize the position of the load in surge, sway, and heave position under DP control. In order to design the controller, we first study the dynamics of the load under the impact of vessel dynamic positioning.

When the load is free-hanging, the vessel and the load can be seen as connected with hoist wires. As the load's rotation has less impact on the vessel's position stability compared to the impact from its position control, the load dynamics can be simplified

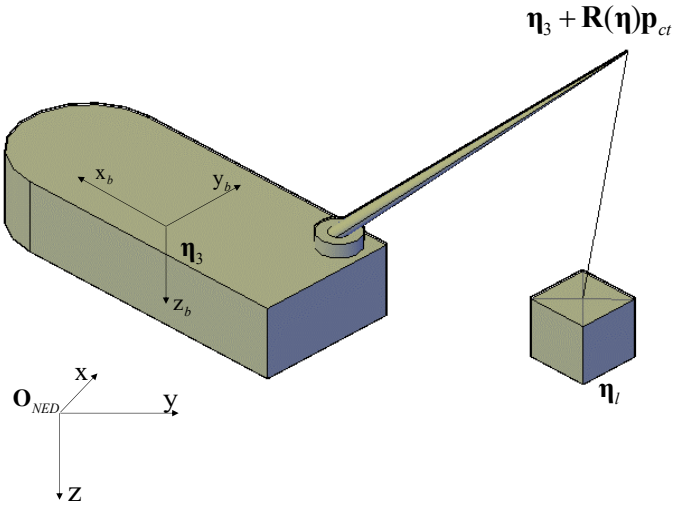

Figure 6.1: Heavy Lift Vessel with Load, where $\boldsymbol{O}_{\text{NED}}$ is the orgin of earth-fixed coordinate system, $\boldsymbol{\eta}_3$ is the vessel position in the earth-fixed coordinate system and the origin of body-fixed coordinate system, $\boldsymbol{R}^T(\boldsymbol{\Theta})$ is the transfer matrix from body-fixed coordinate system to earth-fixed coordinate system, $\boldsymbol{p}_{\text{ct}}$ is the body-fixed position of crane tip in the body-fixed coordinate system, $\boldsymbol{\eta}_{\text{l}}$ is the earth-fixed load position

to 3 DoFs (see Section 3.4.1):

$$\begin{aligned}\ddot{\boldsymbol{\eta}}_{\text{l}}(t) = &- \boldsymbol{M}_{\text{l}}^{-1}\boldsymbol{D}_{\text{l}}\dot{\boldsymbol{\eta}}_{\text{l}}(t) - \boldsymbol{M}_{\text{l}}^{-1}\boldsymbol{F}_{\text{env}}(t) - \boldsymbol{M}_{\text{l}}^{-1}\boldsymbol{g}_{\text{l}} \\ &+ \frac{F_{\text{hoist}}(t)}{||\boldsymbol{\eta}_3(t) + \boldsymbol{R}^T(\boldsymbol{\Theta}(t))\boldsymbol{p}_{\text{ct}} - \boldsymbol{\eta}_{\text{l}}(t)||} \\ &\times \boldsymbol{M}_{\text{l}}^{-1}(\boldsymbol{\eta}_3(t) + \boldsymbol{R}^T(\boldsymbol{\Theta}(t))\boldsymbol{p}_{\text{ct}} - \boldsymbol{\eta}_{\text{l}}(t)),\end{aligned} \tag{6.1}$$

where $\boldsymbol{\eta}_3(t) = [x, y, z]^T$ is the vector of the first three elements in $\boldsymbol{\eta}_{\text{v}}(t)$, and

$$\boldsymbol{R}^T(\boldsymbol{\Theta}) = \begin{bmatrix} c_\psi c_\theta & -s_\psi c_\phi + c_\psi s_\theta s_\phi & s_\psi s_\phi + c_\psi c_\phi s_\theta \\ s_\psi c_\theta & c_\psi c_\phi + s_\phi s_\theta s_\psi & -c_\psi s_\phi - s_\theta s_\psi c_\phi \\ -s_\theta & c_\theta s_\phi & c_\theta c_\phi \end{bmatrix}, \tag{6.2}$$

where s_θ and c_θ are the sine and cosine of the angle θ (similarly for the other sines and cosines in (6.2)). The last term in (6.1) represents the interconnected dynamics between the load position and the vessel movement.

The control objective of this chapter is to define required hoist force in the crane wires in order to keep the load in the desired position.

6.2. CONTROLLER DESIGN

In this section, a state-space model is designed for the hanging load, and a control scheme is proposed based on the state-space model. As the controlled object (i.e., the load) is nonlinear and underactuated, the approach is fulfilled by backstepping and command filtering.

6.2.1. STATE-SPACE MODELLING

If we assume that there is no external disturbance on the load except for the crane tension, we can rewrite (6.1) in the following state-space form:

$$\dot{\boldsymbol{\chi}}_1(t) = \varepsilon(\boldsymbol{\eta}(t)) - \boldsymbol{\chi}_2(t), \tag{6.3}$$

$$\dot{\boldsymbol{\chi}}_2(t) = f_0(\boldsymbol{\chi}_2(t)) + g_0(\boldsymbol{\chi}_1(t))u(t), \tag{6.4}$$

where $\boldsymbol{\chi}_1$ represents the vector of the crane wires (load to cranetip) in earth-fixed coordinate system, with the following representation:

$$\boldsymbol{\chi}_1(t) = \boldsymbol{\eta}_3(t) - \boldsymbol{\eta}_1(t) + \boldsymbol{R}^T(\boldsymbol{\Theta}(t))\boldsymbol{p}_{\text{ct}}, \tag{6.5}$$

$$\boldsymbol{\chi}_2(t) = \dot{\boldsymbol{\eta}}_1(t), \tag{6.6}$$

$$\varepsilon(\boldsymbol{\eta}(t)) = \frac{d}{dt}(\boldsymbol{\eta}_3(t) + \boldsymbol{R}^T(\boldsymbol{\Theta}(t))\boldsymbol{p}_{\text{ct}}) = \boldsymbol{R}^T(\boldsymbol{\Theta})\boldsymbol{\nu}_3(t) + \frac{\partial}{\partial t}\boldsymbol{R}^T(\boldsymbol{\Theta})\boldsymbol{p}_{\text{ct}}) \tag{6.7}$$

$$f_0(\boldsymbol{\chi}_2(t)) = -\boldsymbol{M}_1^{-1}\boldsymbol{D}_1\boldsymbol{\chi}_2(t) - \boldsymbol{M}_1^{-1}\boldsymbol{g}_1, \tag{6.8}$$

$$g_0(\boldsymbol{\chi}_1(t)) = \boldsymbol{M}_1^{-1}\frac{\boldsymbol{\chi}_1(t)}{||\boldsymbol{\chi}_1(t)||}, \tag{6.9}$$

$$u(t) = F_{\text{hoist}}(t), \tag{6.10}$$

where $\boldsymbol{\nu}_3(t) \in \mathbb{R}^3$ denotes the velocity of the vessel.

Let us define

$$\frac{\partial}{\partial t}\boldsymbol{R}^T(\boldsymbol{\Theta}) = \begin{bmatrix} R_{d11} & R_{d12} & R_{d13} \\ R_{d21} & R_{d22} & R_{d23} \\ R_{d31} & R_{d32} & R_{d33} \end{bmatrix}. \tag{6.11}$$

Then we have

$$R_{d11} = -c_\psi s_\theta \dot{\theta} - s_\psi c_\theta \dot{\psi}, \tag{6.12}$$

$$R_{d12} = (s_\psi s_\phi + c_\psi s_\theta c_\phi)\dot{\phi} + c_\psi c_\theta s_\phi \dot{\theta} + (-c_\psi c_\phi - s_\psi s_\theta s_\phi)\dot{\psi}, \tag{6.13}$$

$$R_{d13} = (s_\psi c_\phi - c_\psi s_\phi s_\theta)\dot{\phi} + c_\psi c_\phi c_\theta \dot{\theta} + (s_\phi c_\psi - s_\psi c_\phi s_\theta)\dot{\psi}, \tag{6.14}$$

$$R_{d21} = -s_\psi s_\theta \dot{\theta} + c_\psi c_\theta \dot{\psi}, \tag{6.15}$$

$$R_{d22} = (-c_\psi s_\phi + c_\phi s_\theta s_\psi)\dot{\phi} + s_\phi c_\theta s_\psi \dot{\theta} + (-s_\psi c_\phi + s_\phi s_\theta c_\psi)\dot{\psi}, \tag{6.16}$$

$$R_{d23} = (-c_\psi c_\phi + s_\theta s_\psi s_\phi)\dot{\phi} - c_\theta s_\psi c_\phi \dot{\theta} + (s_\psi s_\phi - s_\theta c_\psi c_\phi)\dot{\psi}, \tag{6.17}$$

$$R_{d31} = -c_\theta \dot{\theta}, \tag{6.18}$$

$$R_{d32} = c_\theta c_\phi \dot{\phi} - c_\theta s_\phi \dot{\theta}, \tag{6.19}$$

$$R_{d33} = -c_\theta s_\phi \dot{\phi} - s_\theta c_\phi \dot{\theta}, \tag{6.20}$$

where $\dot{\phi}, \dot{\theta}, \dot{\psi}$ can be obtained by measurements.

The system described by (6.3) and (6.4) is an under-actuated system which is not feedback linearizable, thus a reduced model with 2 DoFs is defined. Let us therefore define states ζ_1 and ζ_2,

$$\zeta_1(t) = ||\boldsymbol{\chi}_1(t)||, \tag{6.21}$$

$$\zeta_2(t) = -\frac{\boldsymbol{\chi}_1(t)^T \boldsymbol{\chi}_2(t)}{||\boldsymbol{\chi}_1(t)||}, \tag{6.22}$$

where $\zeta_1 > 0$ represents the time-varying length of the hoist wires. Based on (6.21) and (6.22), the state-space model becomes:

$$\dot{\zeta}_1(t) = \zeta_2(t) + f_1(\boldsymbol{\chi}_1(t), \boldsymbol{\eta}_3(t)), \tag{6.23}$$

$$\dot{\zeta}_2(t) = f_2(\boldsymbol{\chi}_1(t), \boldsymbol{\chi}_2(t)) - \frac{u(t)}{M_\mathrm{l}}, \tag{6.24}$$

where

$$f_1 = \frac{\boldsymbol{\chi}_1^T}{||\boldsymbol{\chi}_1||}\varepsilon(\boldsymbol{\eta}), \tag{6.25}$$

$$f_2 = \frac{\boldsymbol{\chi}_1^T \boldsymbol{M}_\mathrm{l}^{-1} \boldsymbol{D}_\mathrm{l} \boldsymbol{\chi}_2 + \boldsymbol{\chi}_1^T \boldsymbol{M}_l^{-1} \boldsymbol{g}}{||\boldsymbol{\chi}_1||} \tag{6.26}$$

$$+ \left(\frac{\boldsymbol{\chi}_2^T}{||\boldsymbol{\chi}_2||} - \frac{\boldsymbol{\chi}_1^T \boldsymbol{\chi}_2 \boldsymbol{\chi}_1^T}{||\boldsymbol{\chi}_1||^3}\right)(\varepsilon(\boldsymbol{\eta}) - \boldsymbol{\chi}_2). \tag{6.27}$$

6.2.2. BACKSTEPPING CONTROL DESIGN

The backstepping control for the system (6.23)-(6.24) is based on the approach presented in [28]. Suppose that (6.23) can be stabilized by a state feedback control law $\zeta_2 = \zeta_{2\mathrm{d}}$; we define $\tilde{\zeta}_1 = \zeta_1 - \zeta_{1\mathrm{d}}$, where

$$\begin{aligned}\zeta_{1\mathrm{d}}(t) &= ||\boldsymbol{\chi}_{1\mathrm{d}}(t)|| \\ &= ||\boldsymbol{\eta}_3(t) - \boldsymbol{\eta}_{\mathrm{ld}} + \boldsymbol{R}^T(\boldsymbol{\Theta}(t))\boldsymbol{p}_{\mathrm{ct}}||\end{aligned} \tag{6.28}$$

is the desired signal for ζ_1. Hence $\boldsymbol{\chi}_{1\mathrm{d}}$ is the tracking signal for $\boldsymbol{\chi}_1$, and $\boldsymbol{\eta}_{\mathrm{ld}}$ is the desired position of the load. Initially, we find a control signal $\zeta_{2\mathrm{d}}$ to solve the tracking control problem for the system

$$\dot{\zeta}_1 = \zeta_{2\mathrm{d}} + f_1. \tag{6.29}$$

If we select

$$\zeta_{2\mathrm{d}} = \dot{\zeta}_{1\mathrm{d}} - k_1\tilde{\zeta}_1 - f_1, \tag{6.30}$$

where $k_1 > 0$ is the control gain, then the controlled ζ_1 dynamics are

$$\dot{\tilde{\zeta}}_1 = -k_1\tilde{\zeta}_1. \tag{6.31}$$

The time derivative of $V_1 = \frac{1}{2}\tilde{\zeta}_1^2$ satisfies

$$\begin{aligned}\dot{V}_1 &= -\tilde{\zeta}_1\dot{\tilde{\zeta}}_1 \\ &= -k_1\tilde{\zeta}_1^2 \leq 0.\end{aligned} \tag{6.32}$$

Consider now the second order system described by (6.23) and (6.24) and define $\tilde{\zeta}_2 = \zeta_2 - \zeta_{2\mathrm{d}}$. Then the error dynamics are

$$\begin{aligned}\dot{\tilde{\zeta}}_1 &= \zeta_{2\mathrm{d}} + f_1 + \tilde{\zeta}_2 - \dot{\zeta}_{1\mathrm{d}}, \\ \dot{\tilde{\zeta}}_2 &= f_2 - \frac{u}{M_\mathrm{l}} - \dot{\zeta}_{2\mathrm{d}},\end{aligned} \tag{6.33}$$

where

$$\begin{aligned}\dot{\zeta}_{1\mathrm{d}} &= \frac{\partial}{\partial t}||\boldsymbol{\chi}_1|| = \frac{\partial||\boldsymbol{\chi}_1||}{\partial\boldsymbol{\chi}_1}\dot{\boldsymbol{\chi}}_1 = \frac{\boldsymbol{\chi}_1^T\dot{\boldsymbol{\chi}}_1}{||\boldsymbol{\chi}_1||} \\ &= \frac{\boldsymbol{\chi}_1^T(\boldsymbol{R}^T(\boldsymbol{\Theta})\boldsymbol{\nu}_3 - \boldsymbol{\nu}_l + \frac{\partial}{\partial t}\boldsymbol{R}^T(\boldsymbol{\Theta})\boldsymbol{p}_{\mathrm{ct}})}{||\boldsymbol{\chi}_1||},\end{aligned} \tag{6.34}$$

with $\boldsymbol{\nu}_l \in \mathbb{R}^3$ representing the velocity of the hanging load.

By applying Lemma 5.3.1 in [28], the control signal for the second order system will be

$$u = m(f_2 + k_2\tilde{\zeta}_2 - \dot{\zeta}_{2\mathrm{d}} + \tilde{\zeta}_1), \tag{6.35}$$

where $k_2 > 0$.

Fot the second order tracking error dynamics, the Lyapunov function is

$$V_2 = V_1 + \frac{1}{2}\tilde{\zeta}_2^2, \tag{6.36}$$

which satisfies

$$\begin{aligned}\dot{V}_2 &= \frac{\partial V_2}{\partial\tilde{\zeta}_1}\dot{\tilde{\zeta}}_1 + \frac{\partial V_2}{\partial\tilde{\zeta}_2}\dot{\tilde{\zeta}}_2, \\ &= \tilde{\zeta}_1\dot{\tilde{\zeta}}_1 + \tilde{\zeta}_2\dot{\tilde{\zeta}}_2 \\ &= \tilde{\zeta}_1(\zeta_{2\mathrm{d}} + f_1 + \tilde{\zeta}_2 - \dot{\zeta}_{1\mathrm{d}}) + \tilde{\zeta}_2(f_2 - \frac{u}{m} - \dot{\zeta}_{2\mathrm{d}}) \\ &= -k_1\tilde{\zeta}_1^2 - k_2\tilde{\zeta}_2^2 \leq 0,\end{aligned} \tag{6.37}$$

6.2.3. COMMAND FILTERING

A command filter is designed to obtain $\zeta_{2\mathrm{d}}$ and $\dot{\zeta}_{2\mathrm{d}}$. First we consider the following structures

$$\zeta_{2\mathrm{d}}^o = \dot{\zeta}_{1\mathrm{d}} - k_1\tilde{\zeta}_1 - f_1 - \xi_2, \tag{6.38}$$

$$\dot{\xi}_1 = -k_1\xi_1 + (\zeta_{2\mathrm{d}} - \zeta_{2\mathrm{d}}^o), \tag{6.39}$$

$$u_c^o = -m(-k_2\tilde{\zeta}_2 + \dot{\zeta}_{2\mathrm{d}} - f_2 - (\tilde{\zeta}_1 - \xi_1)), \tag{6.40}$$

$$\dot{\xi}_2 = -k_2\xi_2 - \frac{1}{m}(u - u^o), \tag{6.41}$$

where ξ_1 and ξ_2 are two bounded outputs of linear stable filters with bounded inputs, the command signal $\zeta_{2\mathrm{d}}^o$ is filtered to obtain $\zeta_{2\mathrm{d}}$. With $\bar{\zeta}_i = \tilde{\zeta}_i - \xi_i, i = 1,2$, we have

$$\begin{aligned}
\dot{\tilde{\zeta}}_1 &= f_1 + \zeta_2 - \dot{\zeta}_{1\mathrm{d}} \\
&= f_1 + \zeta_{2\mathrm{d}}^o - \dot{\zeta}_{1\mathrm{d}} + (\zeta_{2\mathrm{d}} - \zeta_{2\mathrm{d}}^o) + (\zeta_2 - \zeta_{2\mathrm{d}}) \\
&= f_1 + (\dot{\zeta}_{1\mathrm{d}} - k_1\tilde{\zeta}_1 - f_1 - \xi_2) - \dot{\zeta}_{1\mathrm{d}} \\
&+ (\zeta_{2\mathrm{d}} - \zeta_{2\mathrm{d}}^o) + (\zeta_2 - \zeta_{2\mathrm{d}}) \\
&= -k_1\tilde{\zeta}_1 + \bar{\zeta}_2 + (\zeta_{2\mathrm{d}} - \zeta_{2\mathrm{d}}^o), \qquad (6.42) \\
\dot{\tilde{\zeta}}_2 &= f_2 - \frac{1}{m}(u - u^o) - \frac{1}{m}u^o - \dot{\zeta}_{2\mathrm{d}} \\
&= -k_2\tilde{\zeta}_2 - \frac{1}{m}(u - u^o) - \bar{\zeta}_1. \qquad (6.43)
\end{aligned}$$

Based on (6.39)-(6.43), we have

$$\begin{aligned}
\dot{\bar{\zeta}}_1 &= \dot{\tilde{\zeta}}_1 - \dot{\xi}_1 \\
&= -k_1\bar{\zeta}_1 + \bar{\zeta}_2, \qquad (6.44) \\
\dot{\bar{\zeta}}_2 &= \dot{\tilde{\zeta}}_2 - \dot{\xi}_2 \\
&= -k_2\bar{\zeta}_2 - \bar{\zeta}_1. \qquad (6.45)
\end{aligned}$$

Consider the following Lyapunov function

$$V_3 = \frac{1}{F}2\bar{\zeta}_1^2 + \frac{1}{2}\bar{\zeta}_2^2, \qquad (6.46)$$

Then $\dot{V}_3 = -k_1\bar{\zeta}_1^2 - k_2\bar{\zeta}_2^2 \le 0$. The origin of $(\bar{\zeta}_1, \bar{\zeta}_2)$ is exponentially stable.

In order to obtain a stable system, the command filtering is chosen with the following structure:

$$\dot{\boldsymbol{\sigma}}(t) = \begin{bmatrix} 0 & 1 \\ -a_0 & -a_1 \end{bmatrix}\boldsymbol{\sigma}(t) + \begin{bmatrix} 0 \\ a_0 \end{bmatrix}\zeta_{2\mathrm{d}}^o, \qquad (6.47)$$

$$\begin{bmatrix} \zeta_{2\mathrm{d}} \\ \dot{\zeta}_{2\mathrm{d}} \end{bmatrix} = \boldsymbol{I}_{2\times 2}\boldsymbol{\sigma}(t), \qquad (6.48)$$

where

$$s^2 + a_1 s + a_0 = 0 \qquad (6.49)$$

is a stable Hurwitz polynomial.

Remark 6.1. *In this manuscript, we assume that the position of the vessel $\boldsymbol{p}^n$, the rotation angle $\boldsymbol{\Theta}$, the position of the load $\boldsymbol{p}_1^n$, and the hoist force F_{hoist} can be obtained by measurements. The terms $\dot{\phi}, \dot{\theta}, \dot{\psi}$ can be obtained from*

$$\begin{bmatrix} \dot{\phi} \\ \dot{\theta} \\ \dot{\psi} \end{bmatrix} = \begin{bmatrix} 1 & s_\phi t_\theta & c_\phi t_\theta \\ 0 & c_\phi & -s_\phi \\ 0 & s_\phi / c_\theta & c_\phi / c_\theta \end{bmatrix} \begin{bmatrix} p \\ q \\ r \end{bmatrix}, \qquad (6.50)$$

where p, q, and r represent the measurements of the angular rate of roll, pitch, and yaw of the vessel respectively.

Remark 6.2. *The constant setpoint of the load position $\boldsymbol{p}^{\mathrm{n}}_{\mathrm{l}d}$ together with the DP system guarantee that the load is staying at the desired position. According to* (6.5) *and* (6.21)*, the setpoint of ζ_{1d} is a function of $\boldsymbol{\eta}_{\mathrm{l}d}$, $\boldsymbol{\eta}_3(t)$, and $\boldsymbol{\Theta}(t)$, and is time-varying due to the changing of $\boldsymbol{p}^{\mathrm{n}}(t)$ and $\boldsymbol{\Theta}(t)$. This time-varying value of ζ_{1d} impacts the load position generated from the movement of the vessel.*

6.3. SIMULATION RESULTS

In this section, The proposed load controller is assessed by several simulations under construction Mode 2. First we introduce the simulation settings, then the results are given in figures and tables.

6.3.1. SIMULATION SETTINGS

A nominal simulation with a load of 1000t is made. Then the proposed controller is simulated with different loads, and under different environmental loads with a load of 2000t.

In this section, we present simulation results of the application of the designed control scheme to system (1). The vessel position is controlled by the robust DP controller presented in Chapter 4. Throughout the simulations, the error of the DP system is bounded and is less than 0.1. During the simulation, the load is set to 1000 tonnes. The desired load position is set to $\boldsymbol{\eta}_{\mathrm{ld}} = [115, 0, -9.17]$, and the control parameters are chosen to fulfill the stability requirements. The parameters are chosen as

$$k_1 = 3, \tag{6.51}$$
$$k_2 = 3, \tag{6.52}$$
$$a_0 = 0.03, \tag{6.53}$$
$$a_1 = 0.2. \tag{6.54}$$

6.3.2. SIMULATION RESULTS

Simulation results are shown in Figure 6.2 and Figure 6.3. These figures show that the position of the load is stabilized with, with $\tilde{\zeta}_1$ and $\tilde{\zeta}_2$ approach zero gradually. However, the high DoFs of the load model is simplified to a lower-DoF model, which implies that the controlled position of the load might have small errors comparing to the desired position due to the reduced DoFs. This can be improved by further investigation of the setpoint of the heavy lift vessel's DP system.

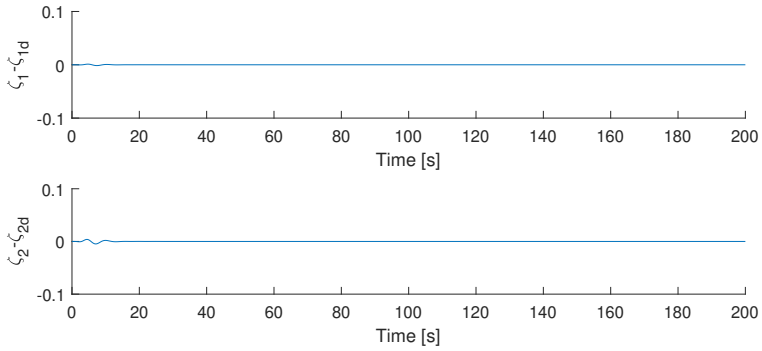

Figure 6.2: $\tilde{\zeta}_1$ and $\tilde{\zeta}_2$ in first ten seconds with m=1000t

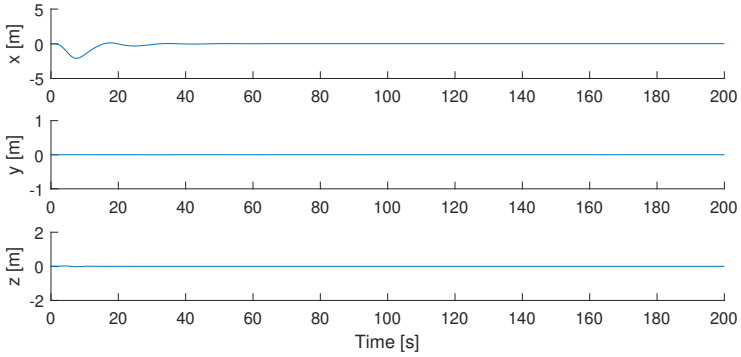

Figure 6.3: $\boldsymbol{\eta}_l - \boldsymbol{\eta}_{ld}$ with m=1000t

Additional simulations are made to test the control system with a lower load (500 tonnes), and a higher load (2000 tonnes). Results are shown in Figure 6.4. Simulations with different loads show that the performance of the controller is improved with the load decreases. Figure 6.6 shows the control input of the three simulations. After 20 seconds, the control input is stable.

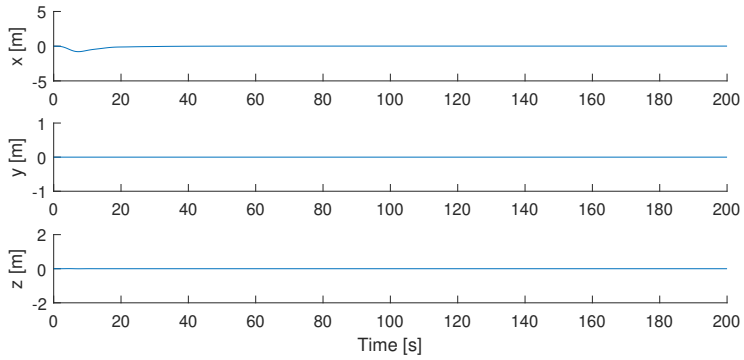

Figure 6.4: Load Position Error with m=500t

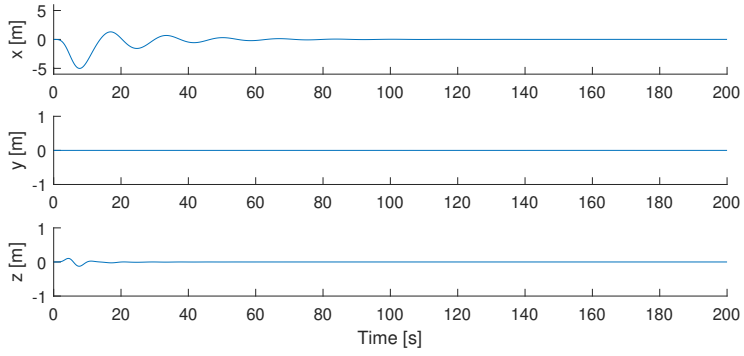

Figure 6.5: Load Position Error with m=2000t

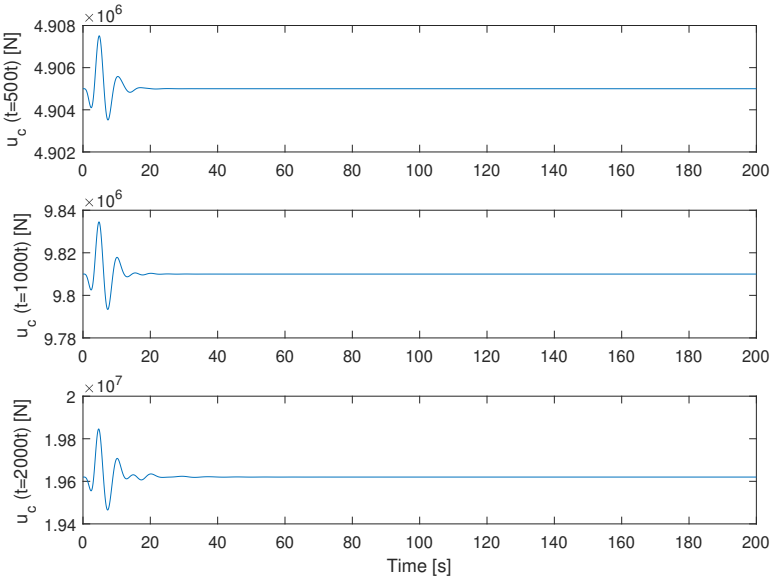

Figure 6.6: Control Input of three simulations

Simulation results in this section (i.e. Figure 6.2 to Figure 6.6) show that the position of the highly underactuated hanging load with only tension in the wires can be controlled and stabilized by applying backstepping and command filtering.

More simulations are made under different environmental loads and with different load weights. The results are shown in Table 6.1 and Table 6.2. Simulation results show that with no environmental load, the proposed controller has a lowest position error (i.e., 0.03m in North, 0.00m in East and Down) and lowest RMSE (i.e., 0.01m in North and East, 0.00m in Down). The increasing of environmental loads has a negative impact on the controller performance. This is because environmental loads are not taken into consideration in the design process of the load controller. Although the controller has a worse performance with high sea state, the RMSE and the position error are still low (i.e., within 0.4m for RMSE, and within 0.25m for position error). Simulation results with different loads show that when the environmental loads stay the same, the weight of the load has very little impact on the performance of the controller. When the simulations are under sea state 2, and the loads are increased from 1600t to 2400t, the RMSEs of the load position stay around 0.05m, 0.29m, and 0.01m in North, East, and Down respectively, while the position errors stay around 0.1m, 0.1m, and 0.3m respectively.

Sea state		0	1	2	3	4
RMSE	North [m]	0.01	0.02	0.04	0.07	0.13
	East [m]	0.00	0.03	0.09	0.11	0.14
	Down [m]	0.00	0.00	0.00	0.00	0.00
Maximum Position Error	North [m]	0.03	0.03	0.11	0.16	0.32
	East [m]	0.00	0.03	0.10	0.14	0.24
	Down [m]	0.00	0.00	0.00	0.00	0.00

Table 6.1: Simulation results (100s-200s) of the load controller under different environmental disturbances (with a load of 2000t)

Load [tonnes]		1600	1800	2000	2200	2400
RMSE	North [m]	0.05	0.05	0.04	0.05	0.04
	East [m]	0.08	0.08	0.09	0.09	0.09
	Down [m]	0.00	0.00	0.00	0.00	0.00
Maximum Position Error	North [m]	0.12	0.13	0.11	0.12	0.10
	East [m]	0.12	0.11	0.10	0.12	0.11
	Down [m]	0.00	0.00	0.00	0.00	0.00

Table 6.2: Simulation results (100s-200s) of the load controller with different loads under sea state 2

6.4. CONCLUSIONS

In this chapter, we addressed *Subquestion 6: How to design a nonlinear control system for the under-actuated heavy load?* by proposing a nonlinear load controller for heavy lift operations. The controller design was based on the three degrees-of-freedom dynamic model of the load motion, where the effects of the vessel's dynamic positioning system were taken into account. Since the crane-load system is under-actuated, a reduced model was derived and a backstepping controller is designed. We also used command filters to avoid the differentiation of virtual control signals in the backstepping scheme. The proposed control scheme makes it possible to control and stabilize hanging offshore load with large mass with a position error of less than 0.1m with no environmental loads, and with limited crane maneuverability, while the offshore heavy lift vessel is under DP control. The performance of the proposed controller decreases with the environmental loads increase. Nevertheless, the controller is able to maintain the position of the load in sea state 4 with a position error of less than 0.5m. In the next chapter, we will provide an automatic system for heavy lift operation by integrating the systems provided in Chapter 4, Chapter 5, and Chapter 6.

7

SYSTEM INTEGRATION FOR SMART OFFSHORE HEAVY LIFTING

THE robust switching DP control system, the mode detection system, and the load controller are designed in Chapter 4, Chapter 5, and Chapter 6. Simulations in the previous chapters show that each designed smart system functions well separately. However, whether these systems can work together or not remains a question. In this section, we will focus on *Subquestion 7: How to integrate the designed systems into a smart offshore operation system?*

This chapter is organized as follows: In Section 7.1, the structure of the integrated system is introduced. In Section 7.2, the algorithm of the integrated system is given. In Section 7.3, simulations are made with the integrated smart system. In Section 7.4, conclusions are reached for the integration of the intelligent control system.

7.1. STRUCTURE OF THE INTEGRATED SMART SYSTEM

The intelligence of offshore heavy lifting operations can be achieved by integrating the observer-based robust switching control system, the mode detection system, and the load control system to guarantee the safety and stability of these operations. The controllers operate according to Table 7.1.

	Mode 1 Fixed Load	Mode 2 Free-hanging Load
DP	✓	✓
Load controller		✓

Table 7.1: The function of the controllers during heavy lift operations

The observer-based robust switching controller is designed in Chapter 4 for the DP system to maintain the position of the vessel. The parameters are switched according

to different construction modes to ensure vessel's stability during the offshore heavy lift operations.

The mode detection system is designed in Chapter 5 to capture the change in the current construction mode. The switching of the DP control system and the initialization of the load controller are adjusted by the detection system. This monitoring system enhances the intelligence of the integrated system.

A load controller is designed in Chapter 6 to control the movement of the free-hanging load via the hoist force. The controller is designed for load under impact from the DP control system. When the monitoring system detects that the vessel-load system is in Mode 2, the controller starts functioning to stabilize the free-hanging load.

During the offshore heavy lift operations, the DP control system is first set to the Mode 1, and the load control is turned off. During construction mode 1, the detection system is initialized with an output of 0, the winch control follows a steadily increasing tourque to lift the load from the platform, while the DP system controls the position of the crane vessel. When the load is lifted, and is free-hanging in the air, the mode detection system detects the mode change and sends its binary decision to switch the DP system and to activate the load controller. The whole high-level control process does not require human input and is thus smart.

7.2. SYSTEM INTEGRATION

The overall structure of the digital control system is shown in Figure 7.1, with the designed smart system acting as a high level control system without human input.

We assume that required measurements for the integrated system can be obtained by sensors (e.g., GPS, IMU, etc.) and sensor fusion (i.e.,combining of sensory data or data derived from disparate sources). Then we have an integrated system as follows:

The detection system give the detected mode change time t_{D}, defined as

$$\begin{aligned} t_{\mathrm{D}} &= \min\{t_{\mathrm{D}j} : j \in 1,2,3,...,12\}, \\ t_{\mathrm{D}j} &= \min\{t : |\hat{\boldsymbol{\chi}}(t) - \boldsymbol{\chi}_{\mathrm{m}}(t)| > \bar{\bar{\boldsymbol{\chi}}}(\boldsymbol{\chi}_{\mathrm{m}}(t), \boldsymbol{\tau}_{\sigma}(t))\}, \end{aligned} \tag{7.1}$$

where $\hat{\boldsymbol{\chi}}$ is the estimation of $\boldsymbol{\chi}$, $\boldsymbol{\chi}_{\mathrm{m}}$ represents the measurement of $\boldsymbol{\chi}$, and $\bar{\bar{\boldsymbol{\chi}}}$ is the adaptive threshold. The estimated signal $\hat{\boldsymbol{\chi}}$ is obtained using the following observer:

$$\dot{\hat{\boldsymbol{\chi}}} = \mathbf{A}_1\hat{\boldsymbol{\chi}}_1 + \gamma(\boldsymbol{\chi}_{\mathrm{m}}, \mathbf{u}) + h(\boldsymbol{\chi}_{\mathrm{m}}, \mathbf{u}, \boldsymbol{\zeta}, \mathbf{u}_{\zeta}) + \mathbf{K}(\boldsymbol{\chi}_{\mathrm{m}} - \hat{\boldsymbol{\chi}}), \tag{7.2}$$

$$\boldsymbol{\zeta} = \boldsymbol{\eta}_1 = \boldsymbol{\eta}_1^{\circ}, \tag{7.3}$$

where

$$\boldsymbol{\chi} = \begin{bmatrix} \boldsymbol{\eta}_{\mathrm{v}}(t) \\ \boldsymbol{\nu}_{\mathrm{v}}(t) \end{bmatrix}. \tag{7.4}$$

The adaptive threshold is defined as:

$$|\boldsymbol{\chi}_{\mathrm{m}}(t) - \hat{\boldsymbol{\chi}}(t)| \leq |\tilde{\boldsymbol{\chi}}(t)| + \bar{\boldsymbol{\omega}}_2(t) \leq \bar{\boldsymbol{\chi}}(t) + \bar{\boldsymbol{\omega}}_2(t) \triangleq \bar{\bar{\boldsymbol{\chi}}}(t), \tag{7.5}$$

with

$$\tilde{\boldsymbol{\chi}}(t) = e^{\boldsymbol{\lambda} t}\tilde{\boldsymbol{\chi}}(0) + [-\boldsymbol{\lambda}^{-1}(\mathbf{I} - e^{\boldsymbol{\lambda} t})(\bar{\boldsymbol{\omega}}_1 + |\mathbf{K}|\bar{\boldsymbol{\omega}}_2)] + \mathbf{H}(s)(\bar{\gamma}(t) + \bar{h}(t)), \tag{7.6}$$

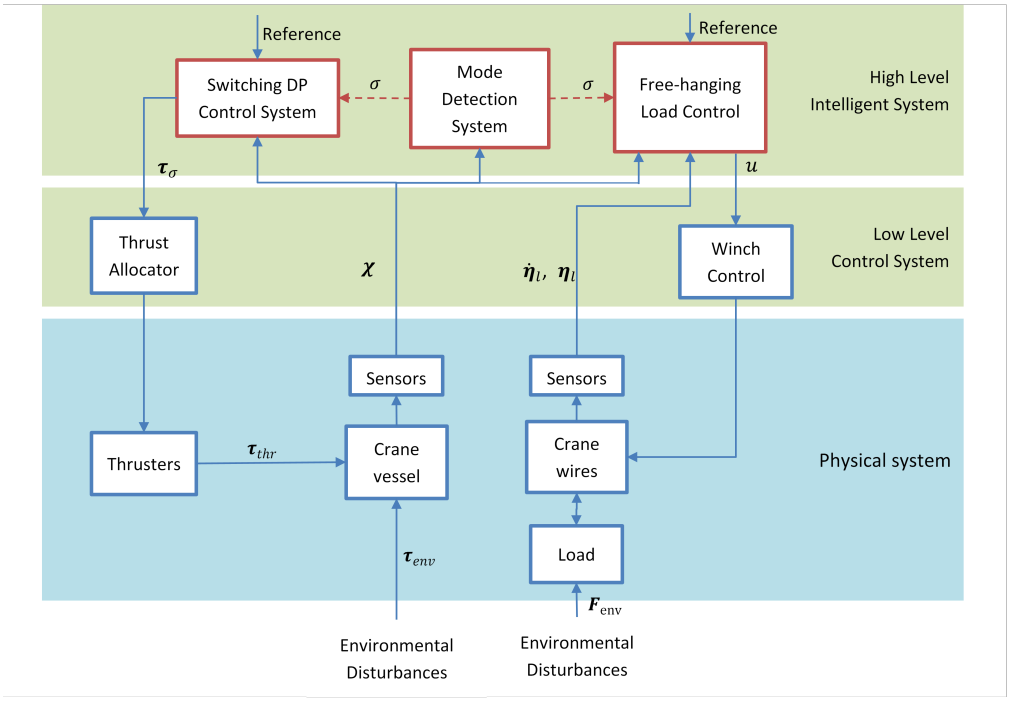

Figure 7.1: The proposed integrated system for smart offshore heavy lift operations

where

$$\bar{\gamma} = \begin{bmatrix} \bar{\boldsymbol{\omega}}_v + |\bar{\mathbf{R}}\boldsymbol{\nu}_{\mathrm{m}}| \\ \overline{\mathbf{M}}^{-1}\bar{\mathbf{C}}_{\mathrm{v}} \end{bmatrix}. \tag{7.7}$$

$$= \begin{bmatrix} [||[\bar{\omega}_{v1}, \bar{\omega}_{v2}, \bar{\omega}_{v3}]||[1,1,1], ||[\bar{\omega}_{v4}, \bar{\omega}_{v5}, \bar{\omega}_{v6}]||[1,1,1]]^T + |\bar{\mathbf{R}}(\bar{\boldsymbol{\omega}}_\eta)\boldsymbol{\nu}_{\mathrm{m}}(t)| \\ \overline{\mathbf{M}}^{-1}\bar{\mathbf{C}}_{\mathrm{v}} \end{bmatrix}, \tag{7.8}$$

$$\bar{h} = \begin{bmatrix} \mathbf{0} \\ \overline{\mathbf{M}}^{-1} \begin{bmatrix} F_{\mathrm{hoist}}\bar{\boldsymbol{\beta}} \\ \mathbf{r}_{ct} \times F_{\mathrm{hoist}}\bar{\boldsymbol{\beta}} \end{bmatrix} \end{bmatrix}, \tag{7.9}$$

with

$$\bar{\boldsymbol{\beta}} = \frac{|\mathbf{R}_3^T(\boldsymbol{\Theta}_{\mathrm{m}})(\boldsymbol{\eta}_{\mathrm{l}} - \boldsymbol{\eta}_{3\mathrm{m}}) - \mathbf{p}_{\mathrm{ct}}| + |\bar{\mathbf{R}}_3^T\boldsymbol{\eta}_{\mathrm{l}}| + ||\bar{\boldsymbol{\omega}}_{3\eta}||[1,1,1]^T + |\bar{\mathbf{R}}_3^T\boldsymbol{\eta}_{\mathrm{m}}|}{\left|||(\boldsymbol{\eta}_{\mathrm{l}} - \boldsymbol{\eta}_{3\mathrm{m}}) - \mathbf{R}_3(\boldsymbol{\Theta}_{\mathrm{m}})\mathbf{p}_{\mathrm{ct}}|| - ||\bar{\boldsymbol{\omega}}_{3\eta}|| - ||\bar{\mathbf{R}}_3\mathbf{p}_{\mathrm{ct}}||\right|} - \frac{\mathbf{R}_3^T(\boldsymbol{\Theta}_{\mathrm{m}})(\boldsymbol{\eta}_{\mathrm{l}} - \boldsymbol{\eta}_{3\mathrm{m}}) - \mathbf{p}_{\mathrm{ct}}}{||\mathbf{R}_3^T(\boldsymbol{\Theta}_{\mathrm{m}})(\boldsymbol{\eta}_{\mathrm{l}} - \boldsymbol{\eta}_{3\mathrm{m}}) - \mathbf{p}_{\mathrm{ct}}||}. \tag{7.10}$$

The details of $\boldsymbol{\lambda}$, $\bar{\boldsymbol{\chi}}(0)$, $\bar{\gamma}$, and $\bar{h}$ can be found in (5.23) to (5.75), and $H(s)$ is a diagonal matrix with stable first order filters.

The DP controller and the tension controller is based upon the output of the mode detection system. For the DP controller, the control algorithm follows:

$$\dot{\hat{\boldsymbol{\eta}}} = -\mathbf{K}_\sigma\hat{\boldsymbol{\eta}} + \mathbf{K}_{1\sigma}\tilde{\boldsymbol{\eta}} + \mathbf{R}_3\hat{\boldsymbol{\nu}}, \tag{7.11}$$

$$\dot{\hat{\boldsymbol{\nu}}} = -\hat{\mathbf{A}}_{1\sigma}\hat{\boldsymbol{\eta}} - \hat{\mathbf{A}}_{2\sigma}\hat{\boldsymbol{\nu}} + \mathbf{M}_\sigma^{-1}\boldsymbol{\tau}_\sigma + \mathbf{K}_{2\sigma}\hat{\boldsymbol{\eta}}, \tag{7.12}$$

$$\boldsymbol{\tau}_\sigma = \mathbf{M}_\sigma\{(\hat{\mathbf{A}}_{1\sigma} - \mathbf{K}_{2\sigma} - \mathbf{P}_{4\sigma}^{-1}\mathbf{R}_3^T\mathbf{P}_{3\sigma})\hat{\boldsymbol{\eta}} + (\hat{\mathbf{A}}_{2\sigma} - (\rho_\sigma + \rho_{1\sigma}))\hat{\boldsymbol{\nu}}\}, \tag{7.13}$$

where $\boldsymbol{\tau}_\sigma$ represents the required DP control force, with the actual thruster force being $\boldsymbol{\tau}_{\mathrm{thr}}$, and σ denotes the construction mode which satisfies

$$\sigma = \begin{cases} 1, t < t_{\mathrm{D}}, \\ 2, t \geq t_{\mathrm{D}}, \end{cases} \tag{7.14}$$

and the tuning gains satisfy (4.55) to (4.60).

The input to the crane winch is as follows:

$$u = \begin{cases} 0, & t \leq t_{\mathrm{l}}, \\ \dfrac{m_{\mathrm{l}}g}{t_{\mathrm{s}} - t_{\mathrm{l}}}(t - t_{\mathrm{s}}), & t_{\mathrm{l}} < t < t_{\mathrm{D}}, \\ m(f_2 + k_2\tilde{\zeta}_2 - \dot{\zeta}_{2\mathrm{d}} + \tilde{\zeta}_1), & t \geq t_{\mathrm{D}}, \end{cases} \tag{7.15}$$

where t_{l} is the starting time of loading procedure, t_{s} denotes the time when load is fully lifted from the platform (i.e., the switching time), and

$$\zeta_1 = ||\boldsymbol{\eta}_3 - \boldsymbol{\eta}_{\mathrm{l}} + \boldsymbol{R}^T(\boldsymbol{\Theta})\boldsymbol{p}_{\mathrm{ct}}||, \tag{7.16}$$

$$\zeta_2 = \frac{(\boldsymbol{\eta}_3 - \boldsymbol{\eta}_{\mathrm{l}} + \boldsymbol{R}^T(\boldsymbol{\Theta})\boldsymbol{p}_{\mathrm{ct}})^T\dot{\boldsymbol{\eta}}_{\mathrm{l}}}{||\boldsymbol{\eta}_3 - \boldsymbol{\eta}_{\mathrm{l}} + \boldsymbol{R}^T(\boldsymbol{\Theta})\boldsymbol{p}_{\mathrm{ct}}||}, \tag{7.17}$$

with $\tilde{\zeta}_2 = \zeta_2 - \zeta_{2d}$, $\tilde{\zeta}_1 = \zeta_1 - \zeta_{1d}$, and

$$f_2 = \frac{\boldsymbol{\chi}_1^T \boldsymbol{M}_l^{-1} \boldsymbol{D}_l \boldsymbol{\chi}_2 + \boldsymbol{\chi}_1^T \boldsymbol{M}_l^{-1} \boldsymbol{g}}{||\boldsymbol{\chi}_1||} \tag{7.18}$$

$$+ (\frac{\boldsymbol{\chi}_2^T}{||\boldsymbol{\chi}_2||} - \frac{\boldsymbol{\chi}_1^T \boldsymbol{\chi}_2 \boldsymbol{\chi}_1^T}{||\boldsymbol{\chi}_1||^3})(\varepsilon(\boldsymbol{\eta}) - \boldsymbol{\chi}_2), \tag{7.19}$$

$$\varepsilon(\boldsymbol{\eta}) = \frac{d}{dt}(\boldsymbol{\eta}_3(t) + \boldsymbol{R}^T(\boldsymbol{\Theta}(t))\boldsymbol{p}_{ct}) = \boldsymbol{R}^T(\boldsymbol{\Theta})\boldsymbol{\nu}_3(t) + \frac{\partial}{\partial t}\boldsymbol{R}^T(\boldsymbol{\Theta})\boldsymbol{p}_{ct}), \tag{7.20}$$

$$\zeta_{2d} = \zeta_{2d} = \dot{\zeta}_{1d} - k_1\tilde{\zeta}_1 - f_1, \tag{7.21}$$

with $k_1 > 0$, and

$$\zeta_{1d} = ||\boldsymbol{\chi}_{1d}||, \tag{7.22}$$

where $\boldsymbol{\chi}_{1d}$ denotes the desired position of the load. The signal of ζ_{2d} and $\dot{\zeta}_{2d}$ can be obtained from command filtering in (6.38) to (6.49).

The integration of the smart system is shown in (7.2) to (7.15). More details of the integrated system can be found in Chapter 4 to Chapter 6.

Remark 7.1 (The intelligence of the smart system)**.** *Previously, offshore heavy lift operations are carried out with human operators to observe the switch of the construction modes, and to switch the DP controller and the load controller to the desired mode. With the integrated system, the mode switch is observed by the detection system. Based on the result from the detection system, the DP controller can automatically switch to the desired mode, and the load controller can be automatically switched on. The integrated DP and load control system can obtain decisions by itself (without the need of operators), and has thus become more 'smart'. In this case, the integrated system can operate under harsher environmental conditions 24/7.*

Remark 7.2 (Measurement of load position)**.** *Although the load position is measured for load control in this smart control system, it is still important to have a mode detection system. This is because the measurement noise, external disturbances, and the possible sensor fault all may lead to wrong detection results if we are using only measured load position to detect the mode switch. The mode detection system utilizes analytical redundancy to capture the mode switch, while the use of load sensors constitutes a physical redundancy approach. These two approaches may be combined in order to enhance the mode detectability. Furthermore, as stated in Chapter 5, the proposed detection system can also be used to detect the sensor fault for the vessel.*

7.3. SIMULATIONS

In this section, simulations are made with the proposed integrated smart offshore heavy lift operations introducing first the simulation settings related to environmental disturbances and system overall design parameters. Then the results are given in figures. The simulations are analyzed after showing the results.

Then additional simulations have been run, in order to assess the integrated system under different environmental settings and different loads.

7.3.1. SIMULATION SETTINGS

The simulated scenario is an offshore removal operation by heavy lift vessels under DP control. First a nominal simulation is made with a load of 2000t under sea state 2. The crane wires are first connected to the load which is located on the platform. Given that the actual time of mode switching is $t_s = 600s$, and t_D is the detected mode switching time, the simulations consists of three phases:

- Phase 1 (Up to t_s): Initialization and lifting. The DP controller is set to Mode 1 (i.e., $\sigma = 1$) and the load controller is turned off. The crane controller gives a steady increasing torque input to lift the load from the platform.

- Phase 2 (From t_s to t_D): Detection gap. The load is lifted and is free-hanging in the air, but the detection system did not detect the change of the construction mode yet. During this period, the load controller stays off, the DP controller stays in Mode 1, and the torque of the hydraulic winch still increases in order to lift the load.

- Phase 3 (From t_D): After detection of Mode 2, the mode signal is updated (i.e., $\sigma = 2$) and sent to the DP controller and the load controller. The DP controller is then set to Mode 2, and the load controller is actuated.

The parameters used for the DP controller are listed in Section 4.4.2, parameters for the mode detection system are shown in Section 5.3, and parameters for the load controller can be found in Section 6.3. Setpoint of the load position is set to

$$\boldsymbol{\eta}_{ld} = \begin{bmatrix} -115 \\ 0 \\ -9.17 \end{bmatrix}, \tag{7.23}$$

and the setpoint of the vessel position $\boldsymbol{\eta}_d$ is first set to $\mathbf{0}$, then slowly switched to $[\frac{9m_l}{5000}\ 0\ 0]^T$ after t_D to compensate the position change due to the lifting of the load approximately.

Initially, the simulation is performed with a load of 2000t under sea state 2. Then we made extra simulations with different loads and environmental disturbances. During these simulations, we assume that we are able to measure the position of the CoG of the vessel, the velocity and angular velocity of the vessel, the position of the CoG of the load, and the velocity of the load. The measurement noise is set to a maximum of 0.1m for the positions, a maximum of 0.01m/s for the velocities, 0.1rad for the angles, and 0.01 rad/s for angular velocities.

7.3.2. SIMULATION RESULTS

In this section, simulations are made to test the proposed integrated smart system. The results are given in Figure 7.2 to Figure 7.5.

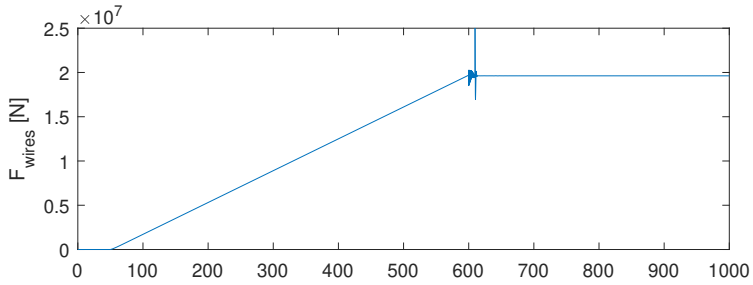

Figure 7.2: Tension in the wires (F_{hoist}) with a load of 2000t

According to Figure 7.2, the tension is first zero, then steadily increasing in Phase 1 due to the linear input from the load controller. At $t = t_s$, the load is lifted from the platform, but the detection system did not detect the mode switch and the load controller is still off, the hoist force is thus oscillating due to the sudden mode switch. After $t = t_D$, the mode switch is detected and the free-hanging load controller is switched on, the hoist force is thus stabilized with a slight oscillation.

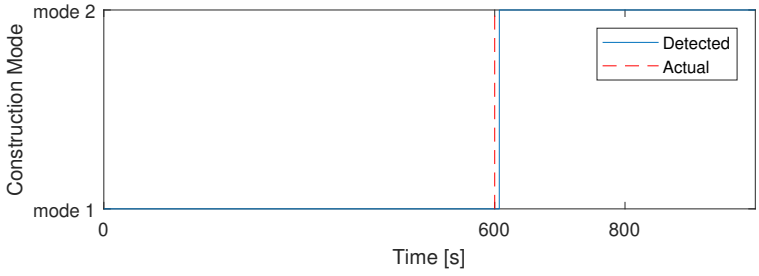

Figure 7.3: Mode switch and detected mode switch with a load of 2000t, with $t_D = 610.1s$

The switching of the construction modes and the detected of mode switch are shown in Figure 7.3, with the red dash line represents the mode switching time t_s, and the blue line represents the detected mode switch time t_D. In the simulated case, there is a time delay of $10.1s$ for the detection of the mode switch.

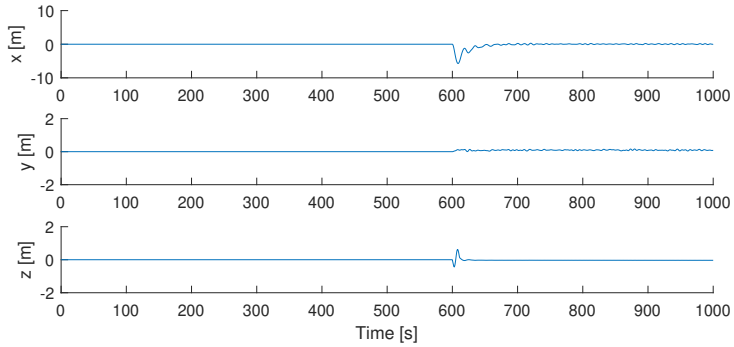

Figure 7.4: Load position error from the desired position ($\boldsymbol{\eta}_{\mathrm{l}} - \boldsymbol{\eta}_{\mathrm{ld}}$) (2000t)

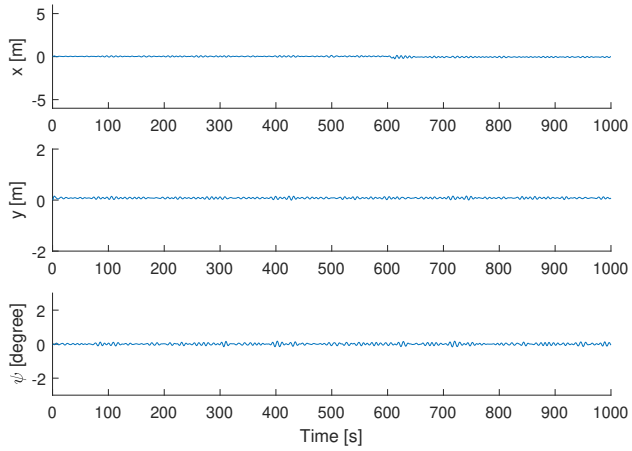

Figure 7.5: Vessel position error from the desired position ($\boldsymbol{\eta} - \boldsymbol{\eta}_{\mathrm{d}}$) with a load of 2000t

The load position error and the vessel position error are shown in Figure 7.4 and Figure 7.5. For the load position, the maximum position error (5m in north and 0.5m in down) happens after the mode switching and before the detection of the mode switch. For the vessel position, the oscillation of the position error has the highest value when $t_{\mathrm{s}} < t < t_{\mathrm{D}}$, when the mode has switched, but the switching has not been detected. During this period, the DP controller is still working under Mode 1, while the dynamics of the system have already switched to Mode 2, which has a negative influence on the stability of the DP control system.

Another simulation with a load of 2400t is made to compare to the above mentioned simulation. The simulation results are shown in Figure 7.6 to Figure 7.9.

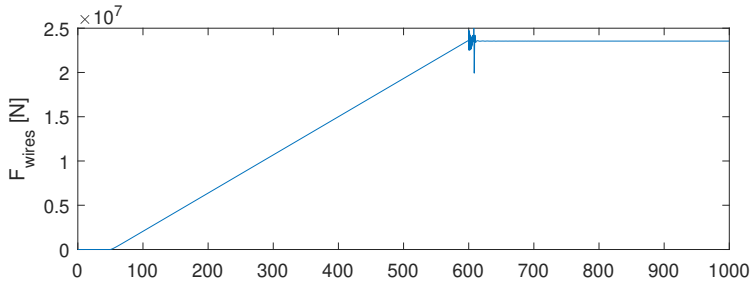

Figure 7.6: Tension in the wires (F_{hoist}) with a load of 2400t

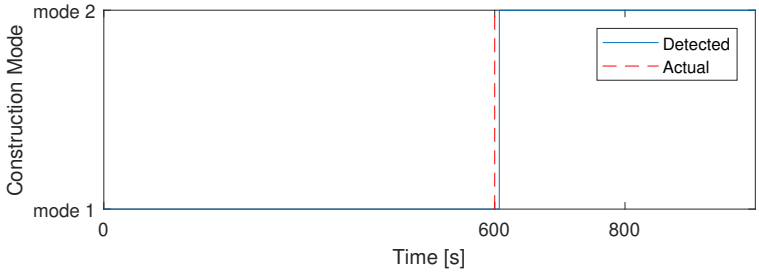

Figure 7.7: Mode switch and detected mode switch with a load of 2400t, with $t_{\text{D}} = 607.7s$

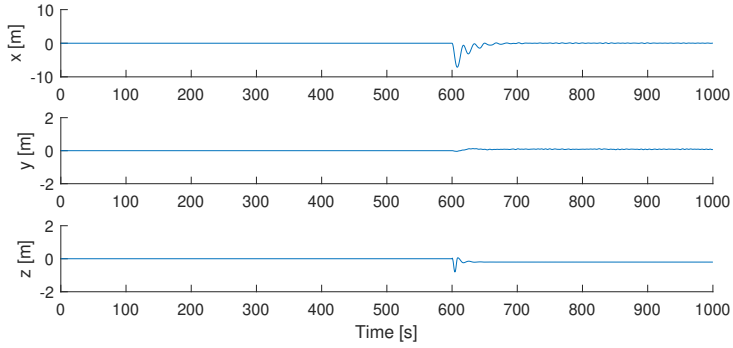

Figure 7.8: Load position error from the desired position ($\boldsymbol{\eta}_{\text{l}} - \boldsymbol{\eta}_{\text{ld}}$) (2400t)

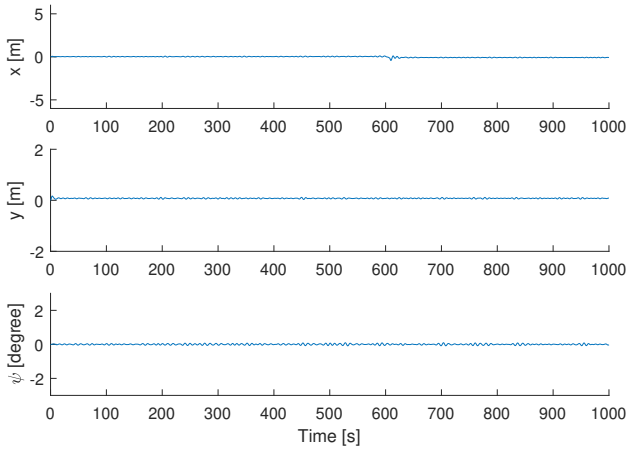

Figure 7.9: Vessel position error from the desired position($\boldsymbol{\eta} - \boldsymbol{\eta}_d$) with a load of 2400t

Comparing Figure 7.2 to Figure 7.9, it is observed that the detection system detects the construction mode switch faster when the load mass is higher, this can be justified by the facts that the detection time delay is 10.1s with a load of 2000t, is 7.7s when the load is 2400t. The DP controller and the load controller can stabilize the positions of the vessel and of the load during the simulations.

To investigate the impact of environmental loads on the integrated system, an additional simulation is made under sea state 0. The results of the simulation are presented in Figure 7.10 to Figure 7.13. Simulation results from Figure 7.12 and Figure 7.13 show that the position of the vessel and the position of the load are bounded in a smaller range comparing to the results in Figure 7.4 and Figure 7.5. The performance of the detection system is not significantly better or worse than the one simulated under sea state 2.

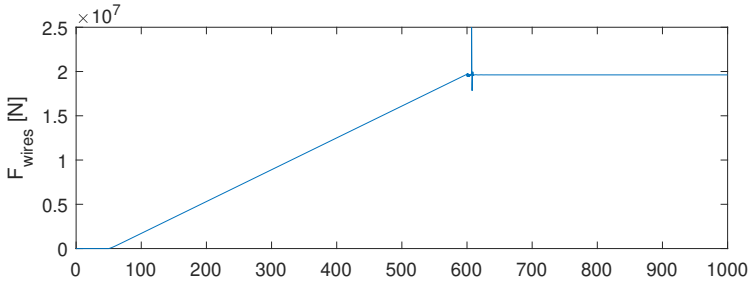

Figure 7.10: Tension in the wires (F_{hoist}) with a load of 2000t under sea state 0

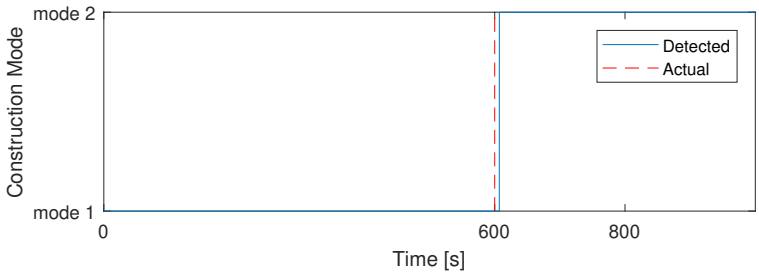

Figure 7.11: Mode switch and detected mode switch with a load of 2000t under sea state 0, with $t_D = 607.5s$

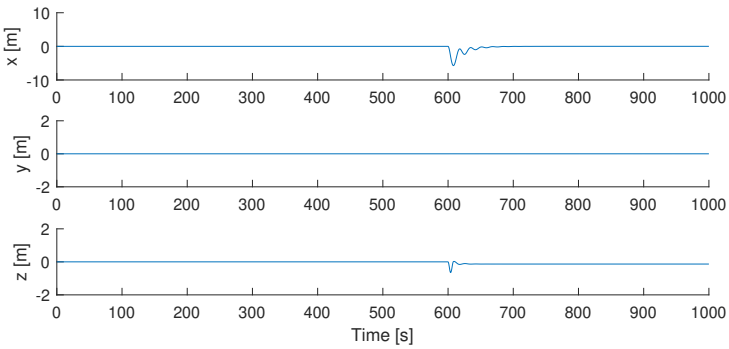

Figure 7.12: Load position error from the desired position ($\boldsymbol{\eta}_l - \boldsymbol{\eta}_{ld}$) under sea state 0 (2000t)

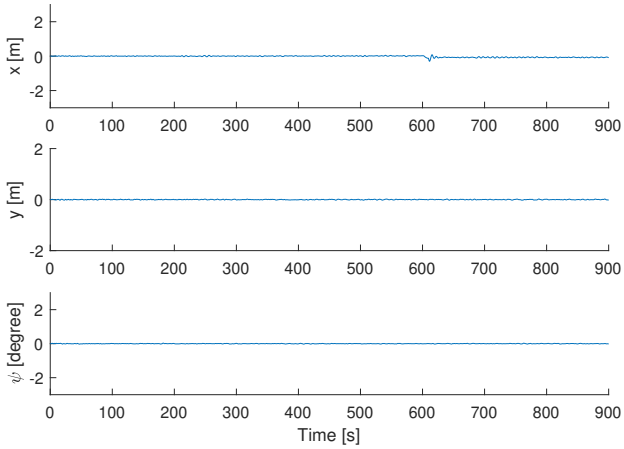

Figure 7.13: Vessel position error from the desired position ($\boldsymbol{\eta} - \boldsymbol{\eta}_d$) with a load of 2000t under sea state 0

To assess the integrated system under different environmental disturbances and with

different loads, more simulations are made. Results are shown in Tables:

Simulation results under different environmental disturbances

To test the performance of the integrated system under different sea states, simulations are made under different sea states with a load of 2000t. Each sea state is simulated ten times and the average results are shown in Table 7.2.

Sea state		0	1	2	3	4
RMSE of Vessel Position Error	North [m]	0.05	0.04	0.04	0.06	0.07
	East [m]	0.00	0.02	0.08	0.08	0.10
	Yaw [°]	0.00	0.00	0.03	0.06	0.09
Maximum Vessel Position Error	North [m]	0.28	0.31	0.28	0.29	0.28
	East [m]	0.00	0.05	0.16	0.16	0.20
	Yaw [°]	0.00	0.02	0.09	0.19	0.28
RMSE of Load Position Error	North [m]	0.01	0.02	0.05	0.10	0.17
	East [m]	0.00	0.03	0.08	0.10	0.13
	Down [m]	0.00	0.00	0.00	0.00	0.00
Maximum Load Position Error	North [m]	0.02	0.04	0.14	0.28	0.48
	East [m]	0.00	0.03	0.12	0.18	0.26
	Down [m]	0.00	0.00	0.00	0.00	0.01
Detection Delay [s]		7.1	8.2	10.5	10.5	12.3

Table 7.2: Simulation results of the integrated system under different environmental disturbances

The integrated system is able to detect the mode change within 13s, and maintain the vessel and the load's position under all simulation scenarios. However, with a higher sea state, the detection time delay becomes larger, which leads to a higher load offset in north and east, and a higher vessel position error in east and yaw. This is because the load controller is only activated when the mode switch is detected. It has to be noted that the choice of the setpoint of the vessel also has an influence on the performance of the load controller and the DP controller due to the interaction between the two controllers. This is also the reason why the down position of the load and the north position of the vessel are not following a simple decreasing or increasing trend. Furthermore, the values of the detection delay in Table 7.2 are different from that in Table 5.2. This is because of different simulation settings: In Chapter 5, simulations are made with an open-loop detection system, while in this chapter, the detection system, the DP controller, and the load controller together form a close-loop system with the vessel and load dynamics.

Simulation results with different loads

Simulations have been performed for offshore heavy lift operations with different loads under sea state 2, that represents the highest sea state allowed for offshore heavy lift operations under IMO rules. Each set of the settings is simulated 10 times, and the average results are shown in Table 7.3.

Load [tonnes]		1600	1800	2000	2200	2400
RMSE of Vessel Position Error	North [m]	0.03	0.04	0.04	0.05	0.06
	East [m]	0.08	0.08	0.08	0.08	0.08
	Yaw [°]	0.03	0.03	0.03	0.03	0.03
Maximum Vessel Position Error	North [m]	0.18	0.22	0.28	0.35	0.40
	East [m]	0.15	0.16	0.16	0.15	0.16
	Yaw [°]	0.09	0.09	0.09	0.08	0.09
RMSE of Load Position Error	North [m]	0.06	0.05	0.05	0.05	0.05
	East [m]	0.08	0.08	0.08	0.09	0.09
	Down [m]	0.00	0.00	0.00	0.00	0.00
Maximum Load Position Error	North [m]	0.23	0.14	0.15	0.13	0.14
	East [m]	0.12	0.11	0.12	0.11	0.11
	Down [m]	0.00	0.00	0.00	0.00	0.00
Detection Delay [s]		42.7	15.6	10.4	8.8	7.9

Table 7.3: Simulation results of the integrated system with different loads

The proposed integrated system is able to stabilize the position of the vessel and the load, and to detect the mode switch with different load weights. A heavier load leads to a shorter detection time delay. Thus the performance of the load controller is also better because of the earlier trigger of the load controller.

7.4. CONCLUSIONS

In this chapter, we answered *Subquestion 7: How to integrate the designed systems into a smart offshore operation system?* by integrating the DP controller in Chapter 4, the mode detection system in Chapter 5, and the load controller in Chapter 6. The integration of the smart offshore heavy lift operation system is explained and simulated for an offshore removal scenario. Simulation results show that the proposed smart operation system can handle the removal operation without human input. The simulations with different environmental loads (i.e., sea state 0 to sea state 4) and different load weights (i.e., from 1600t to 2400t) are able to maintain the position of the vessel with offsets less than 0.4m in all directions, and less than 0.1° in yaw. For the position of the load, the maximum load offset is less than 1.5m in all situations except for the one with a load of 1600t. Thus further research should be performed for optimizing the DP and load control design with respect to various system parameters.

Simulations also indicate that the environmental loads have a negative impact on the performance of the smart system in terms of position keeping. The weight of the load, on the contrary, helps the integrated system to detect the mode switch earlier and to keep the load's and the vessel's position better.

8

CONCLUSIONS AND RECOMMENDATIONS

IN the previous chapters, we focused on the design analysis and assessment of control and monitoring for offshore heavy lift operations. An integrated smart system was designed based on an observer-based robust switching controller, a mode detection system, and a nonlinear load controller. The purpose of the proposed smart system is to assist or replace human operations during the offshore heavy lift operations.

In this chapter, the conclusions of the research are drawn and future research on the related subjects is presented. In Section 8.1, the answers to the main research question and specific research questions are provided. In Section 8.2, the contributions of the thesis are summarized. Then, in Section 8.3, directions for relevant future research are given.

8.1. CONCLUSIONS

The goal of this thesis is to build an smart offshore heavy lift system to enhance the efficiency and ensure the safety of offshore constructions. The research was performed aiming to address the research question:

Main research question: How can we design smart control systems to improve the safety and reliability of offshore heavy lift operations under dynamic positioning?

In this research, we designed a smart system which consists of three subsystems: the DP robust switching control system (in chapter 4), model-based mode detection system (in Chapter 5), and the under-actuated nonlinear tension control system (in Chapter 6). An integration of the subsystems is done in Chapter 7. The proposed smart control system can detect different construction modes and give control signals to the crane and DP system accordingly. More specifically, answers to the research questions are as follows:

Answers to Specific research questions

The main research question was addressed through addressing the following subquestions.

Subquestion 1: What is the state of the art in smart offshore heavy lift operations?

In Chapter 2, we went through the literature related to smart heavy lift operations. According to the literature review, studies on smart offshore heavy lift operations are limited. Existing research focuses on DP systems and crane control systems. Model-based robust DP systems have been investigated for vessels with dynamic uncertainties and environment uncertainties. State of the art related to crane control systems includes the tracking control of low capacity under actuated container cranes, and the control of high capacity cranes in $x-z$ plane.

According to the literature review, the study on a smart offshore heavy lift system is missing. Firstly, there is no existing mode detection system that can detect the mode change during the construction work. Secondly, a theoretically stable model-based robust switching DP control designed for the heavy lift vessel is still missing in literature. Furthermore, the existing load controllers are nether for offshore crane-load system in full dimensions (i.e., at least 6 DoFs for the vessel, and 3 DoFs for the load), nor are with realistic actuators, which gives difficulties for the control of a offshore crane with large load.

Subquestion 2: How to model dynamic positioned offshore heavy lift operations?

In Chapter 3, a dynamic model is designed for dynamic positioned offshore heavy lift vessel. The construction is divided into three construction modes which can be concluded into two construction modes: The dynamics of the vessel-load system varies when the construction mode switches. When the load is on the platform, the system is in Mode 1. When the load is fully lifted and is free-hanging, the vessel-load system is defined to be in construction Mode 2.

The proposed model consists of 5 parts: dynamics of the vessel with the impact from the current, wave model and wind model, propulsion system, hydraulic crane, and the dynamics of the load. Simulation of the physical model with traditional PID controller shows that the maximum offset of the vessel during heavy lift operations is more than 6m. The stability of DP controller needs improvements.

Subquestion 3: How to solve the DP stability and robustness problem for heavy lift operations during Mode 1?

During Mode 1, the hoist force is increasing during time due to the lifting procedure. The external crane force on the vessel is time-varying. In Chapter 3, a robust observer-based controller is designed for the lifting procedure based on Lyapunov theory. The proposed control scheme assumed that several parameters of the vessel are unknown and bounded with a nominal value. Uncertainties include crane force, damping, and environmental loads. The proposed control scheme consists of a nonlinear observer and a feedback controller. The observer is designed to filter out high frequency signal (i.e., measurement noise and high-frequency wave induced movements) which the thrusters can not compensate. The feedback control receive the filtered measurement and gives control input to the system.

Proposed controller is tested with several simulations under different environmental loads and with different load and is proven to maintain the vessel's position with a maximum offset of less than 0.3m in all directions, less than 0.3° in yaw, in all simulated scenarios.

Subquestion 4: How to design a DP controller for heavy lift operations considering the mode switching during the operation?

Due to the change of the dynamics, the dynamic model built for Mode 1 is no longer valid in Mode 2. Thus, a switching controller is designed to control the vessel's position in both Mode 1 and Mode 2.

Based on the robust observer-based controller of Section 4.2, another observer-based switching control scheme is proposed in Section 4.3. The proposed switching controller has a similar structure as the observer-based robust controller for Mode 1. The gains of the controller vary with respect to different construction modes. The controller is first set to no load. When the lifting procedure starts, the controller switches to the setting of Mode 1. When the lifting procedure is over and the load is free-hanging, the controller switches to Mode 2. An average dwell time is defined to avoid fast switching between different sets of gains. The stability is proven for the proposed controller based on Lyapunov method. Simulation results show that the switching controller is able to maintain the vessel's position even when the vessel model is switched from Mode 1 to Mode 2. The maximum offset of the vessel is maintained within 0.3m in all directions, and the yaw angle is controlled with a maximum offset of 0.3°.

Subquestion 5: How to design a software-based system to detect the switching of the construction mode during offshore heavy lift operations?

The heavy lift operations in Mode 1 and Mode 2 have different dynamics. To distinguish these two modes automatically, a model-based detection system is designed. Such detection system is also necessary for the functionality of the switching controller, which is proposed to answer *Question 4*. The proposed detection system is based on the dynamic model of the vessel-load system during Mode 1, and consists of a residual generator, a threshold generator, and the decision logic. The residual is calculated using a model-based observer designed for the vessel-load system in Mode 1. By considering the measurement noise and the environmental disturbances, the time-dependent threshold is designed. The decision logic is based on checking whether the residual is below the threshold. The switching is inferred when the magnitude of the residual is above the threshold. Such detection system can detect the switch between Mode 1 and Mode 2 within 11 seconds during the simulations with load of 1800t to 2400t, and during the simulations under different sea state (i.e., sea state 0 to sea state 4).

Subquestion 6: How to design a nonlinear control system for the under-actuated heavy load?

During construction Mode 1, the crane wires are first attached to the load, and then the tension in the wires is increasing gradually to lift the load. When the load is fully lifted, the hoist force should be controlled to stabilize the load. In heavy lift operations, the crane on board is usually huge with limited manoeuvrability. Thus the load is under-actuated when it is free-hanging. In Chapter 5, a nonlinear controller is made for the

free-hanging load while the vessel is under DP control. The proposed controller is an under-actuated controller with input of only one dimension. The load control system is designed following a backstepping control and command filtering approach. The maximum offset of the load is maintained within 0.4m in all simulated scenarios.

Subquestion 7: How to integrate the designed systems into a smart offshore operation system?
In Chapters 4 to 6, the subsystems for the smart offshore operation system are proposed. Then in Chapter 7, the above mentioned subsystems are integrated into one system. The upper level control system, which is the mode detection system, gives mode signal to the smart system. During the offshore construction, when the mode signal switches, the DP controller for Mode 2 and the tension controller are triggered. The main research question is addressed by integrating the control and monitoring systems developed to improve the efficiency of the heavy lift operations safely. The results show that the proposed integrated system is able to handle the offshore heavy lifting without human input. However, for lower load (i.e., with a load of 1600t or lower), the detection time becomes too large (i.e., more than 50s), which leads to a larger load offset (i.e.,more than 3m in North). Thus the system is recommended for usage with heavy loads.

8.2. CONTRIBUTIONS OF THE THESIS

In this thesis, control algorithms are proposed to solve the problem of smart offshore heavy lift construction. The proposed systems are integrated into one smart system which improves the safety and time efficiency during offshore heavy lift operations. The contribution of the thesis can be summarized as follows:

- In Chapter 3, an innovative model of the heavy lift vessel and the load during a complete heavy lift operation is proposed. The vessel dynamics is in 6 DoFs, and the load is in 3 DoFs. The model is given in equations and is tested in simulations. Such model contains the crane winch, the propulsion system, and environmental disturbances, and is using a modular design.

- In Chapter 4, a novel observer based robust DP controller for crane vessel in Mode 1, and a switching DP controller for crane vessels in Mode 1 and Mode 2 have been developed. The controllers are designed to guarantee the dynamic positioning of the crane vessel during lifting of a heavy load and under environmental disturbances.

- In Chapter 5, an innovative model-based detection system is proposed for offshore heavy lift operation to detect the switching from Mode 1 to Mode 2. The proposed monitoring scheme is designed to ensure the fast detection of the mode switching necessary to guarantee the DP of the vessel during the whole construction.

- In Chapter 6, a backstepping controller is designed for the free-hanging load to stabilize the position of the load while the vessel is under DP control. The control design tackles the problem of underactuation and offers an effective solution to control the position of the load using only the tension in the wires.

- In Chapter 7, subsystems designed in Chapter 4 to Chapter 6 are integrated and simulated. The integrated system can carry out the position control of the vessel and the load during offshore removal work smartally, and can be used to achieve autonomous offshore heavy lifting or to assist human operators on board to improve safety during offshore assignments.

8.3. RECOMMENDATIONS FOR FUTURE RESEARCH

In this section, recommendations are given for future work related to smart offshore construction.

8.3.1. OPTIMIZATION OF THE PERFORMANCE

The gains in Chapter 4 to Chapter 6 are chosen such that the controller or the detection system is theoretically stable. However, the optimization of the control gains is not discussed in this thesis. However, optimization of the gains is an interesting topic. The gains can be optimized in several ways: either to optimize the performance of the controller, or to optimize the energy efficiency.

8.3.2. FAILURE MODES ANALYSIS

In this thesis, the smart system is based on the assumption that sensors and other systems on board of the heavy lift vessel are functioning properly. However, this is not always the case in real life. The sensors might be damaged, and the engines on board can fail during the operation. Further study can focus on the fault diagnosis and fault tolerant control for realizing the autonomy of offshore heavy lift operations.

8.3.3. COMPLICATED OFFSHORE CONSTRUCTIONS

In this thesis, an smart offshore removal operation from a fixed platform is investigated. In reality, there are different types of offshore heavy lift operations. More complicated case can be found with removal from or installation on a floating structure, or the construction work related to the windmills which requires the load to be stabilized within a certain rotation angle. This can be further studied by adding dynamics to the load during Mode 1, or by extend the dimensions of the load.

8.3.4. AUTONOMOUS OFFSHORE HEAVY LIFT OPERATIONS

An autonomous offshore heavy lift operation can be achieved by design and integrate other smart systems on board of the heavy lift vessel. This includes automation in ballast system, energy distribution system, power management system, remote control system, and many more, as well as the integration of these smart systems.

8.3.5. PHYSICAL EXPERIMENTS WITH SCALED HEAVY LIFT VESSEL

The proposed smart system has been proven to work both theoretically and in simulations. However, if we want to apply it in reality, a physical experiment is still missing to test the reliability of the proposed method before adapting it in reality. The first step of the experiment can be carried out in the water tank with a scaled model. Afterwards, it can be installed on a real heavy lift vessel and be tested during an offshore heavy lift

construction.

BIBLIOGRAPHY

[1] M. Althoff, O. Stursberg, and M. Buss. Model-based probabilistic collision detection in autonomous driving. *IEEE Transactions on Intelligent Transportation Systems*, 10(2):299–310, 2009.

[2] P. Aryan, A. Kotousov, C.-T. Ng, and B. Cazzolato. A model-based method for damage detection with guided waves. *Structural Control and Health Monitoring*, 24(3):e1884, 2017.

[3] H. Badihi, Y. Zhang, and H. Hong. Fault-tolerant cooperative control in an offshore wind farm using model-free and model-based fault detection and diagnosis approaches. *Applied Energy*, 201:284–307, 2017.

[4] F. C. Bakker. A conceptual solution to instable dynamic positioning during offshore heavy lift operations using computer simulation techniques. Master's thesis, Delft University of Technology, 2015.

[5] J. G. Balchen, N. A. Jenssen, E. Mathisen, and S. Saelid. Dynamic positioning of floating vessles based on kalman filtering and optimal control. In *1980 19th IEEE Conference on Decision and Control including the Symposium on Adaptive Processes*, pages 852–864. IEEE, 1980.

[6] S. Beadnall and S. Moore. *Offshore construction: Law and practice*. Informa Law from Routledge, 2016.

[7] Bercha Group. Arctic offshore escape, evacuation, and rescue. In *17th International Symposium on Ice, IAHR*, 2004.

[8] F. Berkelaar. Crane ship - wei li - maasmond - port of rotterdam. `https://www.flickr.com/photos/28169156@N03/21219259898`, 2015.

[9] O. Blancke, A. Tahan, D. Komljenovic, N. Amyot, C. Hudon, and M. Lévesque. A hydrogenerator model-based failure detection framework to support asset management. In *2016 IEEE International Conference on Prognostics and Health Management (ICPHM)*, pages 1–6. IEEE, 2016.

[10] M. Börner and R. Isermann. Model-based detection of critical driving situations with fuzzy logic decision making. *Control Engineering Practice*, 14(5):527–536, 2006.

[11] E. F. Brater and H. W. King. *Handbook of hydraulics for the solution of hydraulic engineering problems*. Mcgraw-Hill, 1976.

[12] A. H. Brodtkorb, S. A. Værnø, A. R. Teel, A. J. Sørensen, and R. Skjetne. Hybrid controller concept for dynamic positioning of marine vessels with experimental results. *Automatica*, 93:489–497, 2018.

[13] J. Cai, H. Ferdowsi, and J. Sarangapani. Model-based fault detection, estimation, and prediction for a class of linear distributed parameter systems. *Automatica*, 66:122–131, 2016.

[14] S. Cho, Z. Gao, and T. Moan. Model-based fault detection, fault isolation and fault-tolerant control of a blade pitch system in floating wind turbines. *Renewable Energy*, 120:306–321, 2018.

[15] Y. Chu, F. Sanfilippo, V. Æsøy, and H. Zhang. An effective heave compensation and anti-sway control approach for offshore hydraulic crane operations. In *2014 IEEE International Conference on Mechatronics and Automation*, pages 1282–1287. IEEE, 2014.

[16] T. Danisman, I. M. Bilasco, C. Djeraba, and N. Ihaddadene. Drowsy driver detection system using eye blink patterns. In *2010 International Conference on Machine and Web Intelligence*, pages 230–233, Oct 2010.

[17] S. Dey, H. E. Perez, and S. J. Moura. Model-based battery thermal fault diagnostics: Algorithms, analysis, and experiments. *IEEE Transactions on Control Systems Technology*, 27(2):576–587, 2017.

[18] K. D. Do and J. Pan. Nonlinear control of an active heave compensation system. *Ocean engineering*, 35(5-6):558–571, 2008.

[19] K. D. Do and J. Pan. Nonlinear control of an active heave compensation system. *Ocean engineering*, 35(5-6):558–571, 2008.

[20] K. Doerr. Discharge cooler trial lift. `https://www.flickr.com/photos/kendoerr/7707950884`, 2012.

[21] J. Du, X. Hu, M. Krstić, and Y. Sun. Dynamic positioning of ships with unknown parameters and disturbances. *Control Engineering Practice*, 76:22–30, 2018.

[22] J. Du, Y. Yang, D. Wang, and C. Guo. A robust adaptive neural networks controller for maritime dynamic positioning system. *Neurocomputing*, 110:128–136, 2013.

[23] E. Echavarria, T. Tomiyama, H. Huberts, and G. Van Bussel. Fault diagnosis system for an offshore wind turbine using qualitative physics. In *Proc. EWEC*. Citeseer, 2008.

[24] M. A. El-Reedy. *Offshore structures: Design, construction and maintenance*. Gulf Professional Publishing, 2019.

[25] Y. Fang and P. Wang. Advanced nonlinear control of an offshore boom crane. In *2012 American Control Conference (ACC)*, pages 5421–5426. IEEE, 2012.

[26] Y. Fang, P. Wang, N. Sun, and Y. Zhang. Dynamics analysis and nonlinear control of an offshore boom crane. *IEEE Transactions on Industrial Electronics*, 61(1):414–427, 2013.

[27] P. S. Fard, H. Tohidi, and H. Moayeri. Boom structural design and static finite element analysis for a 1000tons sheerleg offshore crane. *International Research Journal of Engineering and Technology*, pages 485–495, 2016.

[28] J. A. Farrell and M. M. Polycarpou. *Adaptive approximation based control: unifying neural, fuzzy and traditional adaptive approximation approaches*, volume 48. John Wiley & Sons, 2006.

[29] R. J. Flint and R. Stephens. Dynamic positioning for heavy lift applications. In *Dynamic Positioning Conference*, 2008.

[30] T. I. Fossen. Nonlinear passive control and observer design for ships. *Modeling, Identification and control*, 21(3):129, 2000.

[31] T. I. Fossen. *Handbook of marine craft hydrodynamics and motion control*. John Wiley & Sons, 2011.

[32] T. I. Fossen and A. Grovlen. Nonlinear output feedback control of dynamically positioned ships using vectorial observer backstepping. *IEEE transactions on control systems technology*, 6(1):121–128, 1998.

[33] T. I. Fossen and J. P. Strand. Passive nonlinear observer design for ships using lyapunov methods: full-scale experiments with a supply vessel. *Automatica*, 35(1):3–16, 1999.

[34] Q. Fu, H. Wan, and F. Qiu. Pipeline leak detection based on fiber optic early-warning system. *Procedia Engineering*, 7:88–93, 2010.

[35] Z. Gao, C. Cecati, and S. X. Ding. A survey of fault diagnosis and fault-tolerant techniques—part i: Fault diagnosis with model-based and signal-based approaches. *IEEE Transactions on Industrial Electronics*, 62(6):3757–3767, 2015.

[36] R. D. Geertsma, R. R. Negenborn, K. Visser, M. A. Loonstijn, and H. J. Hopman. Pitch control for ships with diesel mechanical and hybrid propulsion: Modelling, validation and performance quantification. *Applied Energy*, 206:1609–1631, 2017.

[37] J. Gertler. *Fault detection and diagnosis in engineering systems*. Routledge, 2017.

[38] J. J. Gertler. Survey of model-based failure detection and isolation in complex plants. *IEEE Control Systems Magazine*, 8(6):3–11, Dec 1988.

[39] M. Godjevac and M. Drijver. Performance evaluation of an inland pusher. In *Transport of Water versus Transport over Water*, pages 389–411. Springer, 2015.

[40] R. Grace, V. E. Byrne, D. M. Bierman, J.-M. Legrand, D. Gricourt, B. Davis, J. J. Staszewski, and B. Carnahan. A drowsy driver detection system for heavy vehicles. In *17th DASC. AIAA/IEEE/SAE. Digital Avionics Systems Conference. Proceedings (Cat. No. 98CH36267)*, volume 2, pages I36/1–I36/8. IEEE, 1998.

[41] A. Grovlen and T. I. Fossen. Nonlinear control of dynamic positioned ships using only position feedback: An observer backstepping approach. In *Decision and Control, 1996., Proceedings of the 35th IEEE Conference on*, volume 3, pages 3388–3393. IEEE, 1996.

[42] E. Harmsen, R. van Dijk, and P. Stuberg. Dp-stability during heavy lift operations using a modified kalman filter. In *ASME 2018 37th International Conference on Ocean, Offshore and Arctic Engineering*, pages V001T01A065–V001T01A065. American Society of Mechanical Engineers, 2018.

[43] X. He, W. He, J. Shi, and C. Sun. Boundary vibration control of variable length crane systems in two-dimensional space with output constraints. *IEEE/ASME Transactions on Mechatronics*, 22(5):1952–1962, 2017.

[44] M. Hendrapati, J. Sumardi, Judhariksawan, M. Napang, Anshar, H. Subhandi, and Y. Kristianto. Offshore installation removal in the interest of navigation safety from international law point of view. *JL Pol'y & Globalization*, 66:194–204, 11 2017.

[45] J. P. Hespanha and A. S. Morse. Stability of switched systems with average dwell-time. In *Proceedings of the 38th IEEE Conference on Decision and Control*, volume 3, pages 2655–2660. IEEE, 1999.

[46] X. Hu and J. Du. Robust nonlinear control design for dynamic positioning of marine vessels with thruster system dynamics. *Nonlinear Dynamics*, pages 1–12, 2018.

[47] R. Isermann. *Fault-diagnosis systems: An introduction from fault detection to fault tolerance*. Springer Verlag, 2006.

[48] R. R. Ismail and Q. Ha. Trajectory tracking and anti-sway control of three-dimensional offshore boom cranes using second-order sliding modes. In *2013 IEEE International Conference on Automation Science and Engineering (CASE)*, pages 996–1001. IEEE, 2013.

[49] R. R. Ismail, N. D. That, and Q. P. Ha. Modelling and robust trajectory following for offshore container crane systems. *Automation in Construction*, 59:179–187, 2015.

[50] M. Katebi, I. Yamamoto, M. Matsuura, M. Grimble, H. Hirayama, and N. Okamoto. Robust dynamic ship positioning control system design and applications. *International Journal of Robust and Nonlinear Control: IFAC-Affiliated Journal*, 11(13):1257–1284, 2001.

[51] H. K. Khalil. *Nonlinear systems*, volume 3. Prentice hall Upper Saddle River, NJ, 2002.

[52] K. Krissian, G. Malandain, N. Ayache, R. Vaillant, and Y. Trousset. Model-based detection of tubular structures in 3d images. *Computer vision and image understanding*, 80(2):130–171, 2000.

[53] S. Küchler, T. Mahl, J. Neupert, K. Schneider, and O. Sawodny. Active control for an offshore crane using prediction of the vessel's motion. *IEEE/ASME Transactions on Mechatronics*, 16(2):297–309, 2010.

[54] G. Lai, Z. Liu, Y. Zhang, C. P. Chen, and S. Xie. Adaptive backstepping-based tracking control of a class of uncertain switched nonlinear systems. *Automatica*, 91:301–310, 2018.

[55] O. Levander. Autonomous ships on the high seas. *IEEE Spectrum*, 54(2):26–31, 2017.

[56] R. Li, K. Hansen, F. Beltrami, et al. A technical investigation on the ongoing evolution of the market of offshore installation vessels. In *SPE Annual Technical Conference and Exhibition*. Society of Petroleum Engineers, 2016.

[57] S. Li, X. Zhao, and G. Zhou. Automatic pixel-level multiple damage detection of concrete structure using fully convolutional network. *Computer-Aided Civil and Infrastructure Engineering*, 34(7):616–634, 2019.

[58] Y. Liang, M. L. Reyes, and J. D. Lee. Real-time detection of driver cognitive distraction using support vector machines. *IEEE transactions on intelligent transportation systems*, 8(2):340–350, 2007.

[59] D. Liberzon. *Switching in systems and control*. Springer Science & Business Media, 2003.

[60] Lloyd's Register. Design code for unmanned marine systems. `https://www.cdinfo.lr.org/information/documents/ShipRight/Design%20and%20Construction/Additional%20Design%20Procedures/Design%20Code%20for%20Unmanned%20Marine%20Systems/Design%20Code%20for%20Unmanned%20Marine%20Systems,%20February%202017.pdf`, 2017.

[61] P. V. P. Lopes, L. Hsu, M. Vilzmann, and K. Kondak. Model-based sensor fault detection in an autonomous solar-powered aircraft. In *FT2019. Proceedings of the 10th Aerospace Technology Congress, October 8-9, 2019*, 162, pages 247–254. Linköping University Electronic Press, 2019.

[62] A. Loria and H. Nijmeijer. Encyclopaedia of life support systems (eolss). vol. perspectives and overview of life support systems and sustainable development, chapter passivity based control, 2002.

[63] B. Lu, Y. Fang, and N. Sun. Nonlinear coordination control of offshore boom cranes with bounded control inputs. *International Journal of Robust and Nonlinear Control*, 29(4):1165–1181, 2019.

[64] B. Lu, Y. Fang, N. Sun, and X. Wang. Antiswing control of offshore boom cranes with ship roll disturbances. *IEEE Transactions on Control Systems Technology*, 26(2):740–747, 2017.

[65] S. R. Mangoubi and M. A. Edelmayer. Model based fault detection: the optimal past, the robust present and a few thoughts on the future. *IFAC Proceedings Volumes*, 33(11):65–76, 2000.

[66] S. Messineo and A. Serrani. Offshore crane control based on adaptive external models. *Automatica*, 45(11):2546–2556, 2009.

[67] N. Mishra, A. Saraf, et al. Leak detection system applicability for offshore and onshore oil and gas pipelines. In *SPE Oil and Gas India Conference and Exhibition*. Society of Petroleum Engineers, 2019.

[68] B. W. Nam, S. Y. Hong, Y. S. Kim, J. W. Kim, et al. Effects of passive and active heave compensators on deepwater lifting operation. *International Journal of Offshore and Polar Engineering*, 23(01), 2013.

[69] S. Natarajan and R. Srinivasan. Multi-model based process condition monitoring of offshore oil and gas production process. *Chemical Engineering Research and Design*, 88(5):572 – 591, 2010.

[70] Q. H. Ngo and K.-S. Hong. Sliding-mode antisway control of an offshore container crane. *IEEE/ASME Transactions on Mechatronics*, 17(2):201–209, 2012.

[71] Q. H. Ngo, N. P. Nguyen, C. N. Nguyen, T. H. Tran, and V. H. Bui. Payload pendulation and position control systems for an offshore container crane with adaptive-gain sliding mode control. *Asian Journal of Control*, 2019.

[72] N. P. Nguyen, Q. H. Ngo, and Q. P. Ha. Active control of an offshore container crane. In *2015 15th International Conference on Control, Automation and Systems (ICCAS)*, pages 773–778. IEEE, 2015.

[73] J. Ni, S. Liu, M. Wang, X. Hu, and Y. Dai. The simulation research on passive heave compensation system for deep sea mining. In *2009 International Conference on Mechatronics and Automation*, pages 5111–5116. IEEE, 2009.

[74] R. D. Olney and S. Manorotkul. Driver adaptive collision warning system, Apr. 17 2007. US Patent 7,206,697.

[75] L. O'neill, E. Fakas, B. Ronalds, P. Christiansen, et al. History, trends and evolution of float-over deck installation in open waters. In *SPE Annual Technical Conference and Exhibition*. Society of Petroleum Engineers, 2000.

[76] M. J. Paulsen and O. Egeland. Passive output feedback and observer based autopilots: a comparative study. *IFAC Proceedings Volumes*, 28(2):123–130, 1995.

[77] Y. Qian, Y. Fang, and B. Lu. Adaptive repetitive learning control for an offshore boom crane. *Automatica*, 82:21 – 28, 2017.

[78] V. Reppa, M. M. Polycarpou, C. G. Panayiotou, et al. Sensor fault diagnosis. *Foundations and Trends® in Systems and Control*, 3(1-2):1–248, 2016.

[79] V. Reppa, S. Timotheou, M. M. Polycarpou, and C. G. Panayiotou. Optimization of observer design for sensor fault detection of nonlinear systems. In *2017 IEEE 56th Annual Conference on Decision and Control (CDC)*, pages 5155–5160. IEEE, 2017.

[80] S. Roy and S. Baldi. On reduced-complexity robust adaptive control of switched euler–lagrange systems. *Nonlinear Analysis: Hybrid Systems*, 34:226–237, 2019.

[81] S. Roy and S. Baldi. A simultaneous adaptation law for a class of nonlinearly-parametrized switched systems. *IEEE Control Systems Letters*, 3(3):487–492, 2019.

[82] S. Roy, J. Lee, and S. Baldi. A new adaptive-robust design for time delay control under state-dependent stability condition. *IEEE Transactions on Control Systems Technology*, 2020.

[83] D. M. Schroeder and M. S. Love. Ecological and political issues surrounding decommissioning of offshore oil facilities in the southern california bight. *Ocean & Coastal Management*, 47(1-2):21–48, 2004.

[84] L. Shuguang, G. Qian, and Z. Wenpu. Research on active heave compensation for offshore crane. In *The 26th Chinese Control and Decision Conference (2014 CCDC)*, pages 1768–1772. IEEE, 2014.

[85] A. J. Sørensen. *Modelling and control of SES dynamics in the vertical plane, Dr. Ing.* PhD thesis, thesis, ITK-report 1993: 7-W, Nor. Inst. Technol., Trondheim, 1993.

[86] A. J. Sørensen and O. Egeland. Design of ride control system for surface effect ships using dissipative control. *Automatica*, 31(2):183–199, 1995.

[87] A. J. Sørensen, S. I. Sagatun, and T. I. Fossen. Design of a dynamic positioning system using model-based control. *Control Engineering Practice*, 4(3):359–368, 1996.

[88] N. Sun, Y. Fang, H. Chen, and B. He. Adaptive nonlinear crane control with load hoisting/lowering and unknown parameters: Design and experiments. *IEEE/ASME Transactions on Mechatronics*, 20(5):2107–2119, 2015.

[89] X. Sun, D. Huang, and G. Wu. The current state of offshore wind energy technology development. *Energy*, 41(1):298–312, 2012.

[90] Y.-G. Sun, H.-Y. Qiang, J. Xu, and D.-S. Dong. The nonlinear dynamics and anti-sway tracking control for offshore container crane on a mobile harbor. *J. Marine Sci. Technol.-Taiwan*, 25(6):656–665, 2017.

[91] Z. Sun, G. Zhang, L. Qiao, and W. Zhang. Robust adaptive trajectory tracking control of underactuated surface vessel in fields of marine practice. *Journal of Marine Science and Technology*, pages 1–8, 2018.

[92] A. Tahar, J. Halkyard, A. Steen, and L. Finn. Float over installation method—comprehensive comparison between numerical and model test results. *Journal of Offshore Mechanics and Arctic Engineering*, 128:256–262, 2006.

[93] J. Tambke, M. Lange, U. Focken, J.-O. Wolff, and J. A. Bye. Forecasting offshore wind speeds above the north sea. *Wind Energy: An International Journal for Progress and Applications in Wind Power Conversion Technology*, 8(1):3–16, 2005.

[94] J. Tang and Q. Wang. Online fault diagnosis and prevention expert system for dredgers. *Expert Systems with Applications*, 34(1):511–521, 2008.

[95] F. Tango and M. Botta. Real-time detection system of driver distraction using machine learning. *IEEE Transactions on Intelligent Transportation Systems*, 14(2):894–905, 2013.

[96] The Maritime Excecutive. Decommissioning: Platform removal needs rethink. `https://www.maritime-executive.com/article/decommissioning-platform-removal-needs-rethink`, 2018.

[97] S. A. Værnø, R. Skjetne, Ø. K. Kjerstad, and V. Calabrø. Comparison of control design models and observers for dynamic positioning of surface vessels. *Control Engineering Practice*, 85:235–245, 2019.

[98] F. Van Hoorn. Heavy-lift transport ships: overview of existing fleet and future developments. In *Marine Operations Specialty Symposium (MOSS 2008)*, pages 5–7, 2008.

[99] F. Vicente, Z. Huang, X. Xiong, F. De la Torre, W. Zhang, and D. Levi. Driver gaze tracking and eyes off the road detection system. *IEEE Transactions on Intelligent Transportation Systems*, 16(4):2014–2027, 2015.

[100] O. Waals. On the use of main hoist tension measurement for feed forward in dp systems during offshore installations. In *ASME 2010 29th International Conference on Ocean, Offshore and Arctic Engineering*, pages 393–400. American Society of Mechanical Engineers, 2010.

[101] A. Wang, Y. Yang, S. Zhu, H. Li, J. Xu, M. He, et al. Latest progress in deepwater installation technologies. In *The Twenty-second International Offshore and Polar Engineering Conference*. International Society of Offshore and Polar Engineers, 2012.

[102] Y. Wang, Y. Tuo, S. X. Yang, M. Biglarbegian, and M. Fu. Reliability-based robust dynamic positioning for a turret-moored floating production storage and offloading vessel with unknown time-varying disturbances and input saturation. *ISA Transactions*, 2018.

[103] J. Xiang and M. Liang. Wavelet-based detection of beam cracks using modal shape and frequency measurements. *Computer-Aided Civil and Infrastructure Engineering*, 27(6):439–454, 2012.

[104] J. Ye. Dynamic positioning during heavy lift operations: Using fuzzy control techniques, nonlinear observer and h-infinity method separately to obtain stable dp systems for heavy lift operations. Master's thesis, Delft University of Technology, 2016.

[105] J. Ye, M. Godjevac, S. Baldi, and H. Hopman. Joint estimation of vessel position and mooring stiffness during offshore crane operations. *Automation in Construction*, 101:218–226, 2019.

[106] J. Ye, S. Roy, M. Godjevac, and S. Baldi. Observer-based robust control for dynamic positioning of large-scale heavy lift vessels. *IFAC-PapersOnLine*, 52(3):138–143, 2019.

[107] J. Ye, S. Roy, M. Godjevac, and S. Baldi. A switching control perspective on the offshore construction scenario of heavy-lift vessels. *IEEE Transactions on Control Systems Technology*, 2020.

[108] K. S. Youssef, S. A. Ragab, A. H. Nayfeh, and D. T. Mook. Design of passive anti-roll tanks for roll stabilization in the nonlinear range. *Ocean Engineering*, 29(2):177–192, 2002.

[109] Q. Yu, R. Xiong, and C. Lin. Model-based sensor fault detection for lithium-ion batteries in electric vehicles. In *2019 IEEE 89th Vehicular Technology Conference (VTC2019-Spring)*, pages 1–4. IEEE, 2019.

[110] W. Yu, H. Xu, and H. Feng. Robust adaptive fault-tolerant control of dynamic positioning vessel with position reference system faults using backstepping design. *International Journal of Robust and Nonlinear Control*, 28(2):403–415, 2018.

[111] S. Yuan, B. De Schutter, and S. Baldi. Robust adaptive tracking control of uncertain slowly switched linear systems. *Nonlinear Analysis: Hybrid Systems*, 27:1–12, 2018.

[112] Q. Zhang. *Basics of hydraulic systems*. CRC Press, 2008.

SUMMARY

SMART OFFSHORE HEAVY LIFT OPERATIONS

Autonomous vessels have developed into a popular research area in both industry and academia. The application of autonomy in offshore and coastal engineering could offer a safe and efficient solution to offshore transportation and operation. However, the state of the art in research has focused on waterborne transportation. Very limited research activity has been in the field of autonomous heavy lift operations. Offshore heavy lift vessels are construction vessels with large scale hydraulic cranes. One challenge to achieve autonomous offshore heavy lifting is to make smart control systems for the subsystems involved in offshore construction work, and to integrate the systems in a coordinated framework.

In this thesis, an smart control system consisting of three subsystems is proposed for safe smart offshore heavy lifting, which aims to replace or assist human operators during offshore heavy lift construction. To develop this smart system, a robust switching Dynamic Positioning (DP) controller to stabilize the position of the vessel, a nonlinear model-based mode detection system to detect the mode switching, and a backstepping crane tension controller to stabilize the load are designed.

The main contributions of this work include the modelling of the offshore heavy lift construction with a full scale heavy lift vessel, the observer-based switching controller for DP system, the detection system for different construction modes, the backstepping controller for the underactuated load, and the integration of the proposed systems.

The vessel-load system during offshore heavy lifting is a time-varying system due to the time-varying crane tension during the lifting process and the sudden change when the load is lifted from the platform. The complete construction operation can be classified into three phases: in phase 1, the vessel is not connected to any load; in phase 2, the vessel is connected to the load via the crane wires and the load is on the platform; in phase 3, the load is fully lifted from the platform by the crane and is free-hanging in the air. The three phases together comprise an offshore heavy lift construction. For the control system design, the three phases can then be summarized into two construction modes. Mode 1 denotes to phase 1 and phase 2, when the load is attached to the platform and no dynamics assumed for the load. Mode 2 refers to phase 3, when the load is free-hanging. The proposed smart system is based on the vessel-load model which follows the construction work in aforementioned phases and modes.

The proposed smart system consists of three subsystems: DP controller, mode detection system, and load controller.

The DP controller collects the position and the yaw angle of the vessel, and stabilizes the vessel in surge, sway, and yaw. It is important that a DP controller only deal with low frequency movement of the vessel due to the limitation of the propulsion system, as well as to avoid unnecessary wear and tear of the propulsion system. Thus an observer is usu-

ally required for the DP system to filter out the unwanted high frequency signals. In our design, the controller consists of a nonlinear observer and a robust switching controller. The nonlinear observer filters out the high frequency noise in the output data, and only gives the low frequency position and yaw angle of the vessel to the controller, which has three sets of controller gains. Of the three sets of gains, one is for the vessel that connects to no load (i.e., Mode 1 with no load), one is for the vessel connected to a load on the platform (i.e., Mode 1), and one is for the vessel with the load hanging (i.e., Mode 2). The uncertainties in the modelling of the vessel, and the crane tension are taken into consideration during the design of the controller and are user-defined.

The detection system collects the measurement from the sensors and provides the detected modes to the smart system. Once the mode changes, the control algorithms for the DP and for the crane tension should also switch to the ones for the correct mode. The detection system is designed to detect the change of the modes to ensure that the DP controller and the crane controller are functioning correctly. The proposed detection system consists of a residual generator, an adaptive threshold calculator, and a decision logic function. The residual generator is designed upon a model-based nonlinear observer, which is based on the dynamics of the vessel during Mode 1. The measurements of the vessels positions, rotation angles, velocities, and angular velocities are compared to the estimated ones to generate the residual. The residual is then compared to the adaptive threshold, which is calculated every time step. If the residual exceeds the threshold then the vessel is detected as switched to Mode 2.

The load controller is designed for the load during Mode 2. When the detection system detects the mode change, the tension controller starts its function to stabilize the free-hanging load's position. It is assumed that the crane on the vessel is fixed, and the load can only be controlled via the tension in the crane wires. Thus the load dynamics is underactuated. The position of the vessel is taken into consideration in this controller design to compensate the impact on the load position from the DP system. The controller is designed based on backstepping and command filtering to generate the underactuated control input, and to avoid the differentiation of virtual control signals.

The abovementioned subsystems function together and build up the high level control systems of the smart offshore heavy lifting system.

The proposed smart system is designed to stabilize the position of the vessel and the position of the load during offshore heavy lift operations. The whole system is built on a switching based algorithm and the vessel-crane system during offshore construction is classified into two construction modes. Mode 1 for the duration that the load is still on the platform, or partly on the platform, when the load can not move due to the friction. Mode 2 denotes the mode that the load is free-hanging, and can move in 3 Degrees of Freedom (DoFs). During an offshore heavy lift operation, the system is first set to mode 1 to stabilize the position of the vessel while the load is attached to the platform. After change of mode is detected, the system is then switched to mode 2 to stabilize both the vessel and the load.

The proposed smart system is able to: i) Detect the construction mode change from Mode 1 to Mode 2 within 10 seconds. ii) Keep the vessel in the desired position during the construction work. iii) Keep the load in position while it is hanging.

SAMENVATTING

EEN INTELLIGENT SYSTEEM VOOR ZWARE OFFSHORE HIJSOPERATIES

Onderzoek aan autonome vaartuigen heeft zich ontwikkeld tot een populair onderzoeksgebied in zowel de industrie als de academische wereld. De toepassing van autonomie in offshore- en kusttechniek zou een veilige en efficiënte oplossing kunnen bieden voor transport en werkzaamheden offshore. Het onderzoek is tot nu toe echter vooral gericht geweest op het transport. Er is nog weinig onderzoek gedaan op het gebied van autonome heavy lift-operaties. Schepen voor zwaar hijswerk op zee zijn uitgerust met grote hydraulische kranen. Een uitdaging bij zwaar hijswerk op zee is het maken van slimme regelsystemen voor de subsystemen die betrokken zijn bij hijswerk offshore, en het integreren van de systemen in een gecoördineerd kader.

In dit proefschrift wordt een intelligent regelsysteem voor veilige en slimme zware hijsoperaties offshore voorgesteld, bestaande uit drie deelsystemen. Het systeem heeft tot doel menselijke operators te vervangen of te ondersteunen. Om dit slimme systeem te ontwikkelen zijn een robuuste dynamic positioning (DP) controller ontwikkeld om de positie van het schip te stabiliseren, een niet-lineair modelgebaseerd systeem voor het detecteren van moduswijzigingen en een backstepping regelaar voor het stabiliseren van de last van de kraan.

De belangrijkste bijdragen van dit werk omvatten het modelleren van de offshore heavy lift operatie met een full-scale heavy lift-vaartuig, de waarnemer-gebaseerde omschakelcontroller voor het DP-systeem, het detectiesysteem voor verschillende modi, de backstepping-controller voor de ondergeactueerde belasting, en de integratie van deze systemen.

De belasting van vaartuigen bij zwaar hijswerk op zee is een tijdsafhankelijk systeem vanwege de in de tijd vari erende kraanbelasting tijdens het hijsproces en de plotselinge verandering wanneer de last van het platform wordt getild. De operatie kan in drie fasen worden ingedeeld: in fase 1 is het vaartuig niet verbonden met een last; in fase 2 wordt het vaartuig via de kraandraden met de last verbonden en staat de last op het platform; in fase 3 wordt de last door de kraan van het platform gehesen en hangt vrij in de lucht. De drie fasen samen vormen een offshore heavy lift operatie. Voor het ontwerp van het regelsysteem kunnen de drie fasen vervolgens worden samengevat in twee modi. Modus 1 verwijst naar fase 1 en fase 2, wanneer de last op het platform is bevestigd en er voor de belasting geen dynamisch gedrag wordt verondersteld. Modus 2 verwijst naar fase 3, wanneer de last vrij hangt. Het voorgestelde slimme systeem is gebaseerd op het model voor scheepsbelasting, dat de werkzaamheden in bovengenoemde fasen en modi volgt.

Het voorgestelde slimme systeem bestaat uit drie subsystemen: DP-controller, modusdetectiesysteem en last-controller.

De DP-controller verzamelt gegevens over de positie en de gierhoek van het vaartuig en stabiliseert de positie van het vaartuig in het horizontale vlak. Het is belangrijk dat een DP-controller alleen de laagfrequente bewegingen van het vaartuig aanstuurt wegens de beperkingen van het voortstuwingssysteem, en om onnodige slijtage van het voortstuwingssysteem te voorkomen. Er is dus in het algemeen bij DP-systeem een filter nodig om hoogfrequente signalen uit te filteren. In ons ontwerp bestaat de controller uit een niet-lineaire waarnemer en een robuuste omschakelcontroller. De niet-lineaire waarnemer filtert de hoogfrequente ruis uit de gegevens en stuurt alleen de laagfrequente positie en gierhoek van het vaartuig naar de controller. De controller heeft drie sets parameters: een voor het schip dat niet is verbonden met een lading (d.w.z. Modus 1 zonder last), een voor het schip dat is verbonden met een lading op het platform (d.w.z. Modus 1), en een voor het schip met de hangende last (d.w.z. Modus 2). Bij het ontwerp van de besturing wordt rekening gehouden met onzekerheden in de modellering van het schip en de belasting van de kraan; deze worden door de gebruiker ingesteld.

Het detectiesysteem verzamelt de metingen van de sensoren en stuurt de gedetecteerde modus naar het slimme systeem. Zodra de modus verandert moeten ook de besturingsalgoritmen voor de DP en voor de belasting van kraan overschakelen naar die voor de juiste modus. Het detectiesysteem is ontworpen om de wijziging van de modi te detecteren, om ervoor te zorgen dat de DP-controller en de kraancontroller correct werken. Het voorgestelde detectiesysteem bestaat uit een verschilgenerator, een drempelcalculator en een beslissingsregel. De verschilgenerator is ontworpen op een model van niet-lineaire waarnemer, die is gebaseerd op de dynamica van het vaartuig tijdens modus 1. De metingen van de posities van het vaartuig, rotatiehoeken, snelheden en hoeksnelheden worden vergeleken met de schattingen. Het verschil wordt vervolgens vergeleken met de drempel, die elke tijdstap opnieuw wordt berekend. Als het verschil de drempel overschrijdt, wordt het vaartuig gedetecteerd als te zijn overgeschakeld naar modus 2.

De lastcontroller is ontworpen voor de belasting tijdens modus 2. Wanneer het detectiesysteem de modusverandering detecteert begint de spanningsregelaar met zijn werk om de positie van de vrijhangende last te stabiliseren. Aangenomen wordt dat de kraan vast zit aan het schip en dat de last alleen kan worden gestuurd via de spanning in de hijsdraden. De belastingsdynamiek wordt zo ondergeactueerd. Bij dit ontwerp van de controller wordt rekening gehouden met de positie van het schip om de impact op de positie van de last uit het DP-systeem te compenseren. De controller is ontworpen op basis van backstepping en opdrachtfiltering om de ondergeactueerde regelinvoer te genereren en om differentiatie van virtuele stuursignalen te vermijden.

De bovengenoemde samenwerkende subsystemen vormen samen het hoogwaardige regelsystemen voor een intelligente systeem voor zwaar offshore hijswerk.

Het voorgestelde systeem is ontworpen om de positie van het vaartuig en de positie van de last te stabiliseren tijdens zware hijsoperaties op zee. Het hele systeem is ontworpen op een op omschakeling gebaseerd algoritme. Het schip-kraansysteem tijdens de hijsoperatie wordt beschouwd in twee modi. Modus 1 als de last zich nog op het platform bevindt, wanneer de lading niet kan bewegen door de wrijving. Modus 2 geeft de toestand weer waarin de last vrij hangt en kan bewegen met drie vrijdheidsgraden. Tijdens een hijsoperatie wordt het systeem eerst ingesteld op modus 1 om de positie van

het schip te stabiliseren terwijl de last op het platform ligt. Nadat een verandering van modus is gedetecteerd, schakelt het systeem over naar modus 2 om zowel het schip als de lading te stabiliseren.

Het voorgestelde intelligente systeem kan: i) Binnen 10 seconden en wijziging van modus 1 naar modus 2 detecteren; ii) Het schip tijdens de werkzaamheden in de gewenste positie houden; iii) De hangende last op zijn plaats houden.

CURRICULUM VITÆ

Jun YE

21-04-1991 Born in Henan, China.

EDUCATION

2009–2013	Undergraduate in Marine Engineering Shanghai Jiao Tong University. Shanghai, China
2014–2016	Master of Science in Maritime Technology Delft University of Technology. Delft, the Netherlands
2016–2020	PhD. in Maritime Technology Delft University of Technology. Delft, the Netherlands
Thesis:	Smart OFfshore Heavy Lift Operations
Promotor:	Prof. dr. R.R. Negenborn

PUBLICATIONS

Ye, J., Godjevac, M. and el Amam, E., 2017, October. Position control of crane vessel during offshore installations: Using adaptive and robust control methods. In 2017 21st International Conference on System Theory, Control and Computing (ICSTCC) (pp. 17-22). IEEE.

Ye, J., Roy, S., Godjevac, M. and Baldi, S., 2019. Observer-based robust control for dynamic positioning of large-scale heavy lift vessels. IFAC-PapersOnLine, 52(3), pp.138-143.

Ye, J., Reppa, V., Negenborn, R.R., 2020. Command filtered Backstepping Control of an Underactuated Offshore Heavy Crane. In 2020 IFAC World Congress.

Ye, J., Godjevac, M., Baldi, S. and Hopman, H., 2019. Joint estimation of vessel position and mooring stiffness during offshore crane operations. Automation in Construction, 101, pp.218-226.

Ye, J., Roy, S., Godjevac, M., Baldi, S., 2020. A Switching Control Perspective on the Offshore Construction Scenario of Heavy-Lift Vessels. IEEE Transactions on Control Systems Technology.

On Robustifying Vessel Positioning to Unmodelled/Uncertain Mooring and Thruster Dynamics. Submitted to a journal.

Construction Mode Detection for Autonomous Offshore Heavy Lift Operations. Submitted to a journal.